NUREG/CR-1249
BNL-NUREG-51130
R-1,7,8

ADVANCED REACTOR SAFETY RESEARCH DIVISION

QUARTERLY PROGRESS REPORT
JULY 1 - SEPTEMBER 30, 1979

HERBERT J.C. KOUTS, Department Chairman
WALTER Y. KATO, Associate Chairman for Reactor Safety

Principal Investigators:

Ashok K. Agrawal	Owen C. Jones, Jr.
Ralph J. Cerbone	Cesar Sastre

Compiled by: Anthony J. Romano
Manuscript Completed: January 1980

DEPARTMENT OF NUCLEAR ENERGY
BROOKHAVEN NATIONAL LABORATORY, ASSOCIATED UNIVERSITIES, INC.
UPTON, NEW YORK 11973

Prepared for the
REACTOR SAFETY RESEARCH DIVISION
OFFICE OF NUCLEAR REGULATORY RESEARCH
U.S. NUCLEAR REGULATORY COMMISSION
CONTRACT NO. DE-AC02-76CH00016
FIN Nos.:

A-3015	A- 24
A-3016	A-3041

FOREWORD

The Advanced Reactor Safety Research Programs Quarterly Progress Report describes current activities and technical progress in the programs at Brookhaven National Laboratory sponsored by the USNRC Division of Reactor Safety Research. The projects reported each quarter are the following: HTGR Safety Evaluation, SSC Code Development, LMFBR Safety Experiments and Fast Reactor Safety Code Validation.

The previous reports, BNL-NUREG-50624, BNL-NUREG-50661, BNL-NUREG-50683, BNL-NUREG-50747, BNL-NUREG-50785, BNL-NUREG-50820, BNL-NUREG-50883, BNL-NUREG-50931, BNL-NUREG-50978, BNL-NUREG-51014 and BNL-NUREG-51082 have covered the periods October 1, 1976 through June 30, 1979.

ADVANCED REACTOR SAFETY RESEARCH

TABLE OF CONTENTS

I. HTGR SAFETY EVALUATION

SUMMARY

Compressive strength, Young's modulus and strain to failure of as-received and oxidized PGX graphite specimens have been measured. The values for as-received graphite are in good agreement with those obtained by workers at General Atomic Company. The compressive strength of graphite oxidized in $H_2O/H_2/He$ at 800°C and assumed to have a sharp reaction profile is consistent with that expected for near surface burnoff. No continuous effect of burnoff on the modulus and strain to failure of oxidized specimens was observed; however, a significant drop in both of these parameters, and perhaps also in compressive strength, was observed during the initial stages of oxidation.

The volumetric rate coefficient, K_v, of PGX EL-2 specimens is calculated to be 10^2 to 2×10^3 greater than that of H451 graphite. This is consistent with the range of values observed by General Atomic Company, but is quite different from the range calculated for PGX ML-2 specimens; the latter gave $K_v^{PGX}/K_v^{H451} = 4$ to 7×10^4.

Prestressing H451 graphite to 75% of its compressive strength appeared to induce a 50% increase in the rate of oxidation with water vapor at 750°C, a 15% increase with air at 500°C and a 10% increase with air at 550°C. These effects will be reexamined during the next quarter.

Nondestructive determination of iron concentration in large specimens of PGX graphite via an oxidation/reduction/oxidation techniques appears to be feasible. Further work is needed, however, to demonstrate and refine the technique.

Detailed scanning electron microscope studies were conducted on Incoloy 800H high cycle fatigue specimens tested in air and HTGR helium. For the in-helium tests preaged specimens were also studied. It was found that for the material preaged in helium for 1500 hours at 760°C, there was severe intergranular corrosion which leads to early fatigue failure. Electron microprobe analyses were carried out to characterize the oxidation characteristics during fatigue.

Hastelloy X and annealed 2 1/4Cr-1Mo steel were also valuated for high cycle fatigue resistance. In the case of the 2 1/4Cr-1Mo steel the helium test gas was found to cause extensive decarburization which gave a large decrease in fatigue strength.

Creep rupture testing of Incoloy 800H and Hastelloy X in air and in a simulated HTGR helium is continuing. Long term tests on Incoloy 800H are being carried out at 649°C and at 760°C and tests on Hastelloy X at 760°C and 871°C. Results of tests extending over 13,000 hours show no significant effect of the helium environment on creep rate of either material but slightly lower rupture strengths are being observed for both alloys.

In the fission product/metal interaction program a series of thermally aged specimens was evaluated using the scanning electron microscope/microprobe. Several distinct surface features were observed including Fe, Fe_xO_y and

Cr_2O_3. The formation of these species during oxidation is outlined.

As a continuation of work already started in the Helium Impurities Loop (HIL), static experiments have begun which will determine the activities of the various components (C, Cr, Mo, FeO, etc.) of HTGR materials.

A number of runs were made to measure the release of CO gas from samples of UO_2, ThO_2 and simulated fission products at temperatures to 2000°C. Preliminary data indicate that pressure increases on heating are not readily reversed on cooling.

1. Graphite

The thrust of the current graphite experimental program is the study of strength loss mechanisms in PGX graphite. Two broad task areas have been designated for this effort. The first comprises oxidation mechanisms, including the effects of non-oxidizing environments, activated (surface) diffusion of oxidants, and direct thermal oxidation on strength. The second task area comprises stress mechanisms, including the effects of stress before and during oxidation on strength.

A separate but related investigation is the study of rate expressions for the oxidation of graphite. This has been put aside temporarily to examine the feasibility of monitoring the iron content of large specimens of PGX graphite via oxidation/reduction/oxidation technique.

1.1 Oxidation Induced Strength Loss in PGX Graphite (F. B. Growcock, J. H. Heiser, III, G. Uneberg)

Problems with the operation of the mass spectrometer precluded any experiments on the exposure of PGX graphite to a non-oxidizing environment. As of this writing, the problems appear to have been solved and the instrument is operating satisfactorily; experiments performed at 900°C with 3/4 inch by 1 1/2 inch, 1 1/2 inch by 1 1/2 inch and 3 inch by 3 inch specimens will be started very soon, using argon rather than helium; at this temperature helium diffuses through quartz quite rapidly compared to the duration of the experiments, while argon is much slower and is not expected to affect the results significantly.

The High Temperature Mass Transport Apparatus is being welded and should be tested for specimen sealing soon. Permeability experiments at low pressure differentials and roon temperature will be done first. Experiments at elevated temperatures will be done when the designated tube furnace becomes available. The apparatus will be goldplated internally if high pressure differentials or reactive gases give problems. Effective diffusion coefficients will be measured when the Carle gas chromatograph is available; it is now in service full time, supplying data for three different task areas.

The investigation of strength loss in PGX graphite arising from thermal oxidation was continued. A schematic of the loop used to supply He + H_2O + H_2 to the specimens is shown in Figure 1.1. It has been dubbed the "Graphite Oxidation Loop." Reactor No. 1 is the "Uniform Flow Apparatus" for oxidation of 1 1/2 inch by 3 inch cylindrical specimens (3 specimens per run); Reactor No. 2 is a larger version of the "Uniform Flow Apparatus," designed to accommodate up to six 3 inch by 3 inch cylindrical specimens. The converter is a bed of CuO granules which oxidizes approximately 1 percent of the H_2 per pass. CO is removed in a batch process by venting or carbonyl formation. The system incorporates safety features in the event of power failure or depressurization. Additionally, alternate traps and gas supplies are included to maintain continuous operation at all times.

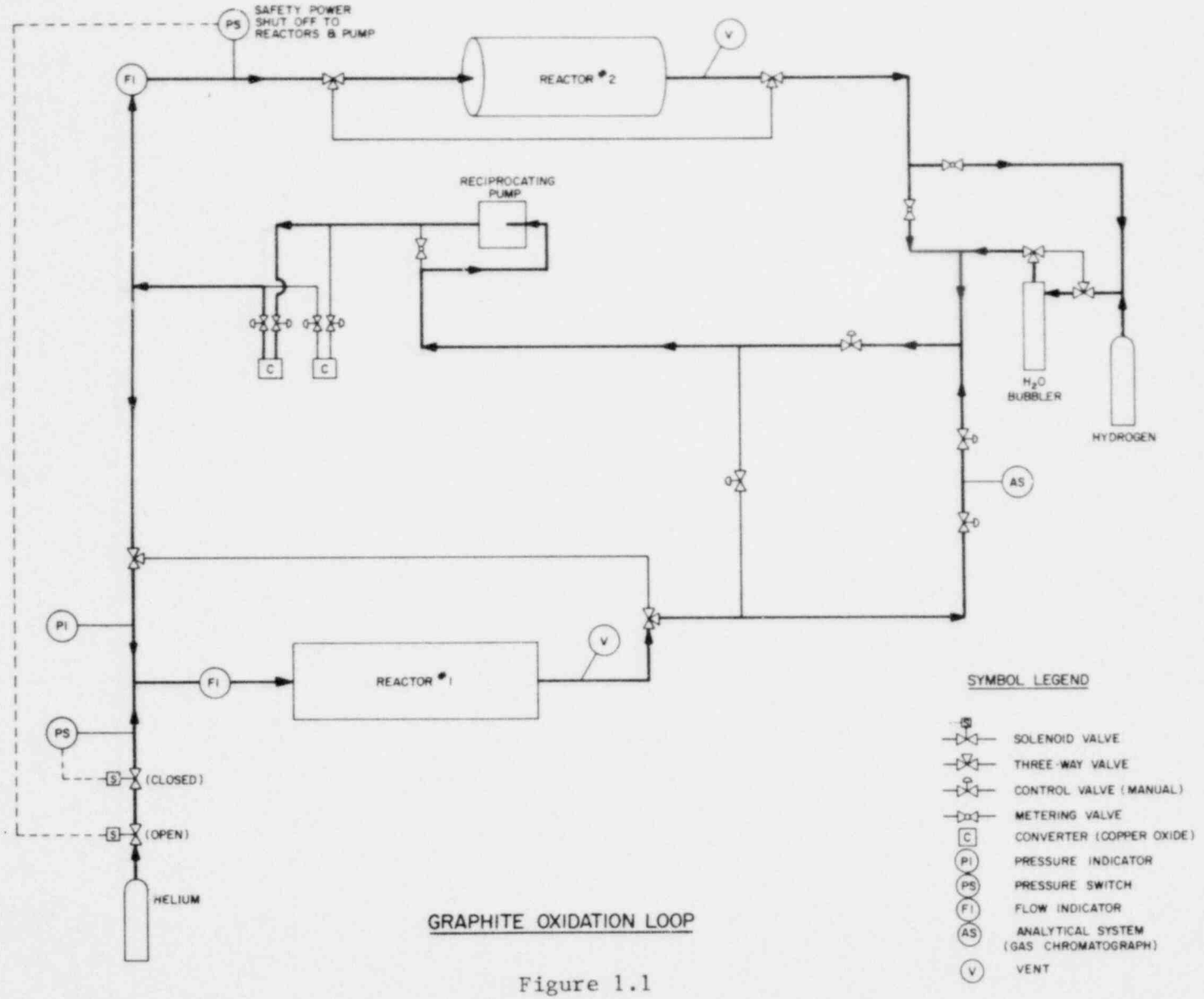

GRAPHITE OXIDATION LOOP

Figure 1.1

Strength of As-received PGX Graphite

Previous series of oxidation runs in the Uniform Flow Apparatus with 1 1/2 inch by 1 1/2 inch cylindrical graphite specimens gave rise to a large scatter in the compressive strength (σ_c) versus burnoff data. Insufficient numbers of control specimens were strength tested at that time to clearly reveal a problem. Since then, other experiments have been performed, leading to a similar large scatter in the data. We have attempted to isolate the problem by testing unoxidized PGX graphite specimens machined in various shops and strength tested with two instruments. Seventy seven axial blocks from the second half of the endlength of BNL log 2 (Union Carbide log 29N6-2), designated EL-2b, were cut, labeled, randomized and distributed to three machine shops. Specimens 1 1/2 inches by 3 inches were machined to minimum tolerances in diameter, length, perpendicularity and parallelism. The finished specimens were then strength tested according to ASTM C695-75 with a machine in the Metallurgy and Materials Science Division at BNL by Don Horne or the old mechanical machine in the HTGR Division. The results, along with those of other unoxidized specimens, are shown in Table 1.1. These results show unequivocably that the specimens tested with the machine in the HTGR Division give an inordinate amount of scatter in the data. Furthermore, the scatter is not due to random error, as evidenced by the low average compressive strengths obtained with that machine. No effect of tolerance level was observed. In fact, specimens which did not meet specifications exhibited the same strength (within the uncertainty interval $\pm$ 2 S_{σ_c}) as the others. Future testing will be done with the machine in the Metallurgy and Materials Science Division.

Several observations made during the course of working with PGX graphite should be mentioned. The EL-2 specimens, like the ML-2, ring out with a metallic sound when struck, whereas the EL-1 specimens give a ceramic-like sound. Another major difference is their machinability: during cutting operations, EL-2 and ML-2 specimens did not crumble and flake the way EL-1 specimens did. Under stress the specimens fractured many different ways, sometimes almost parallel to their axes, sometimes at an angle approaching 45° (see Gillin, 1967) and sometimes they simply crumbled; usually, however, they fractured at an angle between 27° and 35°, in keeping with the value (35°)observed in other graphites (Taylor, 1967). Some workers have detected acoustic "pre-emission" during loading of graphites (Andrew, 1960); although this phenomenon has not been observed by us with PGX graphite, some specimens under load would partially fail, then continue to support ever increasing loads.

A typical stress-strain curve obtained in the EL-2 runs is shown in Figure 1.2. It was of interest to us to approximate Young's Modulus for these specimens. We do not know a priori the relationship between stress, F/A, and strain, ε. However, we can construct models to approximate the stress-strain data particularly in the vicinity of zero stress. Some of the analytical functions used are plotted alongside the data in Figure 1.2. Young's Modulus, E, can be approximated from $\lim_{\varepsilon \to 0} \left(\frac{F/A}{\varepsilon}\right)$, which is the same as the limiting slope.

For the six equations listed in Figure 1.2, the following results were obtained (where 1 GPa = 1.45×10^5 psi):

Table 1.1

Mechanical Properties of As-received PGX Graphite

Specimens[a]	Number Sampled	Machine Shop[b]	Testing Machine[c]	Compressive Strength, MPa $\bar{\sigma}_c$	S_{σ_c}	Young's Modulus, GPa $\bar{E}$	S_E	Strain to Failure, cm/cm $\bar{\varepsilon}_f$	S_{ε_f}
EL-1	3	A	1	29.7	1.9	---	---	------	------
EL-1	9	C	1	22.2	8.4	---	---	------	------
ML-2	7	A	1	34.4	3.7	---	---	------	------
EL-2a	20	B	1	37.6	4.3	---	---	------	------
EL-2a	21	B	2	42.4	1.3	4.4	1.0	0.0252	0.0009
EL-2b	19	B	1	34.9	7.6	---	---	------	------
EL-2b	19	B	2	42.1	0.8	5.0	0.9	0.0248	0.0012
EL-2b	20	C	2	42.6	0.8	4.5	0.6	0.0258	0.0015
EL-2b	19	D	2	41.9	1.2	5.4	3.2	0.0256	0.0019

[a]Axial specimens 1.500" x 3.000": EL = endlength; ML = midlength

[b]A: Crude lathe in HTGR Safety Division - tolerances of ± 0.015" for diameter and length.
B: Precision Swiss lathe in HTGR Safety Division - tolerances of ± 0.0005" for diameter and length.
C: BNL Central Shops - tolerances of ± 0.001" for diameter and length.
D: Mercury Tool Company - tolerances of ± 0.001" for diameter and length.

[c]#1: Tinius-Olsen 12,000 lb mechanical machine, cross-head speed ca. 0.03"/min, flexible contact blocks.
#2: Satec 300 ton hydraulic machine, stress rate 8,000 lb/min, fixed contact blocks.

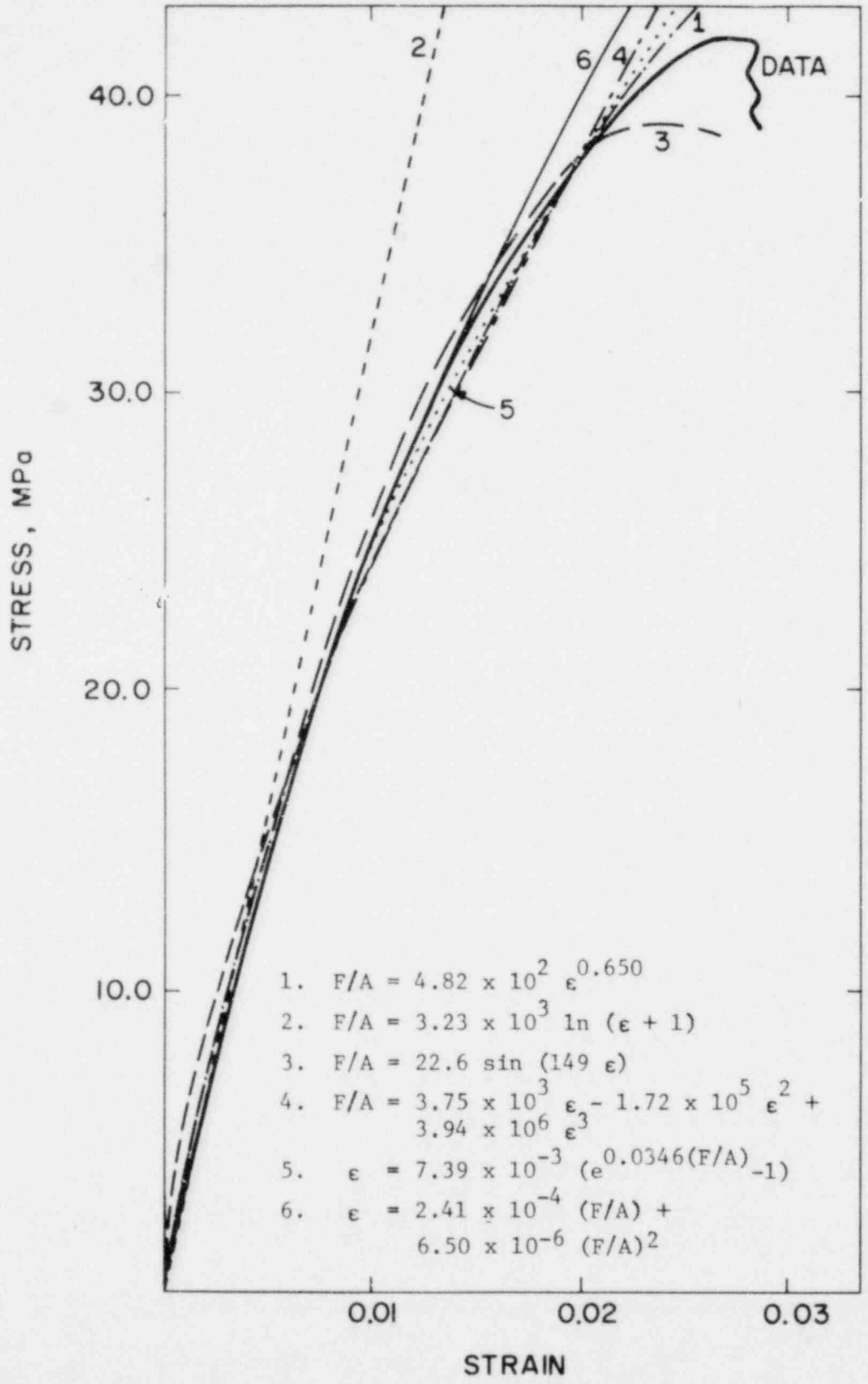

Figure 1.2. Typical stress versus strain plot obtained during σ_c determination of PGX graphite.

(1) $E = \infty$
(2) $E = 3.23$ GPa
(3) $E = 3.38$ GPa
(4) $E = 3.75$ GPa
(5) $E = 3.90$ GPa
(6) $E = 4.15$ GPa

None of the six functions is entirely satisfactory, but they are simple to use. Equations (5) and (6) are ar to model the stress-strain behavior best near the origin; Equation (6) is based on a physical model proposed by Jenkins (1962, 1969). Consequently, EL-2 data were fitted to equations of this form. Average values of Young's Modulus and the sample standard deviation, S_E, are given in Table 1.1. Also tabulated therein are the average values of ε_f, strain to failure. These values may be comapred with those obtained by General Atomic Company using ASTM procedures (Engle, 1978). Batches of six specimens each from log 6484-138 yielded the following ranges of values: $\bar{\sigma}_c = 37.0$-39.2 MPa (1 MPa = 145 psi) with $S_{\sigma_c} = 0.8$-2.5 MPa, $\bar{E} = 2.8$-3.2 GPa with $S_E = 0.1$-0.2 and $\bar{\varepsilon}_f = 0.0233$-$0.0254$ with $S_{\varepsilon_f} = 0.0011$-$0.0033$. Similarly, log 6484-112 yielded $\sigma_c = 40.3$-45.7 MPa with $S_{\sigma_c} = 0.8$-2.8 MPa and $\bar{E} = 4.5$-5.6 GPa with $S_E = 0.1$-0.4 GPa.

We have fitted the GA data from both logs to the linear expression

$$\sigma_c = 2.73 \times 10^{-3} E + 29.4$$

where both σ_c and E are in units of MPa. Maximum uncertainties in the slope and $\sigma_c(o)$ are $\pm$ 3.2×10^{-4} and $\pm$ 1.37, respectively, with 90% confidence. Assuming that this expression can be generalized to include our PGX graphite specimens, we calculate $\sigma_c = 41.4$-44.1 MPa for $E = 4.4$-5.4 GPa. This range of σ_c values agrees well with that obtained experimentally for EL-2 specimens ($\sigma_c = 41.9$-42.6 MPa). This good agreement between the BNL and GA results extends also to the values obtained for ε_f.

It should be emphasized that our method for estimating E is crude. This is borne out by the S_E values, which are considerably higher than the GA values; indeed, the uncertainties represented by S_E in Table 1.1 are necessarily lower limits, since E is model dependent. The data were fitted to Jenkins-type equations at $\varepsilon = 0.00667$ and $\varepsilon = 0.01333$; we do not know how accurate these expressions are near zero stress, since the data are not sufficiently precise in this region.

Strength of Oxidized PGX Graphite

Axial endlength specimens from Union Carbide log 29N6-2 (EL-2a) were oxidized in the Uniform Flow Apparatus at 800°C with 0.17% H_2O + 1.7% H_2 in He flowing at 25 SLM. The effect of burnoff on σ_c and E is shown graphically in Figure 1.3. Oxidation data and mechanical properties of the EL-2a specimens are listed in Table 1.2.

Visual inspection of these specimens revealed the presence of a thin uniform low density ring at the exposed surface. Deep holes or craters were absent. The

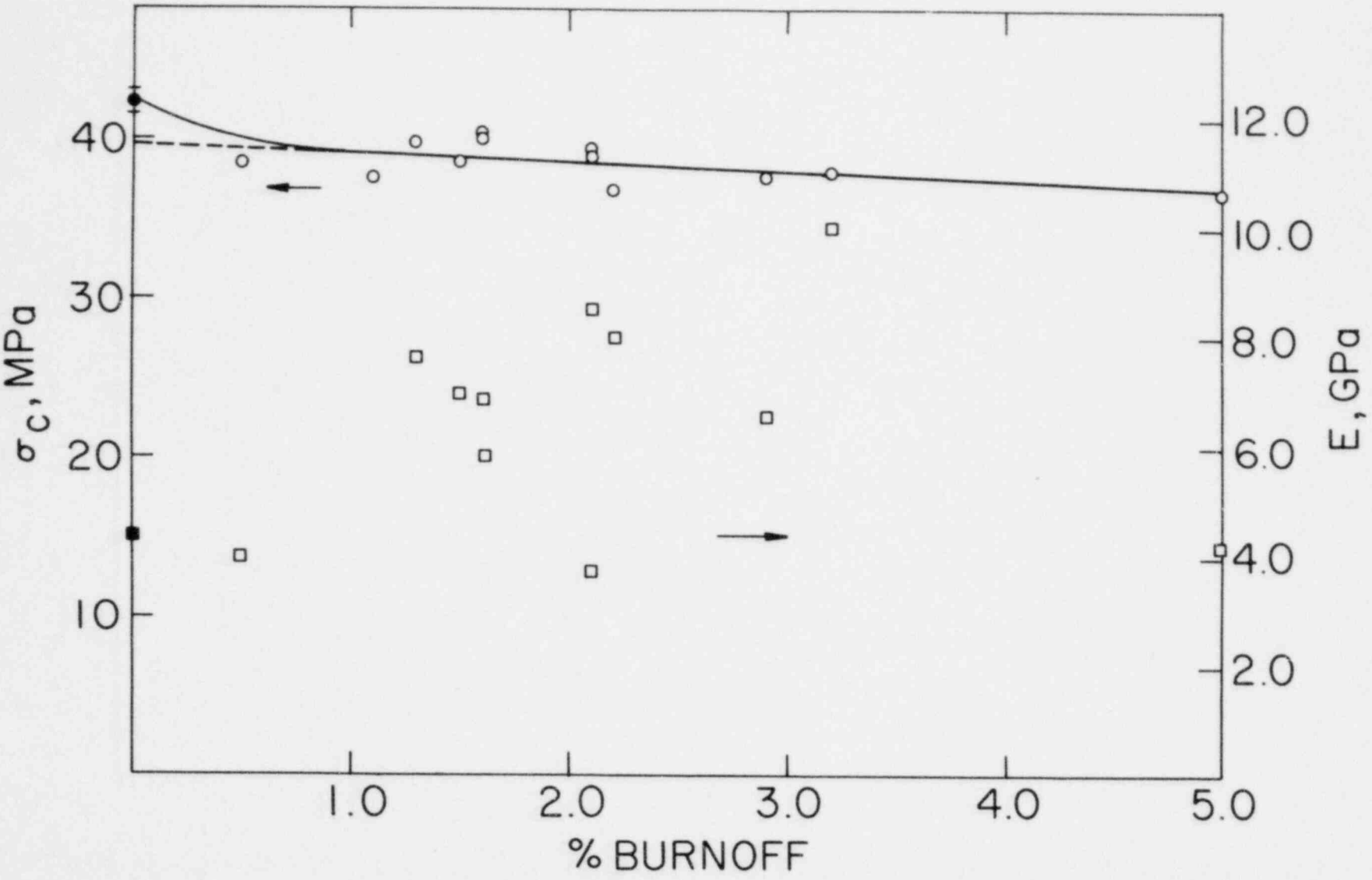

Figure 1.3. The effect of burnoff on ultimate compressive strength and Young's modulus of PGX graphite EL-2a specimens.

Table 1.2

Oxidation Data and Mechanical Properties of Axial EL-2a Specimens

Specimen	Burnoff,%	Reaction Time[a] hr	$\bar{L}$,mm	$\bar{K}_v$,sec^{-1}	σ_c,MPa	E,GPa	ε_f
66	0.5	48.3	3.10	0.67	38.6	4.0	0.0223
64	1.1	48.0	1.41	3.30	37.8	19.8	0.0223
28	1.3	88.5	2.19	1.35	39.9	7.6	0.0220
10	1.5	NA	NA	NA	38.7	7.0	0.0227
29	1.6	48.3	0.97	6.88	40.2	6.9	0.0248
31	1.6	48.0	0.97	6.97	40.5	5.9	0.0248
4	2.1	48.0	0.74	12.0	39.4	3.7	0.0260
71	2.1	88.5	1.36	3.53	39.1	8.6	0.0240
52	2.2	48.3	0.71	13.0	37.0	8.0	0.0225
16	2.9	88.5	0.98	6.7	37.9	6.5	0.0225
9	3.2	NA	NA	NA	38.0	10.0	0.0237
15	5.0	NA	NA	NA	36.8	4.2	0.0233

[a]NA = not available.

effect of burnoff on compressive strength is also consistent with near surface burnoff. These observations are in agreement with those made of ML-2 specimens oxidized in the same manner (Growcock, 1979). However, the loss of strength in the burnoff region below 0.5% appears to be a little greater than expected. The data above zero burnoff can be fitted by linear regression analysis to the line $\sigma_c = -54.4b + 39.7$, where b is the fractional mass loss and the uncertainties in the slope and intercept are $\pm$ 46.2 and $\pm$ 11.6, respectively, at the 90% confidence level; the "true" intercept at 42.4 MPa lies well within the uncertainty figure. However, if we force the intercept at 42.4 MPa we obtain $\sigma_c = -152b + 42.4$, where the uncertainty in the slope is $\pm$ 414 at the 90% confidence level. This suggests that the apparent larger than normal strength loss below 0.5% burnoff may be significant, but further investigation is necessary to settle the issue.

The effect of burnoff on Young's Modulus is difficult to ascertain from the values plotted in Figure 1.3. The precision can be improved considerably by calculating E using values closer to the origin in the stress-strain curves; however, the E values themselves will be reduced substantially and thus their accuracy is questionable. The plotted values yield $\bar{E}$ = 6.58 GPa and S_E = 2.01 GPa. A comparison of these parameters with those for the as-received graphite indicates that the null hypothesis is invalid in both the F-test at the 95% confidence level and the t-test at the 99.5% level. It appears that there is statistically significant divergence between the average values of E. The same is true for the average strain to failure ($\bar{\varepsilon}_f$ = 0.0234 and S_{ε_f} = 0.0013) of the oxidized specimens relative to that of the virgin material. Board and Squires (1966) found that bulk oxidation of British pile grade "A" graphite by CO_2 did not affect the strain to failure. However, Beavan (1979) found a reduction in ε_f during tensile testing of oxidized PGX graphite; specimens oxidized by H_2O in He to give a sharp burnoff profile at a total burnoff of 8.2-10.8% showed ε_f

to be 15% lower than that of unoxidized specimens. Our EL-2 specimens display no continuous decrease in ε_f, but there does appear to be a sudden change in ε_f, as well as in E and σ_c, at the onset of oxidation. We will continue to investigate these phenomena.

The rate of oxidation of PGX graphite increases with time. Typical [CO]/[H_2O] versus time curves are shown in Figure 1.4. The rates of EL-2 and ML-2 specimens increase rapidly to a constant value, whereas the rates of EL-1 specimens increase continuously throughout a run. The behavior of the former is consistent with the establishment of a constant oxidation profile, whereas that of the latter is more in keeping with "bulk" oxidation.

The average values of the volumetric rate coefficients, K_v, and the diffusion lengths, L, calculated from the oxidation data of EL-2 specimens are shown in Table 1.2. The small values of $\bar{L}$ are consistent with the physical appearance of the specimens. It is interesting to compare values of $\bar{K}_v$ with those obtained for H451 graphite. From a composite rate expression determined by Velasquez, et al (1978), $K_v^{H451} = 6.77 \times 10^{-3}$ sec^{-1} at 1% burnoff under our conditions (this is not much different from the value 7.54×10^{-3} sec^{-1} obtained with the Fuel Design Data Manual Rate Constants). The $\bar{K}_v^{PGX}$ (EL-2) values are greater than K_v^{H451} by factors of 99 to 1920; burnoff effects are ignored. This is in contrast to the values obtained previously for ML-2 specimens (Growcock, 1979), which gave $\bar{K}_v^{PGX}$ (ML-2)/K_v^{H451} = 3.6 to 7.0 x 10^4. It is apparent that the reactivity of PGX graphite is quite variable; thorough documentation of this variability is of considerable importance.

A series of EL-1 specimens has been oxidized; unfortunately, strength testing was done with the Tinius-Olsen machine, so that the scatter makes interpretation of the data difficult. Another series of EL-1 specimens is being prepared for oxidation; results from these runs will be presented in the next progress report. In addition, specimens from a third log of PGX graphite will be characterized and oxidized, and density profiles of some of these specimens will be obtained along with the strength data.

1.2 Stress Induced Strength Loss in Nuclear Graphites (M. Eto, F. B. Growcock)

During this quarter experiments were carried out to determine the dependence on temperature, burnoff and prestress of the reaction rates of PGX and H451 graphites in air and water vapor/hydrogen/helium mixtures. Specimens were oxidized under chemical reaction control conditions. Preliminary tests have been performed on the oxidation of graphite under tensile or compressive stressing using the stress apparatus which was described in the previous report.

Effect of Temperature

Arrhenius plots for the reaction rate of H451 graphite oxidized in air at temperatures between 450 and 600°C are shown in Figure 1.5; these plots were obtained in a manner similar to that described for PGX graphite in the previous progress report (Eto, 1979). Maximum burnoffs were 7.9 and 10.2% for the specimens represented by solid circles and open circles, respectively. These plots yield an apparent activation energy of 197 kJ/mol for air oxidation of H451,

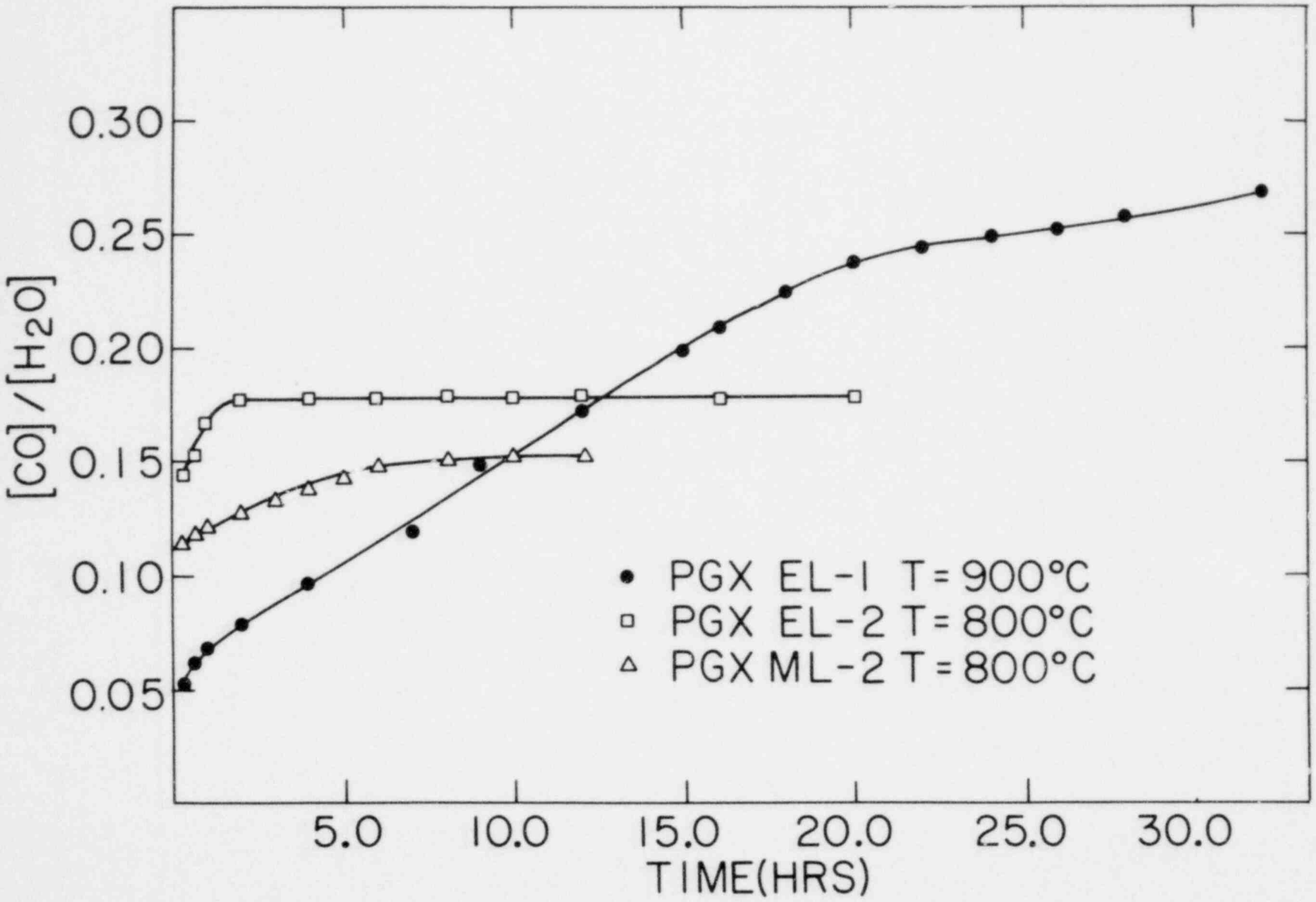

Figure 1.4. Rate of CO formation as a function of reaction time during oxidation of PGX graphite by 0.17% H_2O + 1.7% H_2 in He.

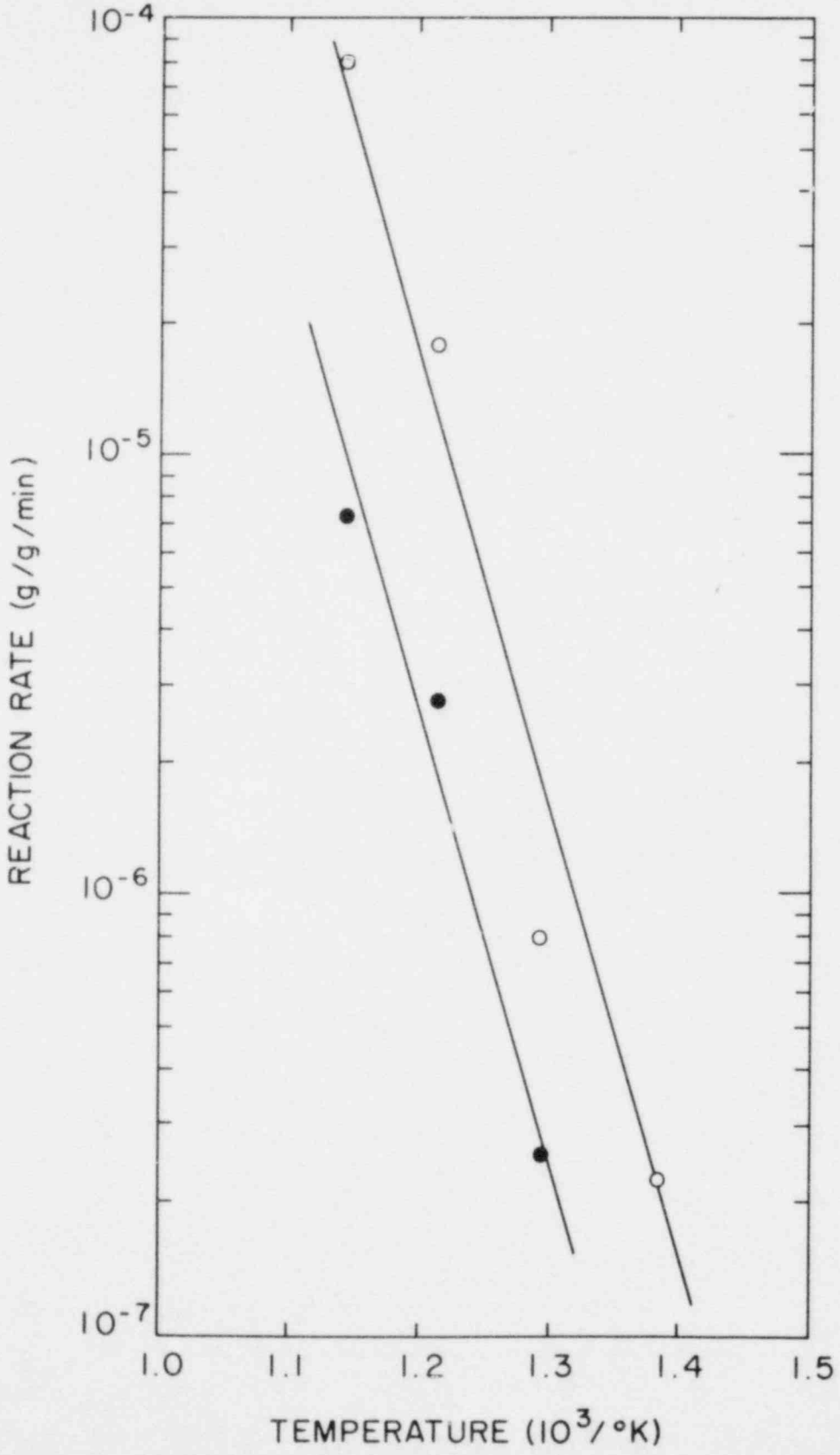

Figure 1.5. Arrhenius plot for H451 graphite oxidized in air. Maximum burnoff is 10.2% for open circles and 7.93% for solid circles.

which is about 10 kJ larger than that obtained for PGX. Since oxidation in air at 650°C occurred in the diffusion limited temperature regime, the data obtained at this temperature were omitted from the figure.

For PGX graphite oxidized in a water vapor (2%)/hydrogen (20%)/helium (80%) mixture at a flow rate of 600 sccm the activation energy was estimated to be 189 kJ/mol in the temperature range 550 to 750°C, which is almost equal to that for air oxidation of the graphite. Arrhenius plots are shown in Figure 1.6, where maximum burnoffs are 6.25% (open circles) and 9.05% (triangles). These specimens will be exposed to this atmosphere at higher temperatures in the next quarter. The value obtained here is, as in the case of air oxidation, at least 20% lower than that reported in the literature (Walker, et al, 1959) for more ideal materials, i.e. 230-350 kJ/mol. Since the reaction rate is affected by catalytic elements such as iron, the quantity of hydrogen in the oxidizing atmosphere and burnoff (Everett, et al, 1967), the difference observed here is not surprising.

Considering the relatively high iron concentration in this graphite, catalysis may be a major factor which makes the activation energy low.

Effect of Burnoff

Figure 1.7 shows the dependence of reaction rate on burnoff in the case of PGX graphite oxidized in air at temperatures between 450 and 500°C. Reaction rate increases with increasing burnoff. However, no pronounced increase is observed if burnoff is less than 10%. A similar trend was observed for H451 graphite, though the data are somewhat sparse. The rate at 20% burnoff seems to be 2 to 3 times larger than that at 10% burnoff. Burnoff dependence of the reaction rates of PGX and H451 graphites with water vapor above 700°C will be examined in the near future.

Effect of Prestress

Experiments similar to those described in the previous report were done for air and water vapor oxidation of H451 graphite. An H451 graphite specimen was first oxidized at 500°C or 550°C in air at 300 sccm or at 750°C in a water vapor (2%)/helium mixture at 200 sccm, until a stabilized rate was attained. The specimen was then stressed to 75% of its compressive strength, which was estimated from previously obtained data. In contrast to PGX graphite, the data for H451 seems to show that the rate for air oxidation is slightly enhanced by prestressing, i.e. about 15% at 500°C and 10% at 550°C. Figure 1.8 shows the result obtained in the case of water vapor oxidation. Here open circles represent the unstressed specimen, whereas solid symbols are for the data after stressing. These data indicate that prestress caused ca. 50% increase in the reaction rate at 750°C. To confirm that this enhancement is not an artifact, a control specimen which was prestressed to 75% of mean compressive strength before the first run was oxidized in a similar manner. This time no enhancement of rate was observed upon reexposing the specimen to the oxidizing conditions. This can be seen in Figure 1.9. In these experiments maximum burnoff was less than 1%.

In the next quarter, effects of lower and higher prestress as well as stress under oxidation will be investigated to elucidate the relationship between reac-

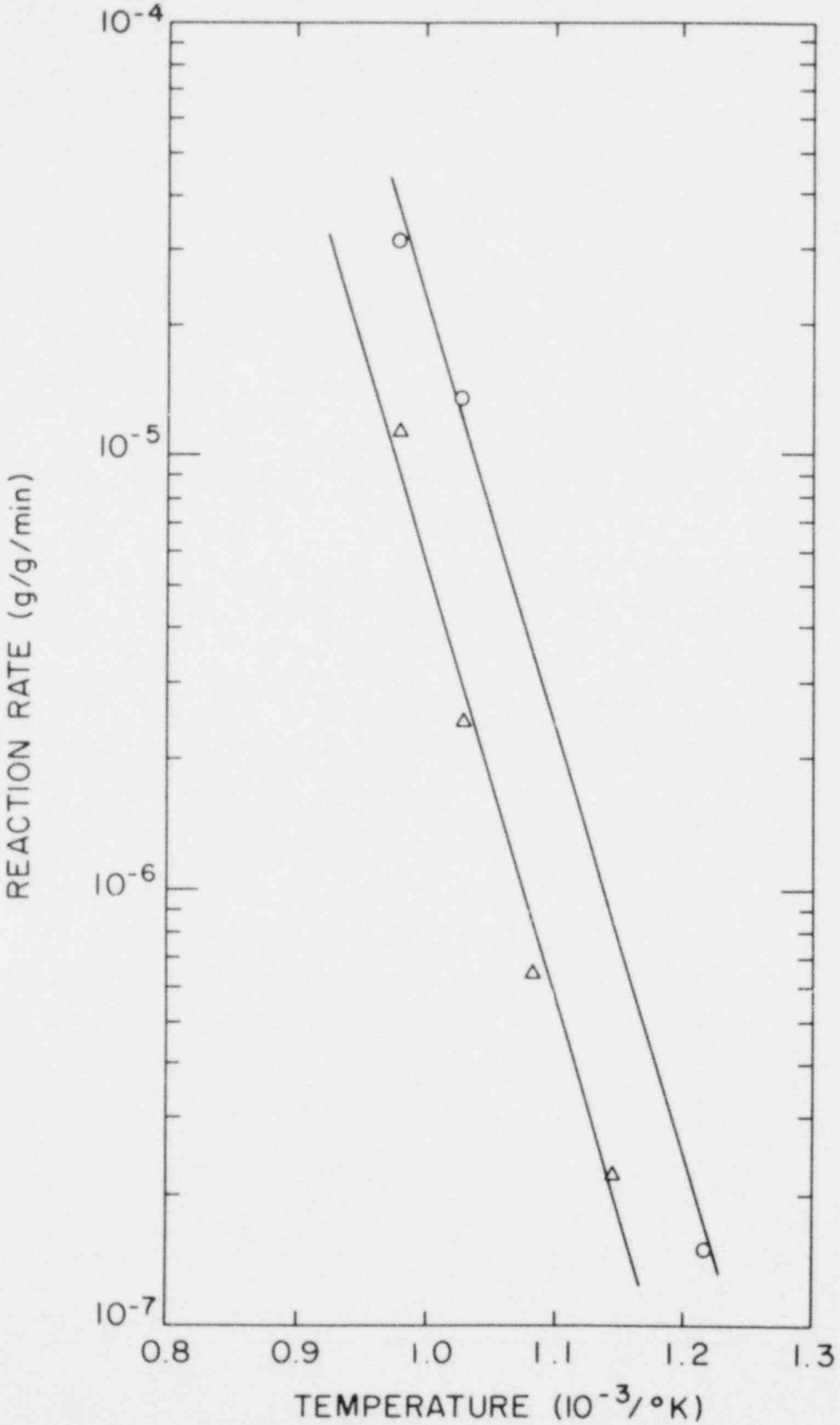

Figure 1.6. Arrhenius plot for PGX graphite oxidized in a 2% water vapor/ 20% hydrogen/80% helium mixture. Maximum burnoff is 6.25% for open circles and 9.05% for triangles.

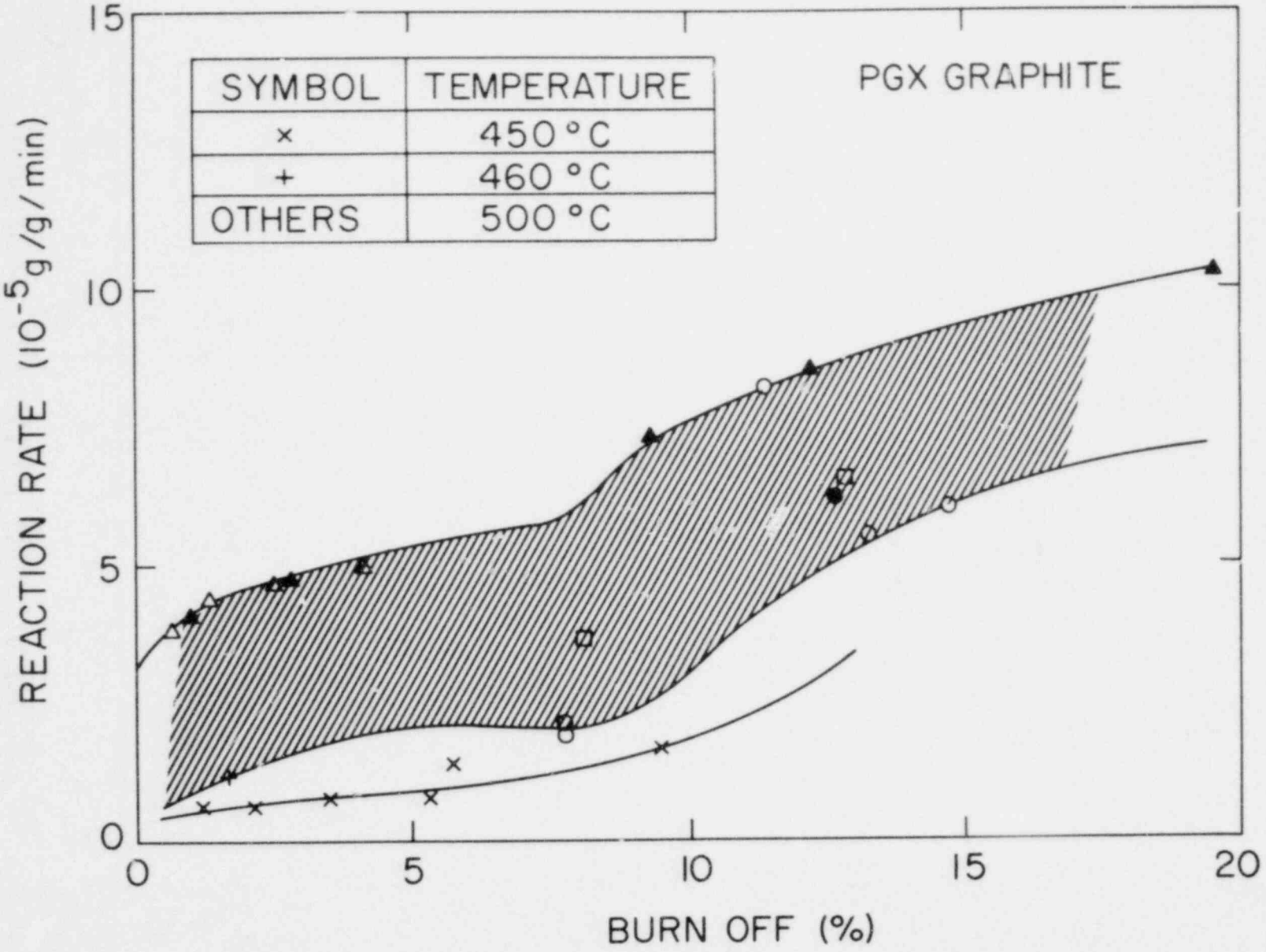

Figure 1.7. Plots of reaction rate versus burnoff for PGX graphite oxidized in air at 450 to 500°C.

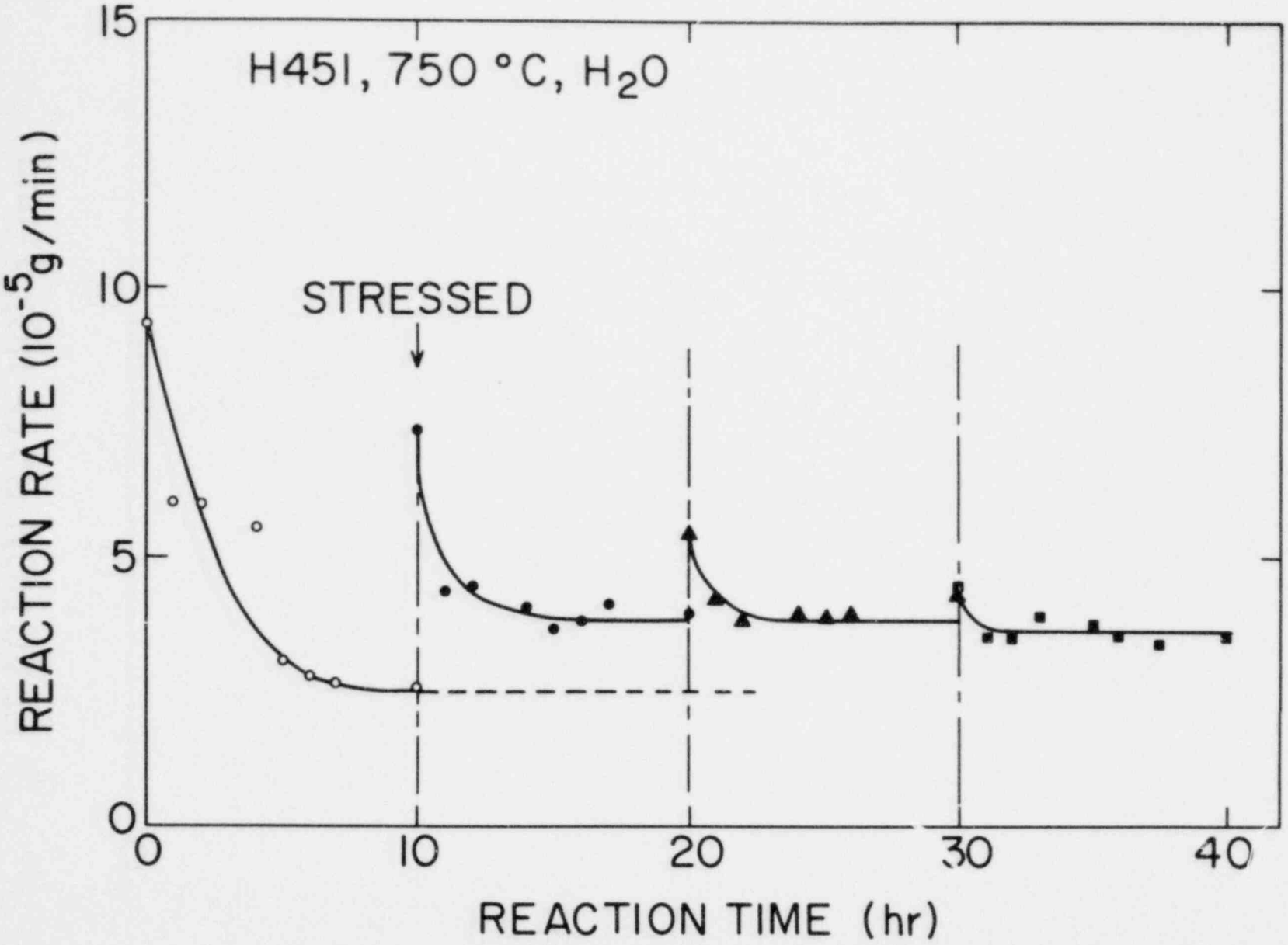

Figure 1.8. Effect of stressing a specimen of H451 graphite on its rate of reaction with 2% H_2O in He at 750°C. The specimen was weighed at room temperature every ten hours as indicated by dashed vertical lines. The reaction rate did not change from 40 hours to 70 hours (not shown).

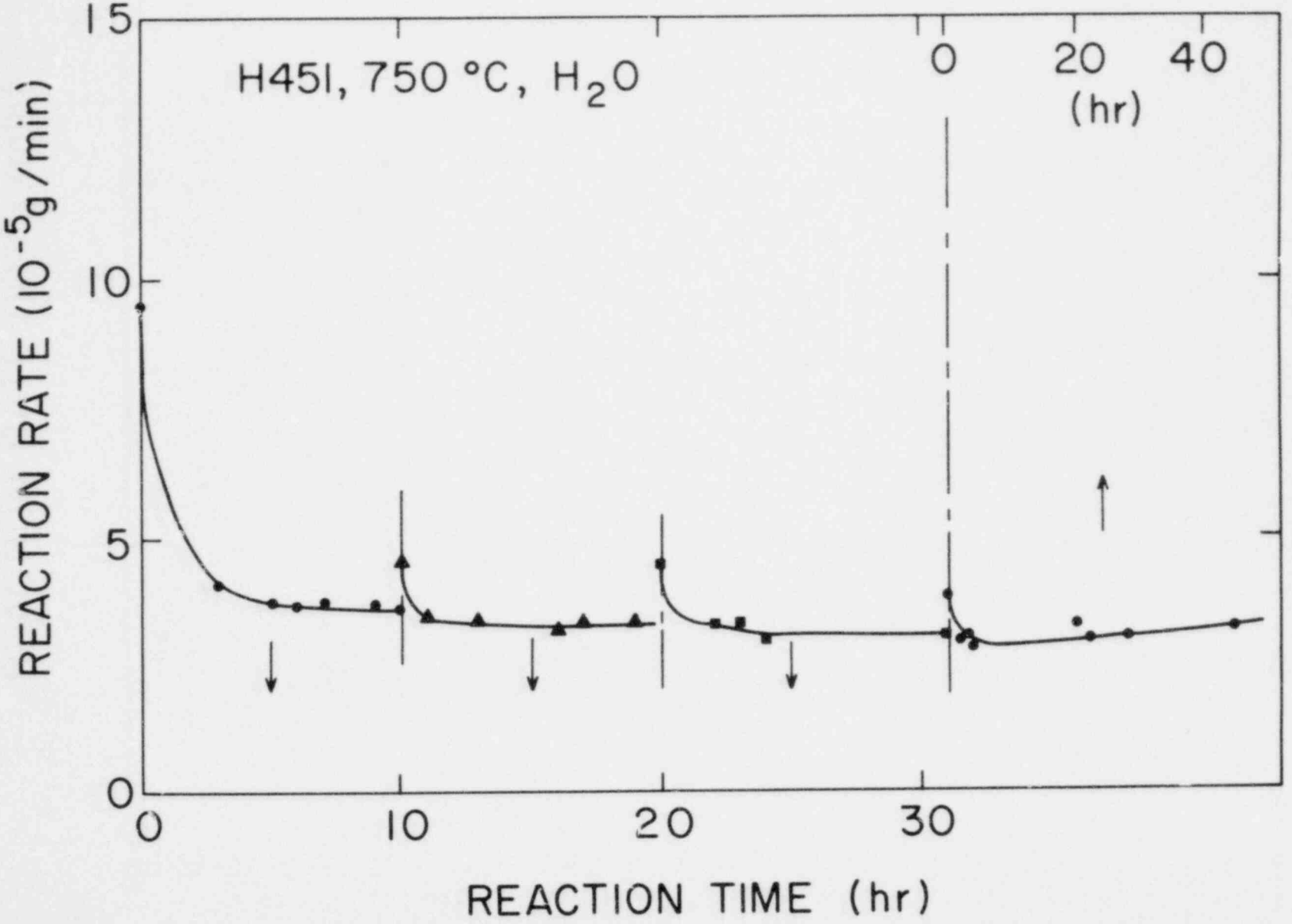

Figure 1.9. Reaction rate of a prestressed H451 specimen shown as a function of reaction time. The specimen was weighed at room temperature every ten hours as indicated by fine vertical lines.

tion rate, strength and stress applied before or during oxidation. Compressive strength of the specimens oxidized in this quarter under various experimental conditions will be measured in the next quarter.

1.3 The Characterization of Nuclear Graphites (F. B. Growcock, J. H. Heiser, III, D. G. Schweitzer)

The small scale study of the non-destructive oxidation/reduction/oxidation (ORO) method of monitoring iron concentration in large specimens of PGX graphite is continuing. Temporarily it supersedes the study of oxidation of graphite near equilibrium; the latter, however, will be resumed during the following quarter.

The recurring failure to reproducibly observe integrated weight changes of only 0.5-1.0 milligrams in 2 gram specimens of PGX graphite over several hours has led us to abandon this part of the project and continue with the second phase.

Specimens of PGX graphite weighing ca. 150 grams are oxidized and reduced in a tube furnace and the products are monitored via gas chromatography (gc). He and H_2 are purified during an experiment over 13X molecular sieves maintained at 77°K. A specimen is oxidized at 723°K with 2% H_2O in He flowing at 100 sccm until the reaction product, H_2, is being formed in immeasurably small amounts (<20 ppm). The oxidation is continued for 1 hour, after which the specimen is exposed to He for 1 hour to remove adsorbed oxides, then quenched and weighed. It is subsequently heated to 1073°K in He to remove high temperature adsorbates, quenched, weighed again and reheated in He to 1073°K; He is replaced with H_2 and the products CO and CH_4 are integrated over the duration of the reduction. The specimen is weighed and oxidized as in the first step.

Results obtained with an EL-2 specimen are presented in Table 1.3.

Table 1.3. Results of ORO Iron Monitoring Experiments
Iron concentration, ppm

	Mössbauer Spectroscopy	Gas Chromatography	Adjusted Weight Change
Oxidation	------	∿ 576	605
Reduction	750 ± 50	∿ 233	913
Oxidation	------	144	680
Reduction	------	123	426

The "Adjusted Weight Change" values are independent of the "Gas Chromatography" values, so that the former are not corrected for CH_4 formation during reduction. The agreement between the gc and weight change results is poor. Carbide formation during reduction may be the cause. To minimize this possibility and reduce the contribution made by CH_4, reduction will be done at lower temperatures. These experiments will be continued for a few weeks.

PUBLICATIONS

GROWCOCK, F. B. and HEISER, J., "The Removal of Iron from Impure Graphites," in Extended Abstracts and Program of the 14th Biennial Conference on Carbon, June 25-29, 1979, The Pennsylvania State University, p. 459.

REFERENCES

ANDREW, J. F., OKADA, J. and WOBSCHALL, D. C. in Proceedings of 4th Carbon Conference, Buffalo, 1959, Pergamon Press, 1960, p. 559.

BEAVAN, L. A., in Extended Abstracts and Program of the 14th Biennial Conference on Carbon, June 25-29, 1979, The Pennsylvania State University, p. 469.

BOARD, J. A. and SQUIRES, R. L. in Proceedings 2nd Conference on Industrial Carbon and Graphite, Soc. Chem. Industry, London, 1966, p. 289.

ENGLE, G. B. and BEAVAN, L. A., "Properties of Unirradiated Graphites PGX, HLM, and 2020 for Support and Permanent Side Reflector LHTGR Components," General Atomic Co., GA-A14646, June 1978.

ETO, M. and GROWCOCK, F. B., "Strength of Oxidized Nuclear Graphites Subjected to Stress and Prestress," in Reactor Safety Research Programs Quarterly Progress Report, April 1-June 30, 1979, Brookhaven National Laboratory, BNL-NUREG-51082, 1979.

EVERETT, M. R., KINSEY, D. V. and RÖMBERG, E., Chemistry and Physics of Carbon, Vol. 3, P. L. Walker, Editor, Marcel Dekker, New York, 1967, p. 147.

GILLIN, L. M., J. Nucl. Mater. 23, 280 (1967).

GROWCOCK, F. B. and HEISER, J., "Compressive Strength of Oxidized PGX Graphite," in Reactor Safety Research Programs Quarterly Progress Report, January 1-March 31, 1979, Brookhaven National Laboratory, BNL-NUREG-51014, May 1979.

JENKINS, G. M., Brit. J. Appl. Phys. 13, 30 (1962); J. Nucl. Mater. 29, No. 3, 322 (1969).

TAYLOR, R., et al, Carbon 5, 519 (1967).

VELASQUEZ, C., HIGHTOWER, G. and BURNETTE, R., "The Oxidation of H451 Graphite by Steam, Part I: Reaction Kinetics," General Atomic Co., GA-A14951, August 1978.

WALKER, P. L., Jr., RUSINKO, F., Jr. and AUSTIN, L. G., Advan. Catalysis 11, 133 (1959).

2. Materials, Chemistry, and Instrumentation

This program covers the evaluation of four main categories of materials: (1) metallic materials, (2) graphites, (3) PCRV, and (4) other materials. Included in (4) are control rod materials and thermal barrier insulation. At this time, however, the major emphasis is centered on metals. The objectives of the work are to critically review available materials data pertinent to HTGR safety, identify areas where information is sparse or unavailable, and to design and initiate experiments to yield data which will permit accurate assessments to be made of materials related safety problems.

2.1 Fatigue of Structural Materials (P. Soo, J. Chow, R. Sabatini, J. Hare)

The current effort on fatigue is focused on the high cycle fatigue regime to evaluate the behavior of components subjected to rapidly oscillating stresses. Tests are conducted in air and a simulated HTGR helium environment under load control at a cycling rate of 40 Hz. Six Material Test Systems (MTS) closed loop electrohydraulic fatigue machines are being used in the program. At this time 5 units are being used for in-helium testing. Test gas is supplied from the Materials Test Loop (MTL). Recent examination of the Panametrics Model 2000 probe, which is used in the MTL to monitor and control the moisture level, has shown it to be faulty. A series of calibration runs was, therefore, carried out using an EG&G Model 440 dewpoint hygrometer and an upwardly revised moisture level of 2500 μatm. of water has now been validated. This new moisture level is applicable to all of the fatigue and creep data reported in the HTGR program. The total impurities in the test helium gas include 2500 μatm. H_2O, 200 μatm. H_2, 40 μatm. CO, 20 μatm. CH_4 and 10 μatm. CO_2. Chemistries of the test alloys are given below:

	C	P	S	Mn	Si	Cr	Ni	Mo	Fe	Others
Incoloy 800H (Ht. HH7427A)	0.05	NA	0.003	0.67	0.46	19.83	32.17	NA	Bal.	0.65 Cu 0.43 Ti 0.39 Al
Hastelloy X (Ht. 4-2809)	0.11	0.021	0.008	0.50	0.41	20.67	Bal.	8.86	18.66	2.10 Co 0.55 W
2 1/4 Cr-1Mo	0.14	0.012	0.016	0.57	0.37	2.2	0.16	0.92	Bal.	

NOTE: NA = not analyzed. All concentrations in weight percent.

2.1.1 Incoloy 800H High Cycle Fatigue Testing

Detailed analyses of thermally aged specimens have recently been completed. Pretest thermal aging in the helium test gas was carried out at a temperature of 760°C (1400°F) for aging times of 1500, 3000 and 6000 hours. Samples having short test times were compared to those having long test times to determine whether the stress level significantly changed the mode of failure. Figure 2.1 shows fractographs for in-helium tests and also air tests to determine if environmental conditions are significant. All of the failed specimens showed a tendency for the

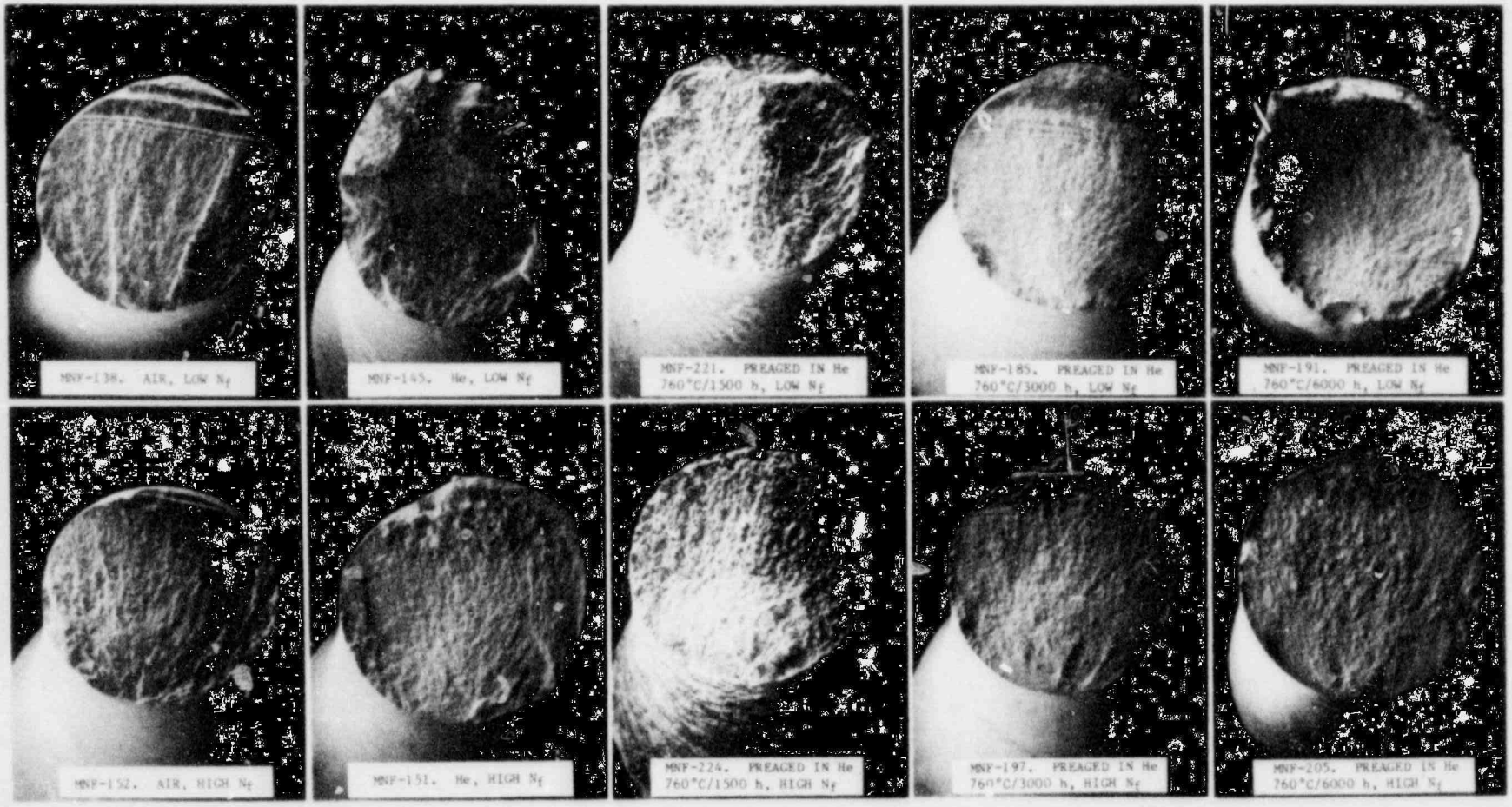

FRACTOGRAPHS OF INCOLOY 800H HIGH CYCLE FATIGUE SPECIMENS TESTED AT 760°C (1400°F) FOR VARIOUS TEST ENVIRONMENTS AND STRESS LEVELS. MAGNIFICATIONS APPROXIMATELY 6X.

Figure 2.1

fatigue cracks to propagate reasonably uniformly throughout the cross section, leading to a "chisel edge" where final separation occurs. For the high stress (low N_f) samples there is distinct evidence that crack initiation may occur simultaneously in different locations. In Specimen MNF-138, for example, 3 cracks initially began to propagate and eventually linked to form a single uniform crack. Specimer MNF-191 has a scalloped edge on the fracture surface which seems to have resulted from several small cracks. The initiation points for the main cracks are shown in Figure 2.2. No distinct feature causing the crack to form could be distinguished and all cracks were usually nucleated at the surface. In the vicinity of the initiation point, however, the moving crack forms a sharp step discontinuity parallel to the crack propagation direction, which is upward in Figure 2.2.

Fatigue striations are usually observed as shown in Figure 2.3 although they are indistinct, with the exception of the 1500-hour aged specimens. Secondary cracks in the fracture surface are common in the aged specimens. In the area where final separation occurs dimple formation is observed in the fracture surface (Figure 2.4). They are most prominent in air tested samples and those preaged for 1500 hours at 760°C (1400°F). Probably, the high concentrations of dimples observed in the 3000- and 6000-hour aged samples are associated with the larger numbers of precipitated carbides which act as nucleii for dimple formation. There does not appear to be any noticeable difference in the nature of the dimples for the high and low stress conditions.

An interesting feature in most fracture surfaces is the presence of small densely packed particles (Figure 2.5). Some specimens also display whiskers (Specimen MNF-224). It is speculated that these are metal oxides formed in the fracture surface after failure had occurred.

In order to correlate surface oxidation effects with fatigue strength, selected specimens were sectioned, polished and examined with an optical microscope (Figure 2.6). Long and short term tests were evaluated to determine whether stress levels influenced the nature of failure. For short term unaged specimens (tested in air or helium) a cold worked surface layer is observed (Specimens MNF-138 and MNF-145) which resulted from surface grinding of the gagelength during specimen fabrication. For longer term tests recrystallization of the surface layer occurs (Specimens MNF-151 and MNF-152).

For the intermediate aging time of 1500 hours an interesting observation is that very small grains nucleate in the surface zone (MNF-221) and deep intergranular fatigue cracks are present after short test times. For long term tests on 1500-hour aged specimens (MNF-224) deep intergranular cracks are again formed and there is a very large increase in the depth of oxidation. It was found that in Specimen MNF-224 this depth is significantly decreased in regions away from the highly stressed narrow part of the contoured gagelength. It seems that for the 1500-hour aged condition there is considerable stress assisted intergranular penetration down grain boundaries. Since the grains at the surface are very small due to recrystallization, the overall effect is an acceleration of oxygen penetration into the specimen as shown in Specimen MNF-224.

The tendency for deep intergranular attack in the 1500-hour aged specimens is in accord with the large decrease in fatigue strength described in the last

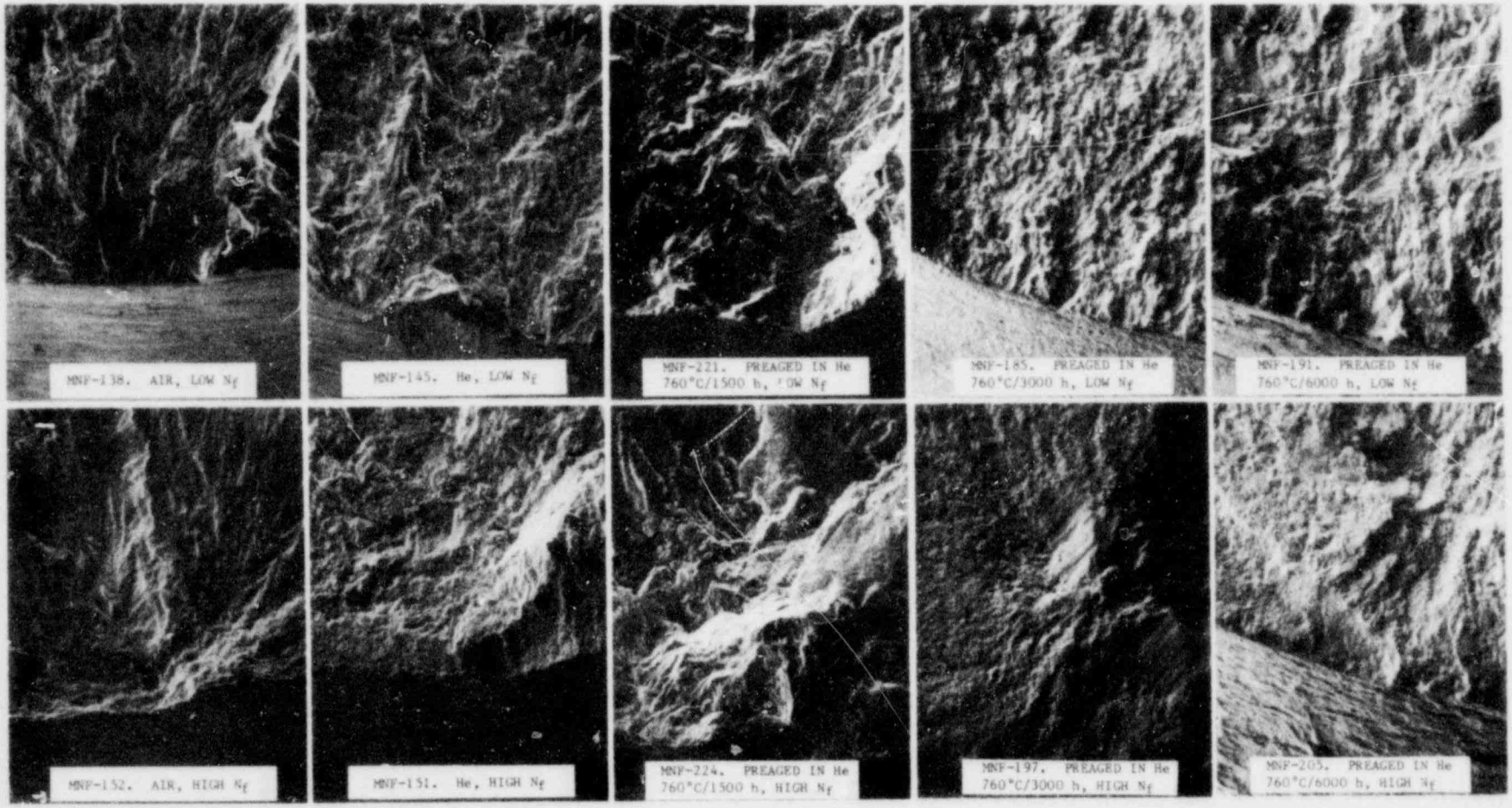

CRACK INITIATION POINTS IN INCOLOY 800H HIGH CYCLE FATIGUE SPECIMENS TESTED AT 760°C (1400°F) FOR VARIOUS TEST ENVIRONMENTS AND STRESS LEVELS. MAGNIFICATIONS 60X.

Figure 2.2

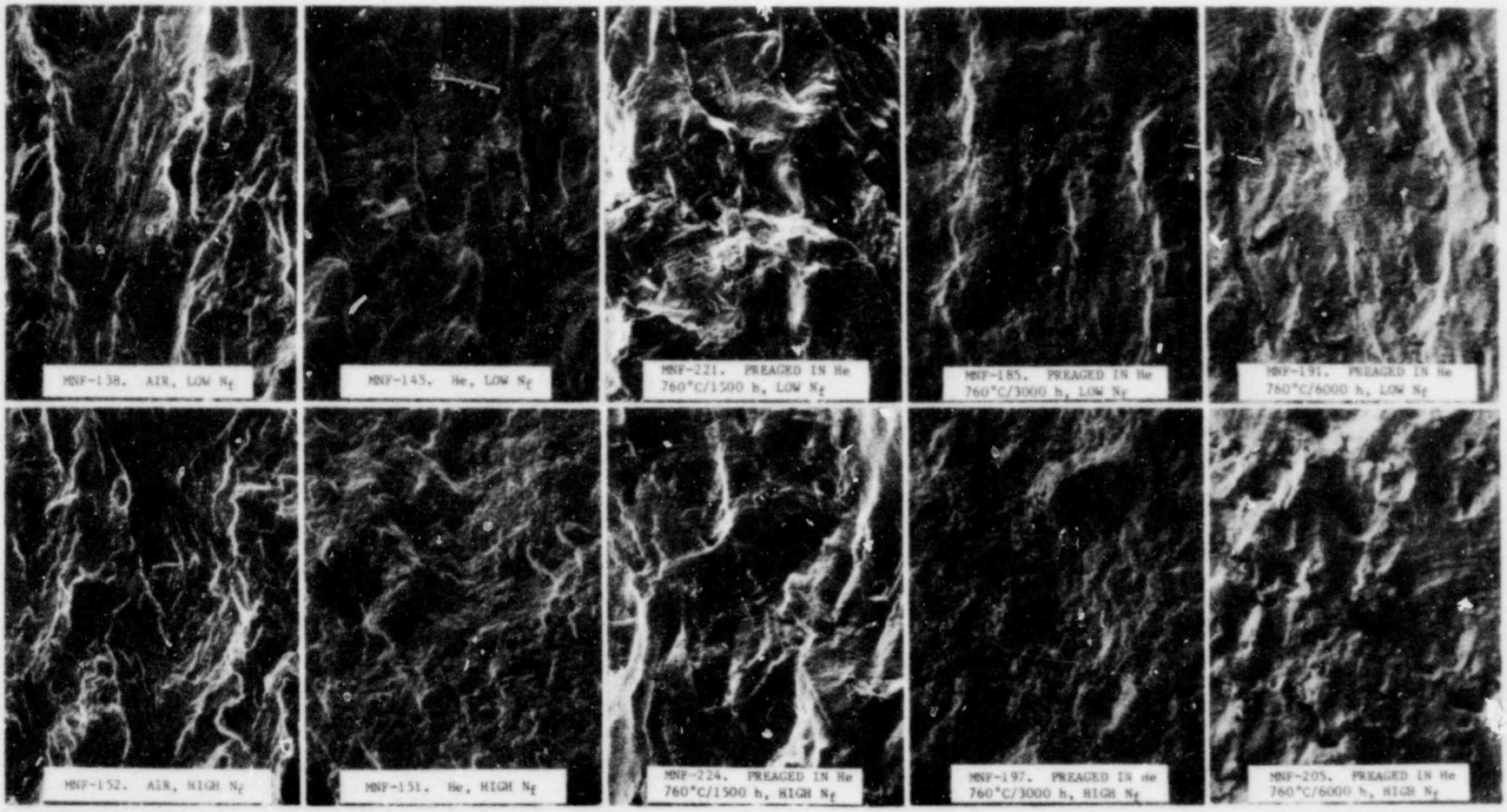

STRIATIONS IN INCOLOY 800H HIGH CYCLE FATIGUE SPECIMENS TESTED AT 760°C (1400°F) FOR VARIOUS TEST ENVIRONMENTS AND STRESS LEVELS. MAGNIFICATIONS 150X.

Figure 2.3

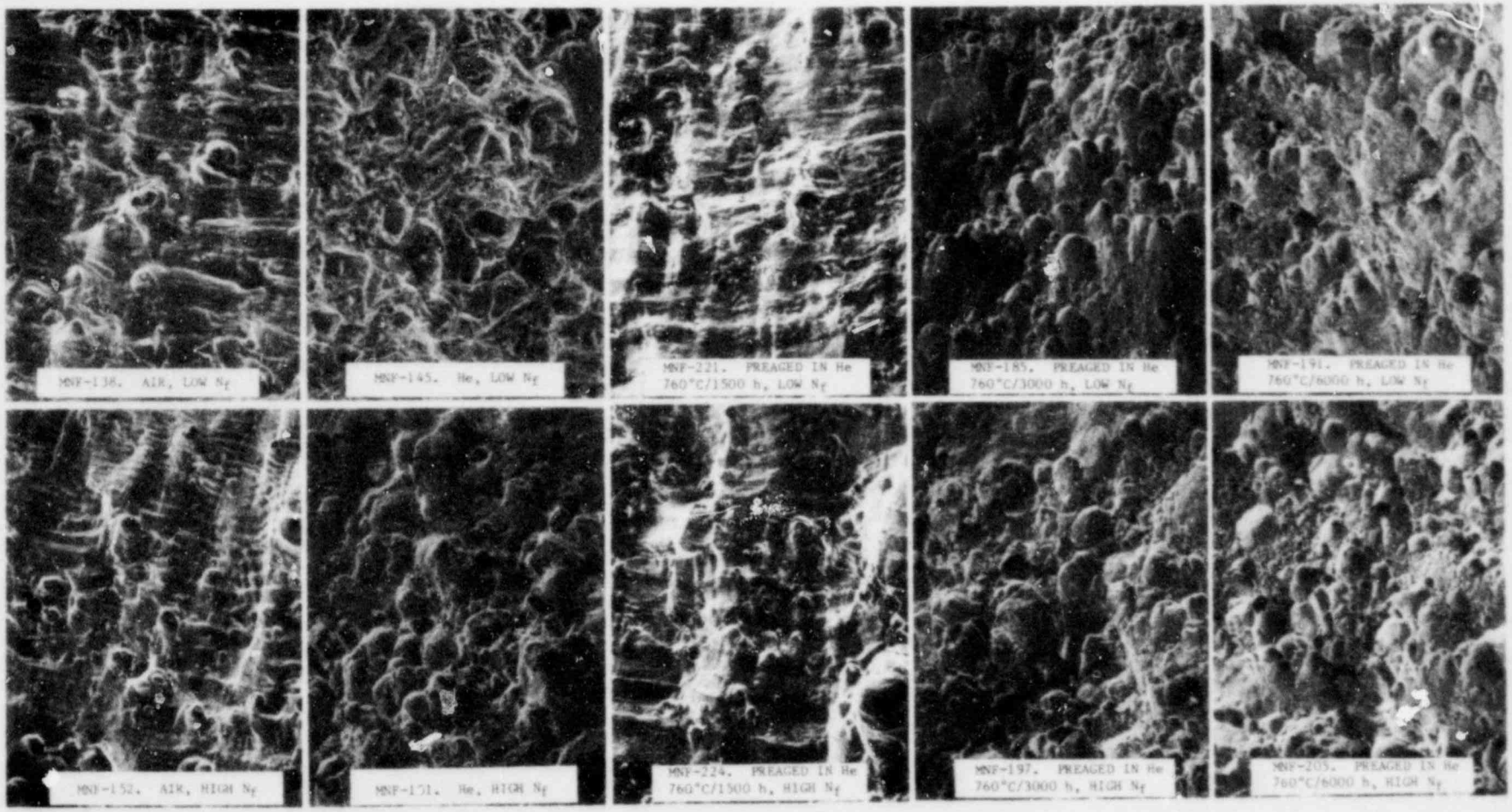

STAGE III DIMPLE FORMATION IN INCOLOY 800H HIGH CYCLE FATIGUE SPECIMENS TESTED AT 760°C (1400°F) FOR VARIOUS TEST ENVIRONMENTS AND STRESS LEVELS. MAGNIFICATIONS 150X.

Figure 2.4

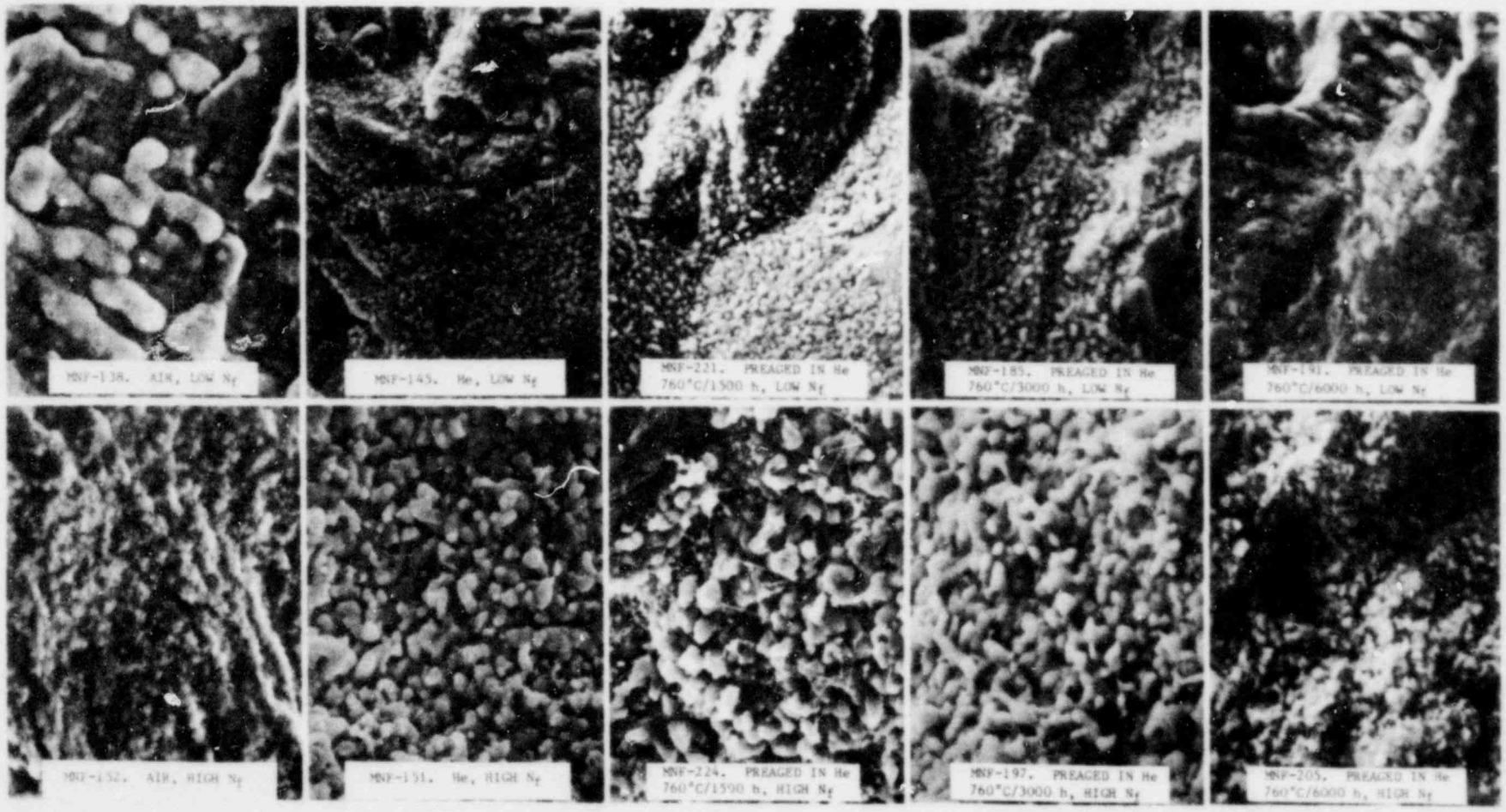

OXIDATION PRODUCTS IN FRACTURE SURFACES OF INCOLOY 800H HIGH CYCLE FATIGUE SPECIMENS TESTED AT 760°C (1400°F) FOR VARIOUS TEST ENVIRONMENTS AND STRESS LEVELS. MAGNIFICATIONS 1400X.

Figure 2.5

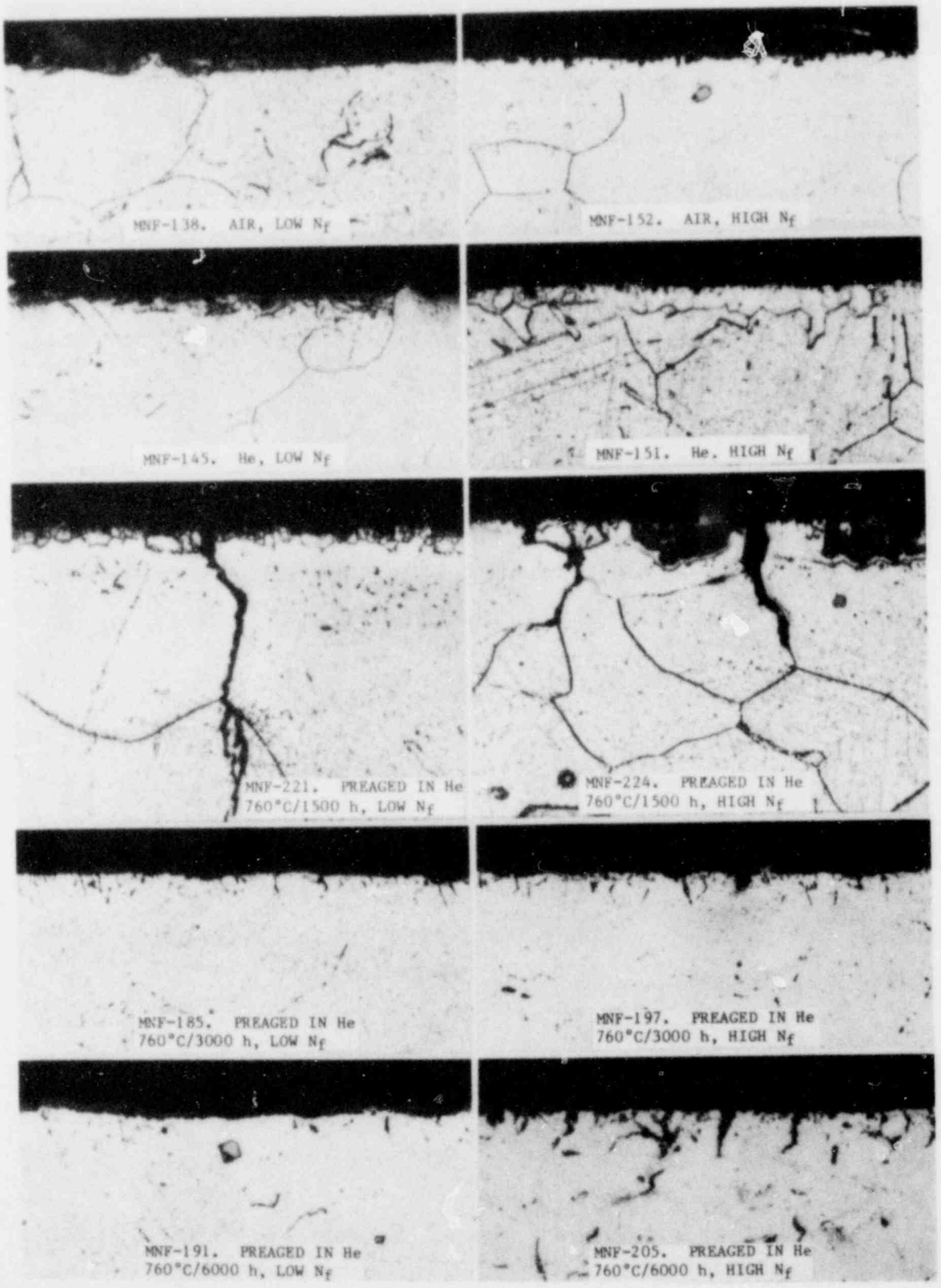

RECRYSTALLIZATION AND CRACKING IN INCOLOY 800H HIGH CYCLE FATIGUE SPECIMENS FOR VARIOUS TEST ENVIRONMENTS AND STRESS LEVELS. MAGNIFICATIONS 350X.

Figure 2.6

quarterly report (Soo, 1979).

Figure 2.6 shows that for longer aging times of 3000 and 6000 hours the tendency toward rapid stress assisted surface oxidation disappears. No deep general oxygen penetration is noticed although the intergranular cracks in the 6000-hour aged specimen are about twice as deep as those in the 3000-hour aged specimen.

Scanning electron microscope/microprobe scans were carried out across sectioned fatigue specimens as shown in Figure 2.7. The very thick oxidized region is clearly shown for the 1500-hour aged specimens. At the longer aging times considerable intergranular attack is noticed below the oxide scale. However, the fatigue strength data shown previously (Soo, 1979) indicate that the samples aged for 6000 hours have a comparable strength to unaged material. Hence, the intergranular cracks formed in the aged material do not appear to detrimentally affect fatigue life by introducing embryonic cracks that promote early fatigue failure.

An examination of the chemical composition of the oxidized surface layers shows some very interesting features. Most of the specimens show a mixture of Cr and Mn surface oxides with the Mn being concentrated more closely to the surface. Concentrations of Ti and Al oxides are also found close to the surface. A pronounced exception to this behavior occurs for the 1500-hour aged specimen (MNF-224). The Cr and Mn oxide layers are still observable but these are overlaid by a thick nickel rich oxygen free layer. This in turn is overlaid by an iron oxide layer. Although the presence of Fe and Ni in the uppermost layers is most prominent in the 1500-hour aged material there is an indication that this behavior is present in the unaged specimens tested in helium (see Figure 2.7, Specimen MNF-151). Air tested specimens only show Cr and Mn oxides on the surface.

The reason for the presence of Fe oxide layers in the unaged and 1500-hour aged specimens tested in helium probably centers on the rapid formation of fresh metal surfaces during the recrystallization process in which the number of easily penetrated grain boundaries is greatly increased. This would permit much of the Cr and Mn to be oxidized at relatively large distances below the surface which would thus inhibit the formation of an unbroken protective Cr/Mn oxide layer on the surface. Iron in the vicinity of the surface would then also be exposed to moisture and Fe oxides could then form, as observed.

Knoop microhardness traverses were made across surfaces of polished specimens. Typical results are shown in Figure 2.8. As expected, residual surface cold work hardens the specimen surface. The compressive stresses formed are beneficial and give an increased fatigue strength (Soo, 1979). Thermal aging causes relaxation and recrystallization resulting in a softening of the surfaces, which partly explains why all of the aged samples were weaker than unaged material.

Figure 2.8 shows that although the 3000-hour and 6000-hour aged specimens show surface recrystallization and softening, they also display a general bulk strengthening which increases with aging time. This probably explains why the 6000-hour aged specimens have a fatigue strength close to that for unaged material, even though surface softening is present (Soo, 1979). Figure 2.9 is a

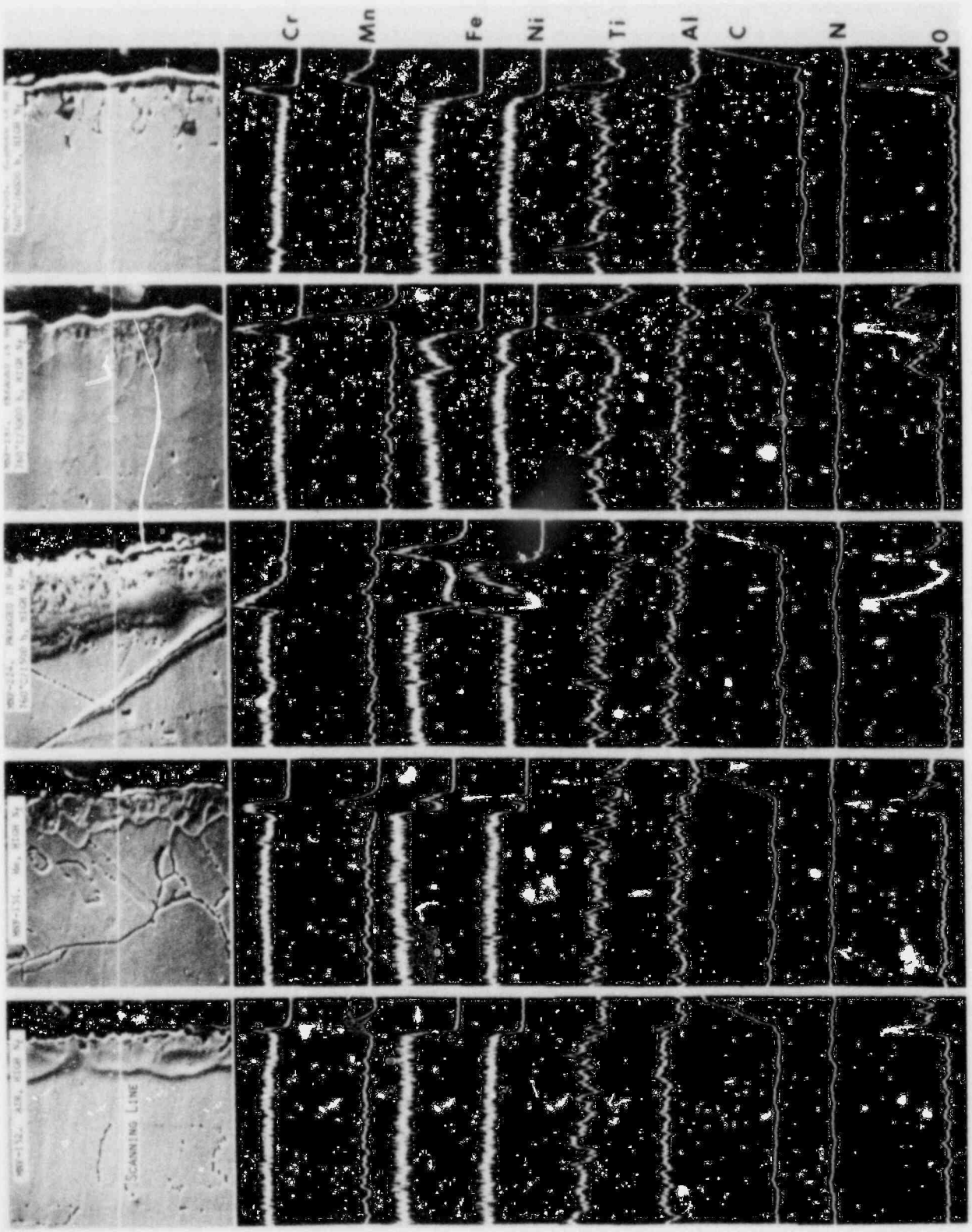

Scanning electron microscope microprobe scans thru the surfaces of Incoloy 800H high cycle fatigue specimens as a function of test environment and pretest thermal aging time. Aging and test temperature was 760°C (1400°F). Magnifications 425X.

Figure 2.7

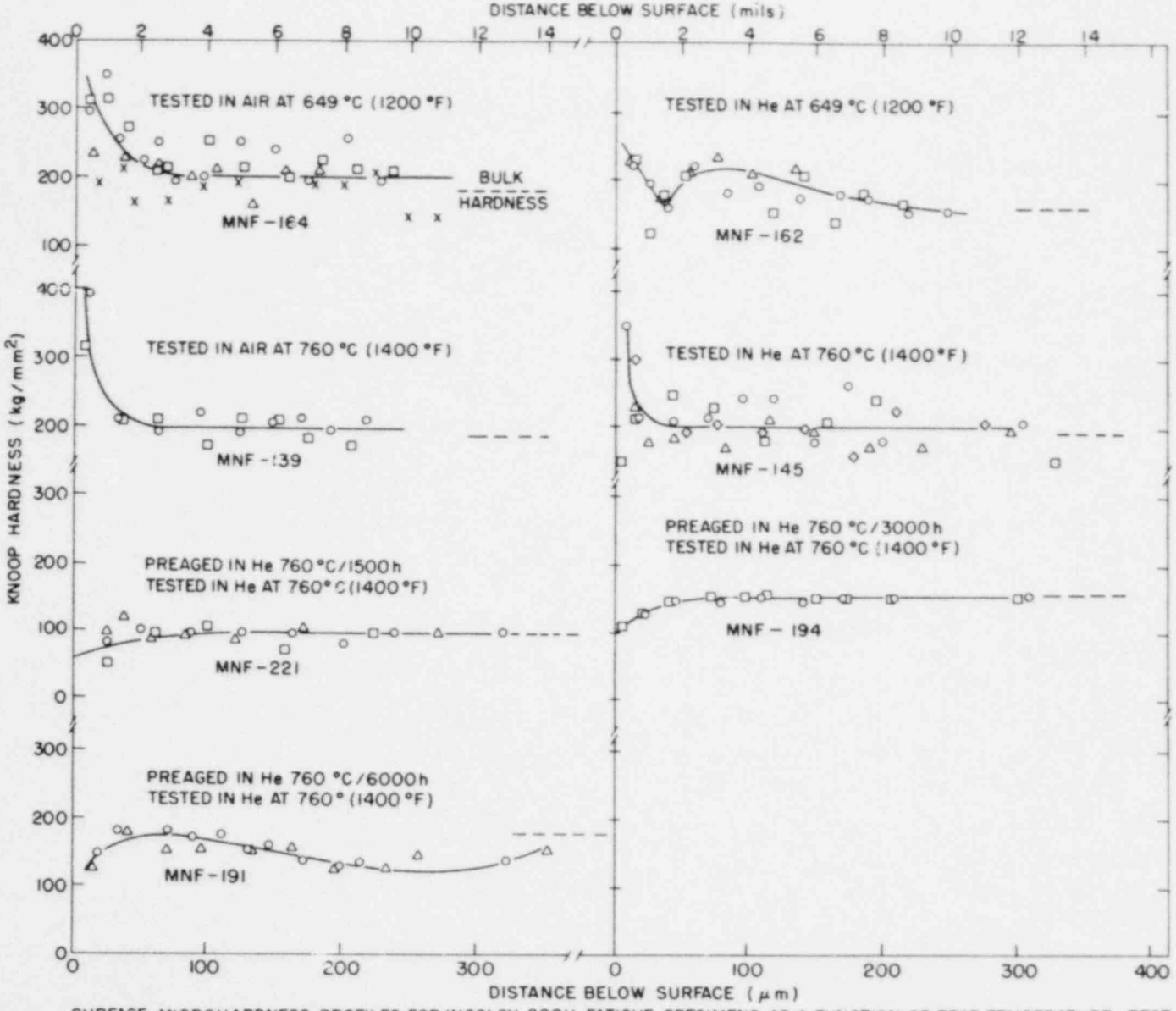

SURFACE MICROHARDNESS PROFILES FOR INCOLOY 800H FATIGUE SPECIMENS AS A FUNCTION OF TEST TEMPERATURE, TEST ENVIRONMENT AND THERMAL PREAGING TIME.

Figure 2.8

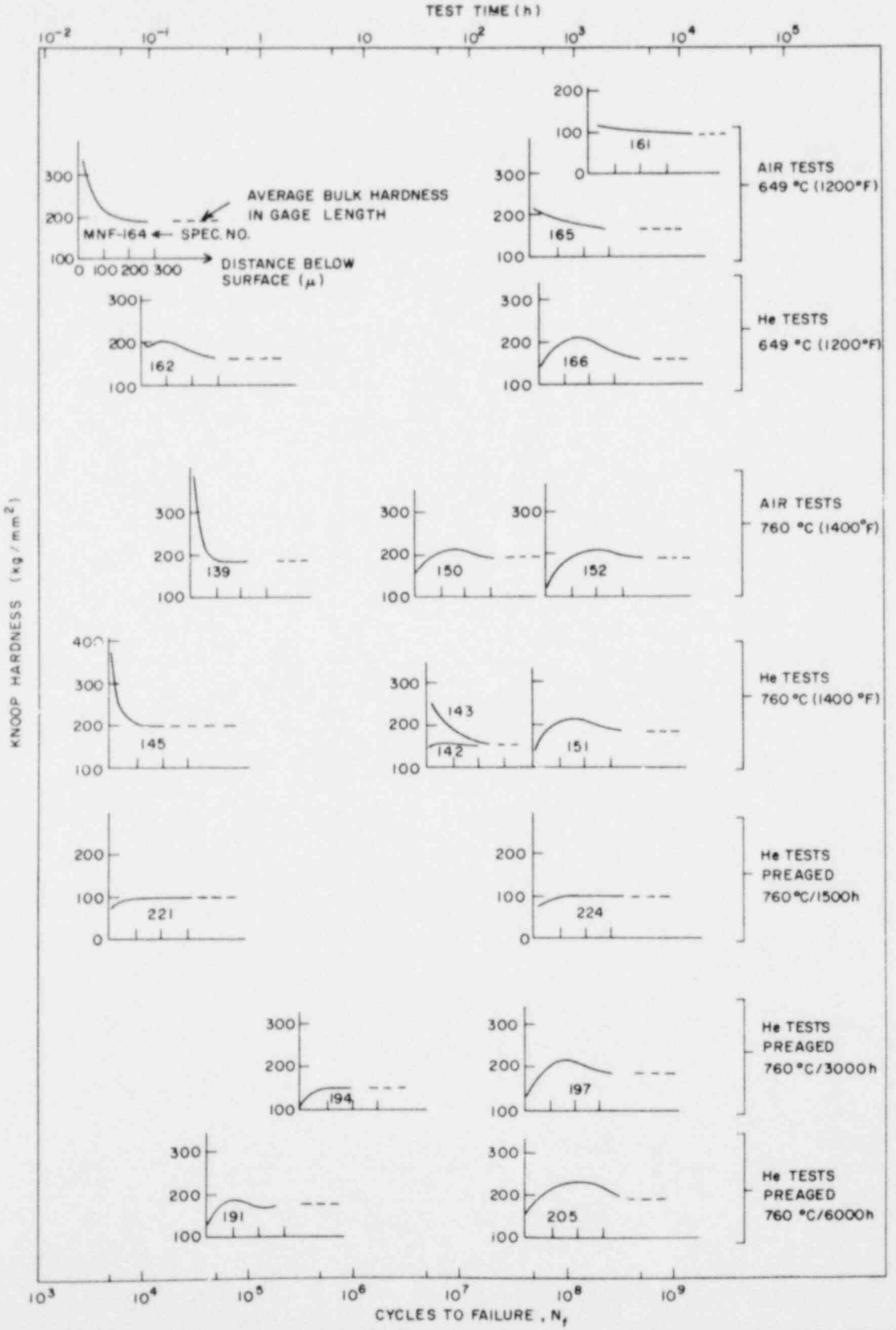

SCHEMATIC OF SURFACE HARDNESS PROFILES FOR INCOLOY 800H FATIGUE SPECIMENS AS A FUNCTION OF TEST TEMPERATURE, TEST ENVIRONMENT AND THERMAL PREAGING CONDITION.

Figure 2.9

more complete summary of the microhardness data for aged Incoloy 800H fatigue specimens.

Figure 2.10 shows the bulk (internal) hardness of Incoloy 800H fatigue specimens as a function of cyclic work hardening and pretest and in-test thermal exposures. The open symbols were hardness values taken from the shanks of fatigue specimens which are essentially unstressed. Note that the hardness remains at about 75 KHN for up to 1500 hours of aging at 760°C (1400°F), after which a rapid hardness increase occurs. Time-temperature-precipitation curves described by Orr (1978) suggest that this increase is a result of either TiC or $M_{23}C_6$ or, possibly, both. The γ' phase apparently does not appear until about 50,000 hours of aging at 760°C (1400°F) according to Orr's work. After approximately 4000 hours of aging the bulk hardness stabilizes.

The closed symbols in Figure 2.10 show the combined effects of aging and cyclic stresses on hardness. An average hardness value was obtained from at least 6 indentations close to the minimum diameter region of the contoured gagelength of failed specimens. Considerable scatter is observed for some of the aging conditions, reflecting the different cyclic stress levels used. It is clear, however, that the 1500-hour aged material is not as significantly work hardened as material aged for shorter and longer times. Again, this observation is compatible with the lower fatigue strength of the 1500-hour aged specimens.

Attempts to determine whether carbon and/or nitrogen transfer occurred at the surfaces of the fatigue specimens during aging and testing of the specimens were inconclusive. If such transfer does occur the scanning electron microscope/microprobe is not sufficiently sensitive to detect it. Note that the large increase in the carbon concentration near the specimen surface results from the presence of plastic used to mount the samples.

2.1.2 Hastelloy X High Cycle Fatigue Testing

The nature of fracture in Hastelloy X has been evaluated with the aid of a scanning electron microscope for a range of thermally aged conditions. As in the case of Incoloy 800H (Figure 2.11) there is a possibility that fatigue cracks initiate at different locations (Specimen MHF-46 shows two initiation points) but these eventually merge and a single crack propagates until complete failure occurs. Final failure occurs along a "chisel edge." In a few cases, internal crack initiation points are observed (Specimen MHF-59, Figure 2.12). There is no noticeable feature which could be identified as the cause of crack initiation; nor were there any significant differences in general fractographic appearance for the various thermal aging conditions and test environments.

Scanning electron microscope examinations were made in regions close to the centers of fractured surfaces. Striations, if present, were very finely spaced and diffuse. The air tested specimen (MHF-59, Figure 2.13) showed a slightly more irregular fracture surface and there appeared to be more dimple formation for the samples aged for longer times. The tendency for dimple formation is more marked in areas of the fracture surface close to the point of final separation (Figure 2.14).

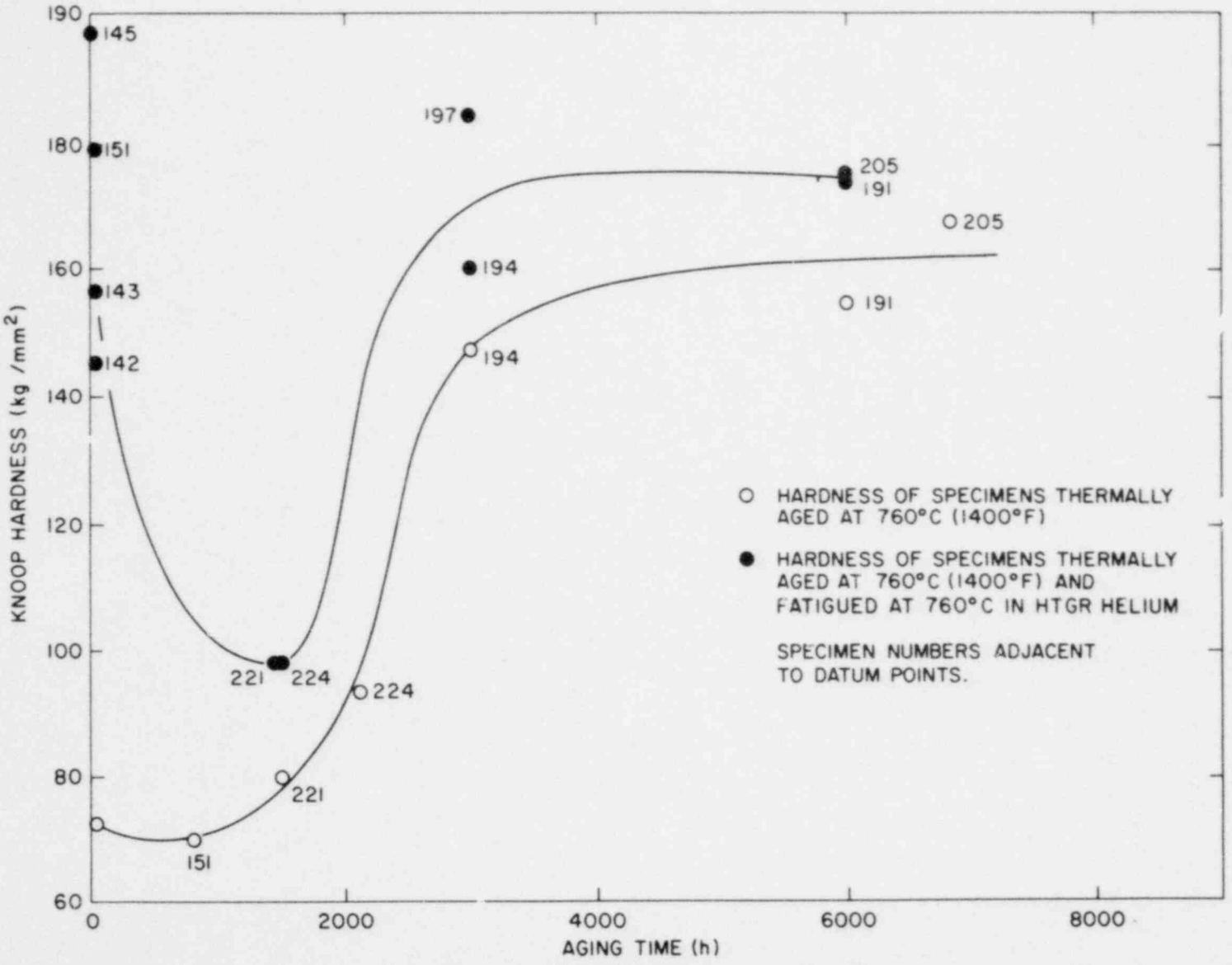

EFFECT OF THERMAL AGING AND CYCLIC STRESSING ON THE MICROHARDNESS OF INCOLOY 800H

Figure 2.10

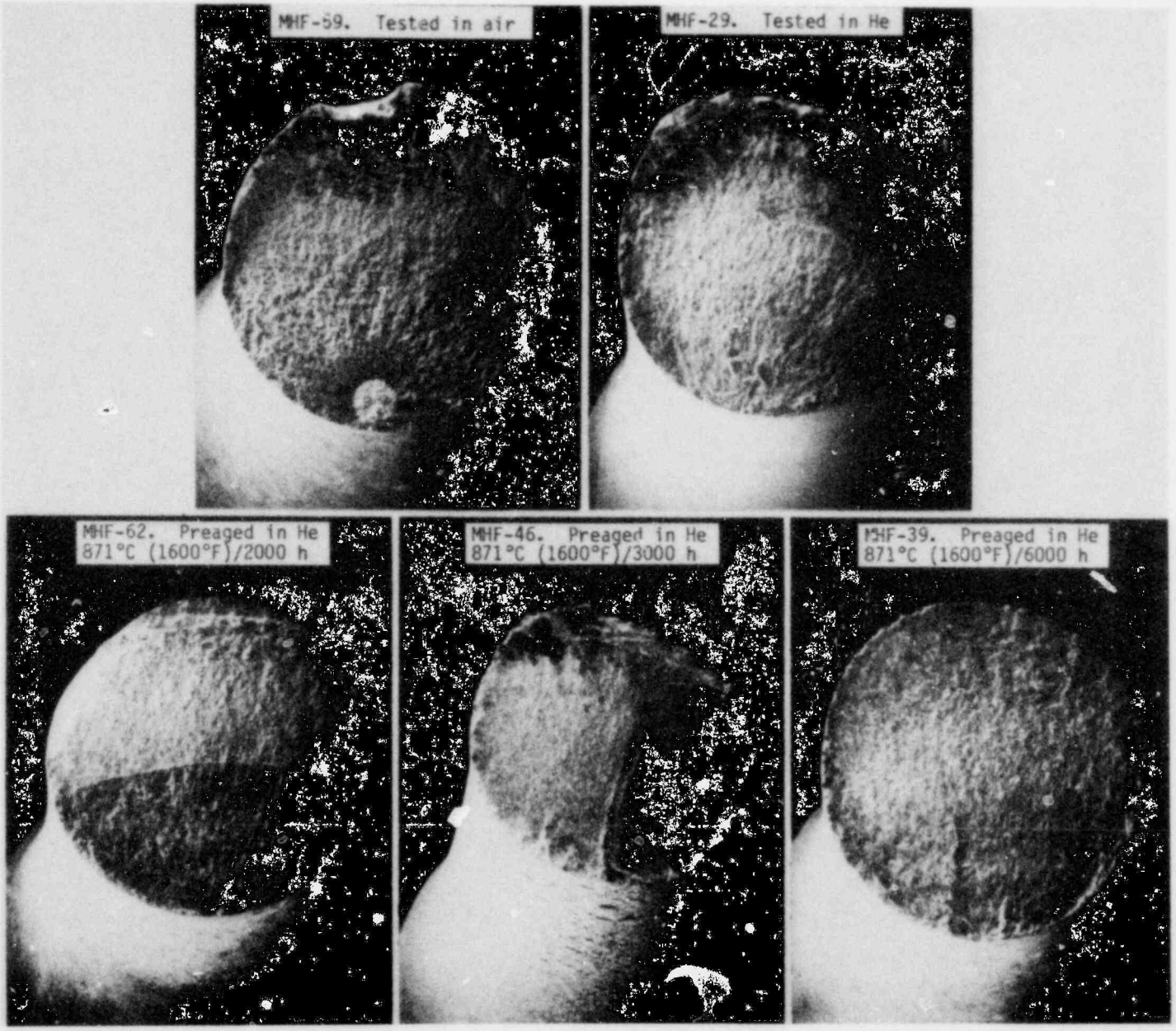

FRACTOGRAPHS OF HASTELLOY X HIGH CYCLE FATIGUE SPECIMENS TESTED AT 871°C (1600°F) AS A FUNCTION OF TEST ENVIRONMENT AND PRETEST THERMAL AGING TIME IN HTGR HELIUM. MAGNIFICATIONS APPROXIMATELY 8X.

Figure 2.11

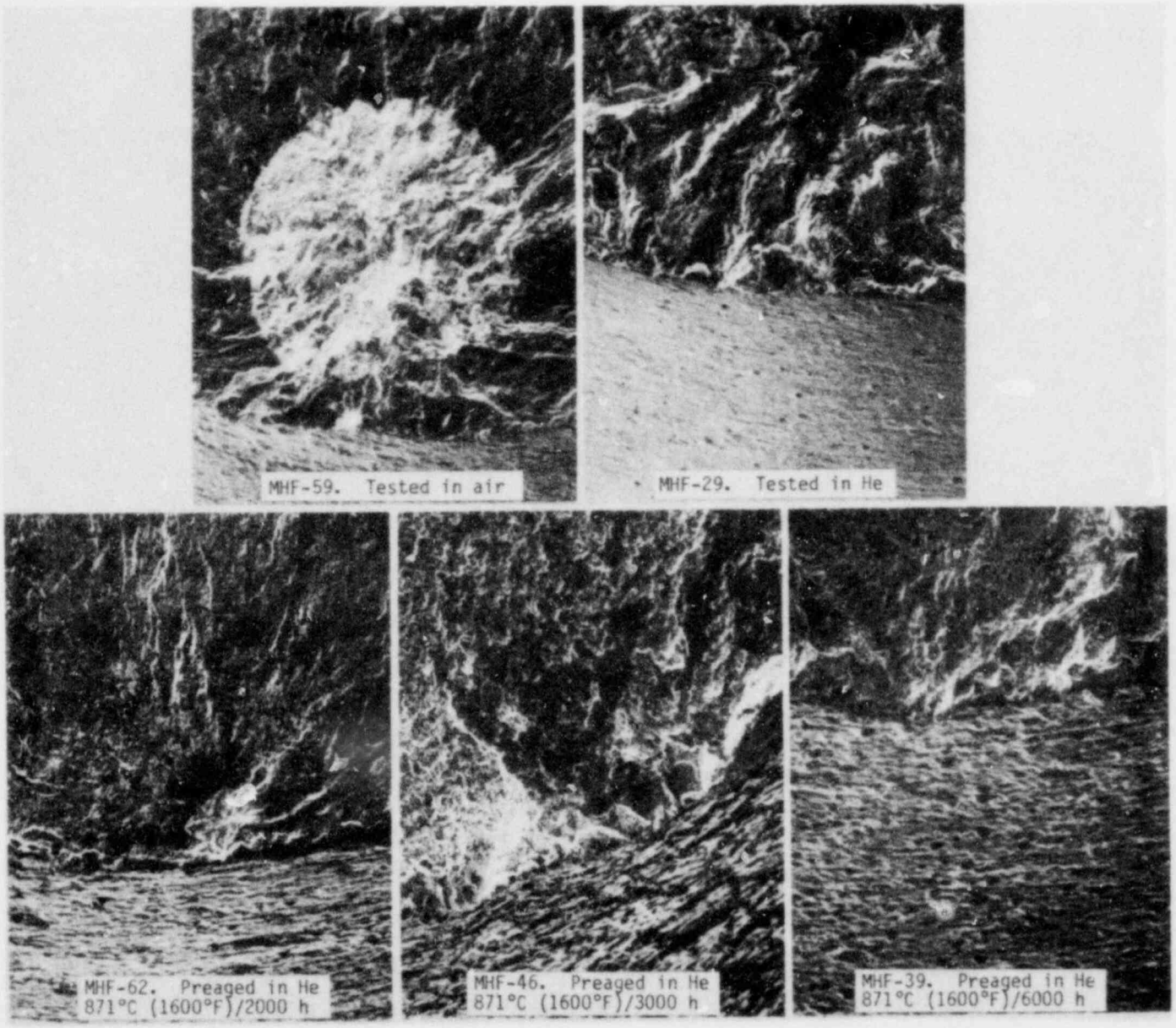

CRACK INITIATION POINTS IN HASTELLOY X HIGH CYCLE FATIGUE SPECIMENS TESTED AT 871°C (1600°F) AS A FUNCTION OF TEST ENVIRONMENT AND PRETEST THERMAL AGING TIME IN HTGR HELIUM. MAGNIFICATIONS 70X.

Figure 2.12

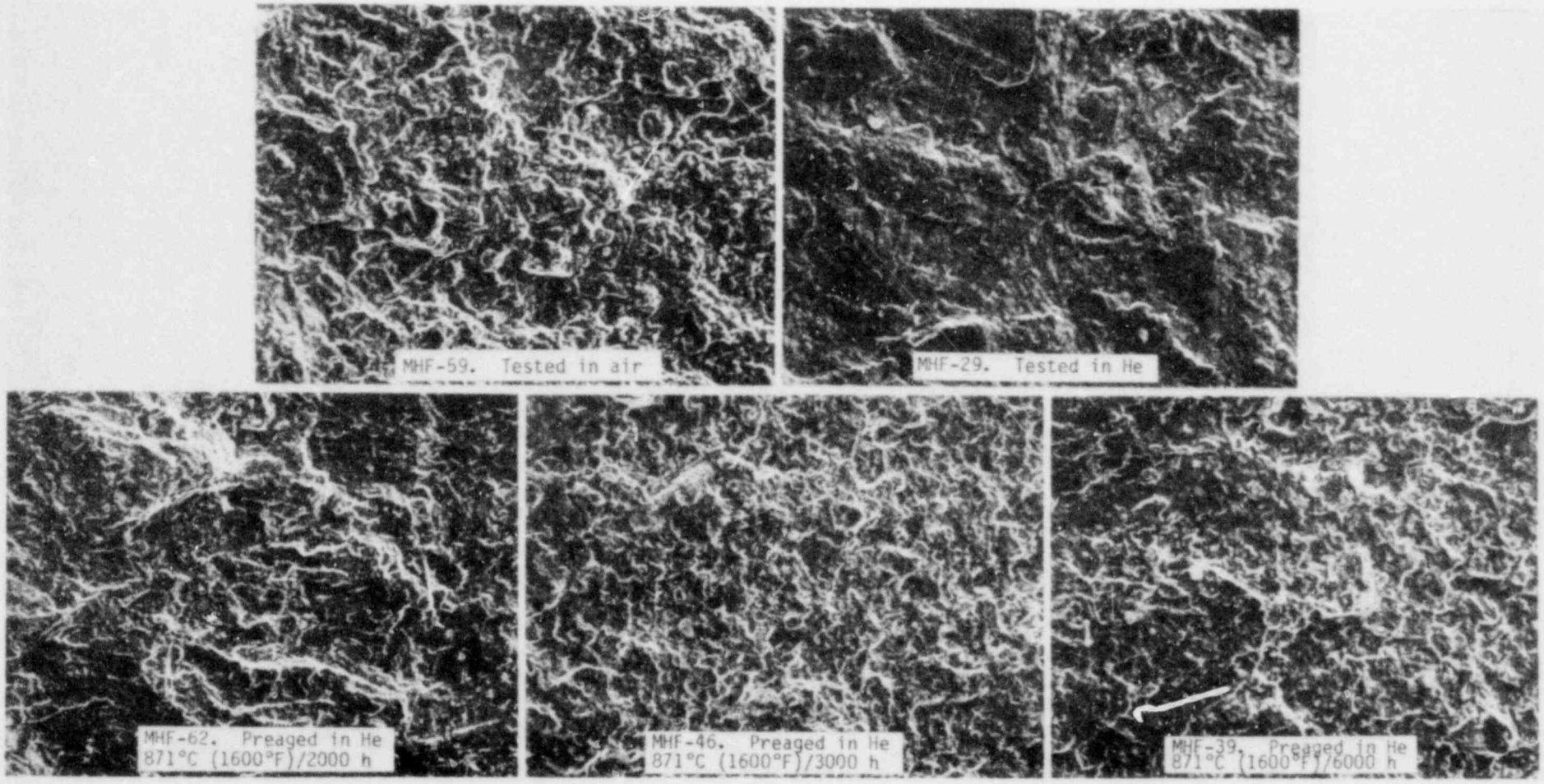

CENTERS OF FRACTURE SURFACES FOR HASTELLOY X HIGH CYCLE FATIGUE SPECIMENS TESTED AT 871°C (1600°F) AS A FUNCTION OF TEST ENVIRONMENT AND PRETEST THERMAL AGING TIME IN HTGR HELIUM. CRACK PROPAGATED FROM LEFT TO RIGHT. MAGNIFICATIONS 200X.

Figure 2.13

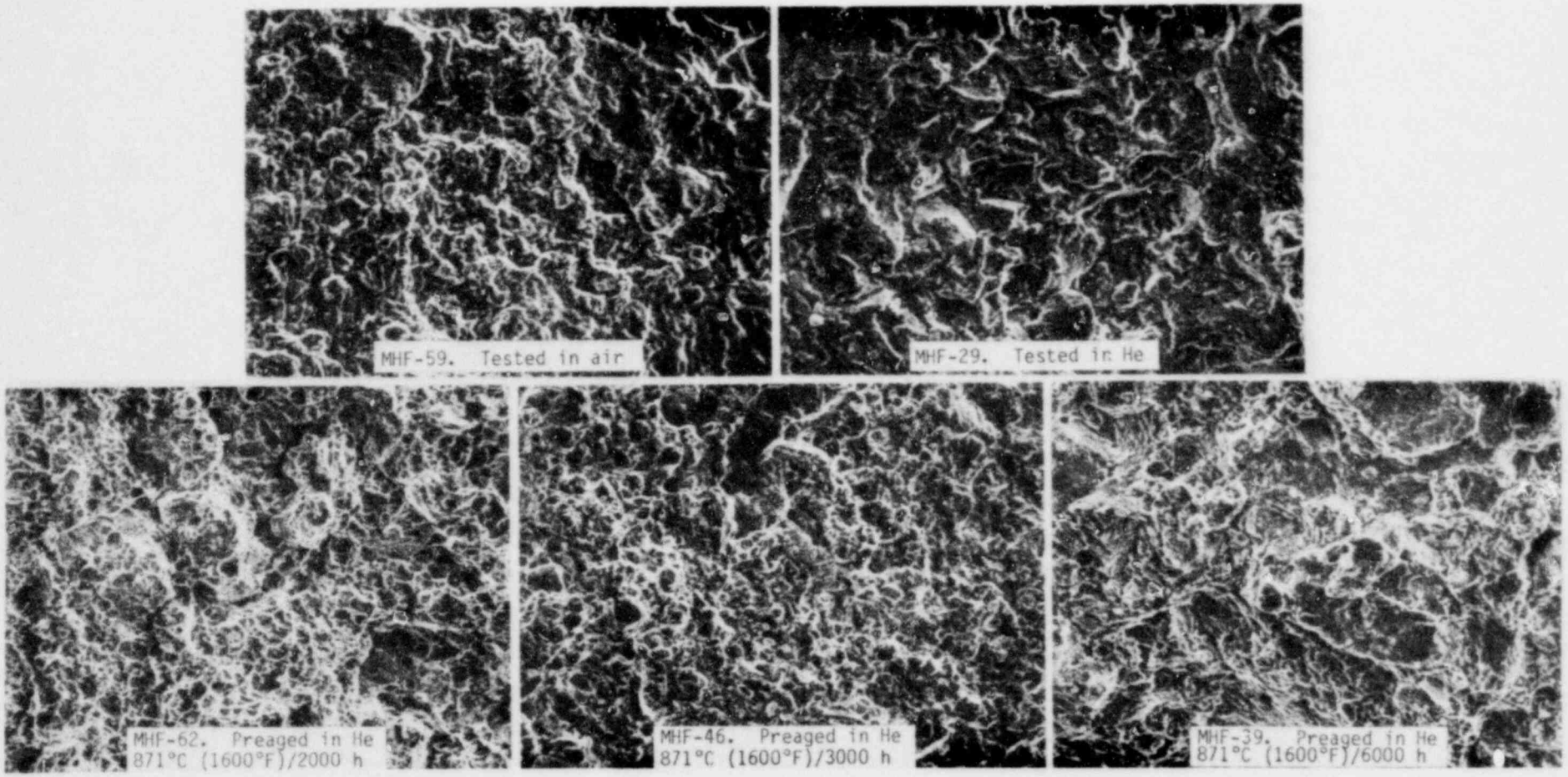

FRACTURE SURFACES NEAR AREAS OF FINAL SEPARATION FOR HASTELLOY X HIGH CYCLE FATIGUE SPECIMENS TESTED AT 871°C (1600°F) AS A FUNCTION OF TEST ENVIRONMENT AND PRETEST THERMAL AGING TIME IN HTGR HELIUM. CRACK PROPAGATED FROM LEFT TO RIGHT. MAGNIFICATIONS 200X.

Figure 2.14

Scanning electron microscope observations were made of the edges of fracture surfaces lying parallel to the crack propagation direction to examine the nature of corrosion during pretest thermal aging and in-test exposure to the test environments. For the two unaged specimens examined (MHF-59 tested in air and MHF-29 tested in helium, Figure 2.15) no distinctive scale formation was noticed. For the air tested specimen there appeared to be small cavities very close to the surface; these were not seen in the helium test. For the 2000-, 3000-, and 6000-hour aged specimens an oxide scale has formed which is apparently quite loosely adherent to the bulk material below. Cracks are readily noticed below the scale and they are deeper for the specimens aged for the longer times. These are connected with intergranular corrosive attack along the boundaries of small recrystallized surface grains (Soo, 1978). Most likely, these cracks directly contribute to the decrease in fatigue stregnth observed in the aged specimens (Soo, 1979). Additional evaluations of the effects of surface condition will be made on aged Hastelloy X specimens in future quarterly reports.

2.1.3 2 1/4Cr-1Mo Steel High Cycle Fatigue Testing

Annealed 2 1/4Cr-1Mo steel is being evaluated in an attempt to determine the behavior of steam generator tubes in HTGR helium environments. Figure 2.16 shows the results of all tests to date. For unaged materials the HTGR helium environment is significantly less detrimental to fatigue life compared to air. There is approximately a 20% difference in fatigue strength between specimens tested in the two gas environments. Pretest thermal aging in the helium test gas causes a very large decrease in fatigue strength. For a thermal aging time of 3000 hours the strength in helium is reduced to that for the air test condition. After 6000 hours of aging the strength is 10-20% below that for air.

The loss in fatigue strength is caused by severe decarburization of the sample during aging. The rapid decrease in the fatigue strength curve for unaged material tested in helium is also likely to be caused by the decarburization effect. Metallographic evidence to support this will be presented in future reports.

2.2 Creep Rupture Properties of Primary Circuit Structural Materials in Air and HTGR Helium (J. G. Y. Chow, P. Soo, K. Lee, C. Brewster)

Since many of the HTGR primary circuit components are inaccessible for replacement, they have to maintain their integrity over the design life of the reactor. Therefore, the long term mechanical properties of the materials used to construct these components are important safety considerations. These materials are exposed to helium containing impurities such as water vapor, CO, CO_2, H_2 and CH_4 which are present due to water influx from the steam generators. The objectives of this phase of our program are to study the long term mechanical behavior of the primary circuit metals in a prototypic HTGR helium environment and to assess the changes in properties compared to standard air testing.

The creep testing program has been concentrated on Hastelloy X which is the thermal barrier cover plate material in the highest temperature zones and on Incoloy 800H which is widely used in the construction of the steam generator. Materials from commercial heats of these two alloys were purchased in the form of

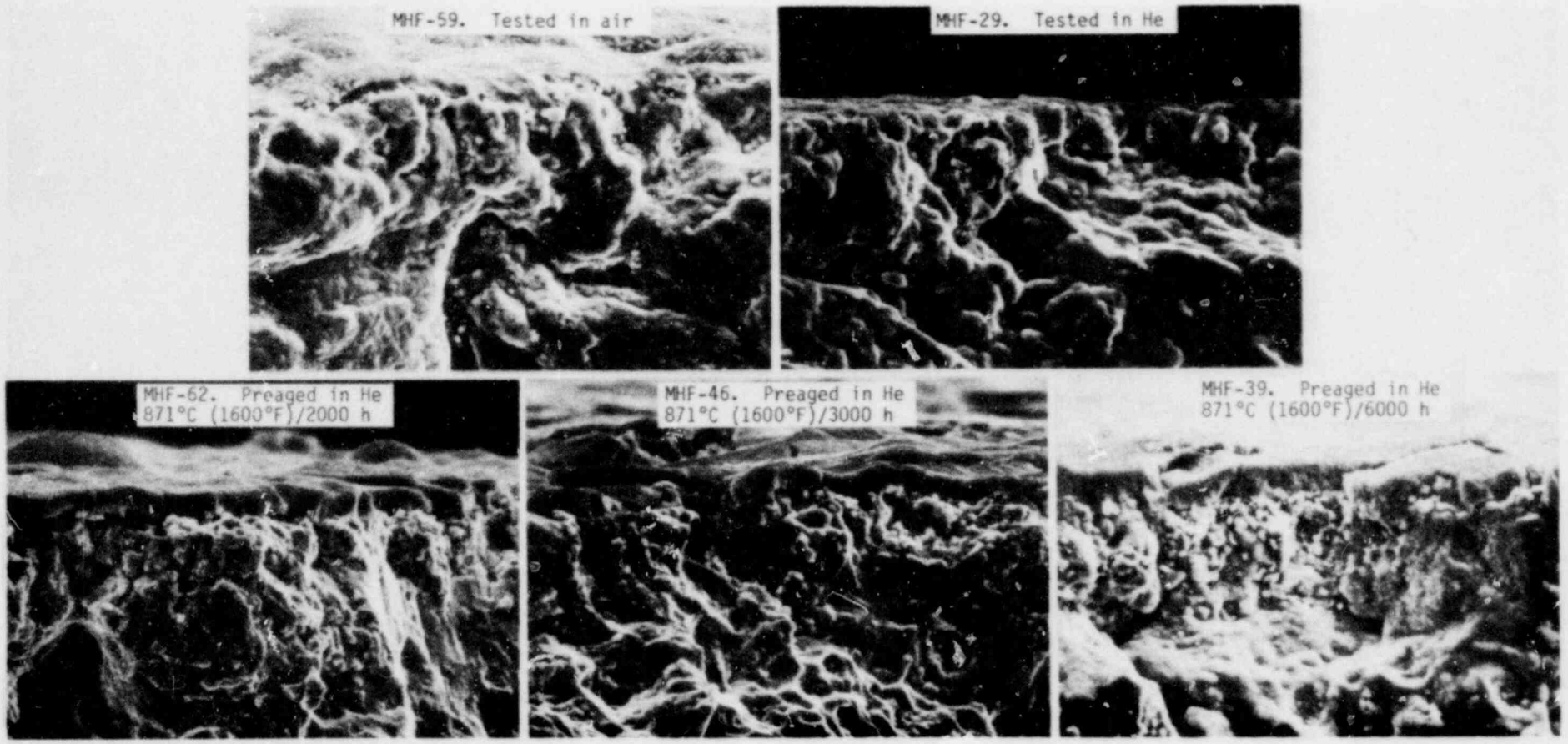

EDGES OF FRACTURE SURFACES FOR HASTELLOY X HIGH CYCLE FATIGUE SPECIMENS TESTED AT 871°C (1600°F) AS A FUNCTION OF TESTED ENVIRONMENT AND PRETEST THERMAL AGING TIME IN HTGR HELIUM. CRACK PROPAGATED FROM LEFT TO RIGHT. MAGNIFICATIONS 675X.

Figure 2.15

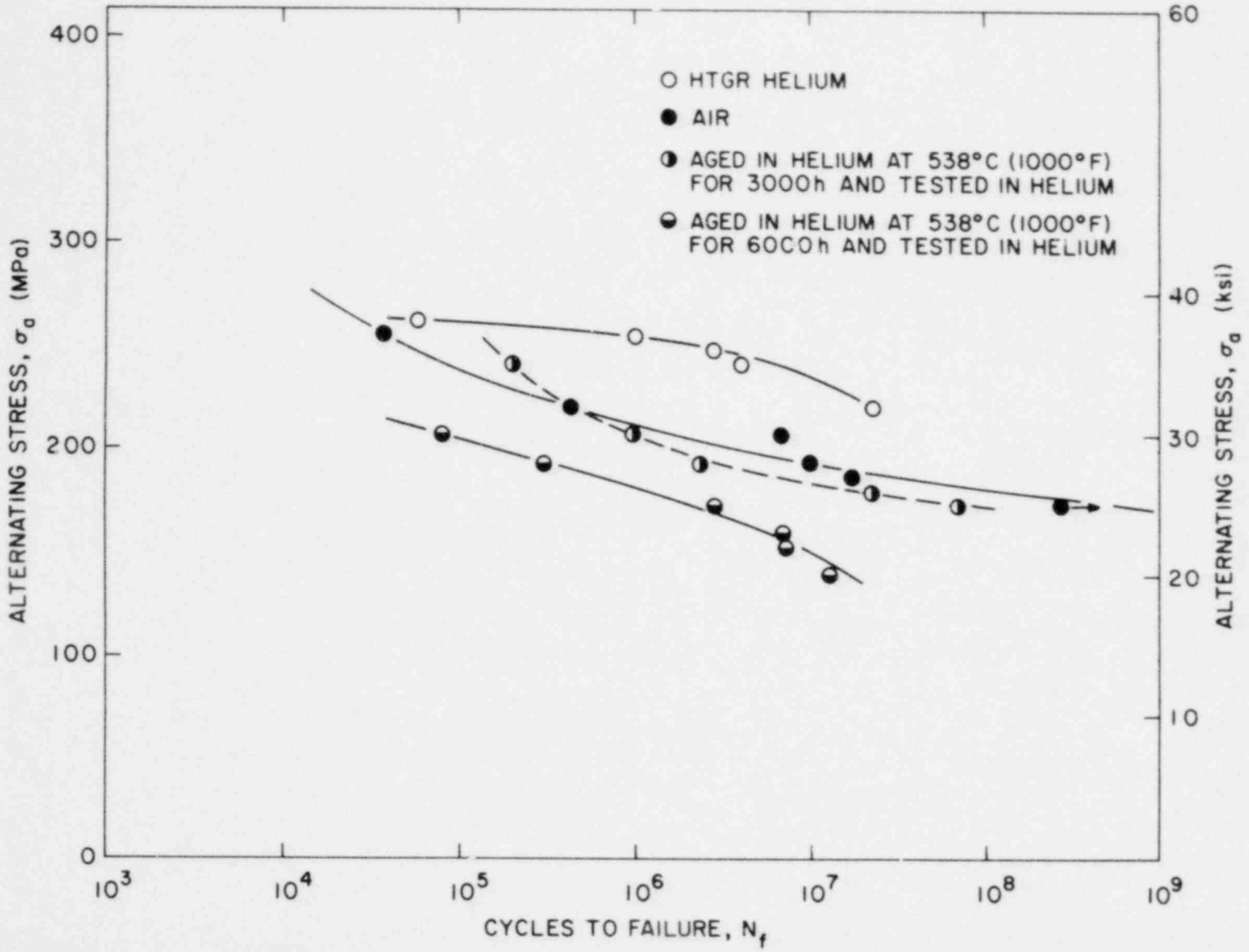

EFFECT OF A HELIUM ENVIRONMENT ON THE HIGH-CYCLE FATIGUE OF ANNEALED 2¼ Cr-1Mo STEEL AT 538°C (1000°F)

Figure 2.16

1/2 inch diameter rods.

Prior to machining of the test specimens the Incoloy 800H alloy was solution treated by heating to 1149°C (2100°F) and water quenched. The Hastelloy X specimens were heated to 1176°C (2150°F) for one-half hour and water quenched. In order to eliminate heat-to-heat variations the in-air and in-helium test specimens were made from single reference heats.

Our creep testing facility consists of 20 lever arm testing units; 15 of the units are equipped with environmental retorts for testing the helium environment and the balance of the units are used for in-air tests. The helium environment for the creep testing environment is being supplied from the Materials Test Loop (MTL). The composition of impurities in the helium was covered in Section 2.1. We are running a "wet" environment to simulate an operating HTGR which has water ingress into the primary system from leaking steam generator tubes, etc.

At the present, 7 of the units have tests that are in progress over 10,000 hours. The longest test under way is a Hastelloy X specimen testing in air at 760°C (1400°F) which has been in progress for 15,500 hours.

2.2.1 Incoloy 800H

Creep rupture testing of Incoloy 800H at 649°C (1200°F) and 760°C (1400°F) in the simulated HTGR helium environment supplied by the MTL and in air is continuing The stress rupture curves on specimens that have failed are shown in Figure 2.17. The minimum creep rate data are summarized in the curves shown in Figure 2.18. The stress-rupture data indicate that at 649°C (1200°F) the helium environment does not change the rupture life of Incoloy 800H when compared to in-air tests. However, testing in helium at 760°C (1400°F) seems to show a slightly lower rupture life but the effect is not conclusive. The creep rate data indicate that no differences exist between the in-air and in-helium test results at both 649°C (1200°F) and 760°C (1400°F).

2.2.2 Hastelloy X

Creep rupture testing of Hastelloy X is being carried out at 760°C (1400°F) and at 871°C (1600°F) in air and in the simulated helium environment. The stress rupture and minimum creep rate data obtained to date are summarized in Figure 2.19 and Figure 2.20, respectively.

The stress rupture curves show that when compared to testing in air, testing in the HTGR helium lowered the rupture life at both temperatures. However, the minimum creep rates are not affected by the environments studied at either of the testing temperatures.

The failed specimens are being examined metallographically and are also being studied by scanning electron microprobe to attempt to determine the cause of the lower rupture life of Hastelloy X in helium. Figure 2.21 shows the microstructure near the surface of the specimens and the oxide scale of two Hastelloy X specimens tested in helium, (a) at 760°C (1400°F) for 10,350 hours and (b) at 871°C (1600°F) for 5,109 hours. The specimen tested at 760°C (1400°F) (Figure 2.21a) shows a

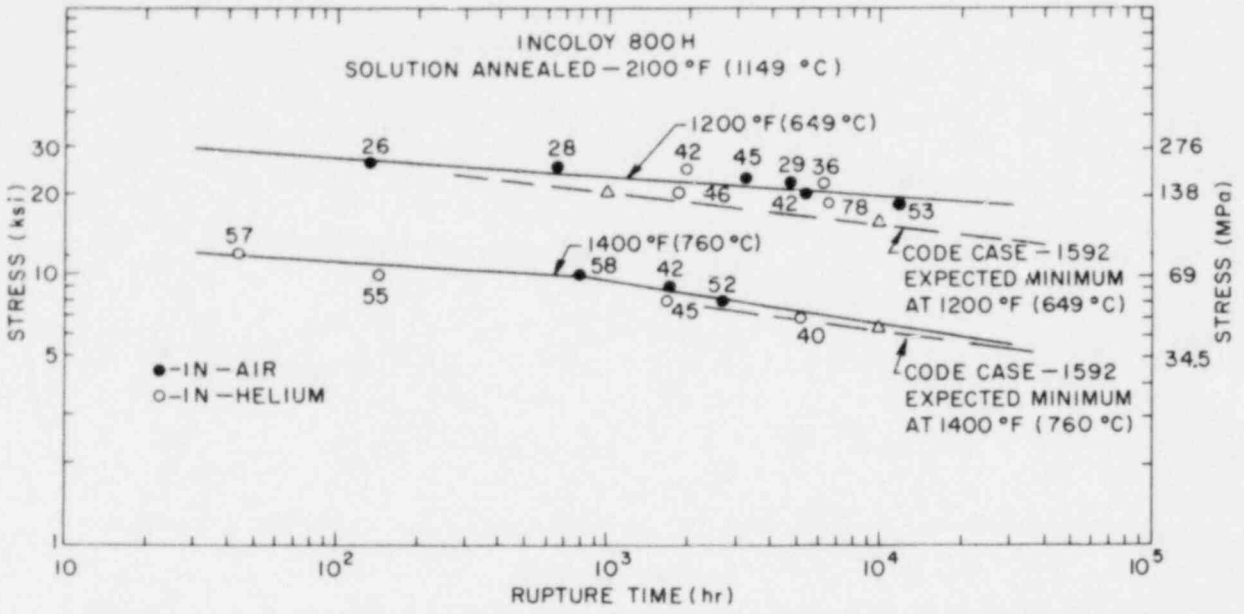

STRESS RUPTURE PROPERTIES INCOLOY 800H TESTED AT 1200 °F (649 °C) AND 1400 °F (760 °C) IN AIR AND IN HTGR HELIUM

Figure 2.17

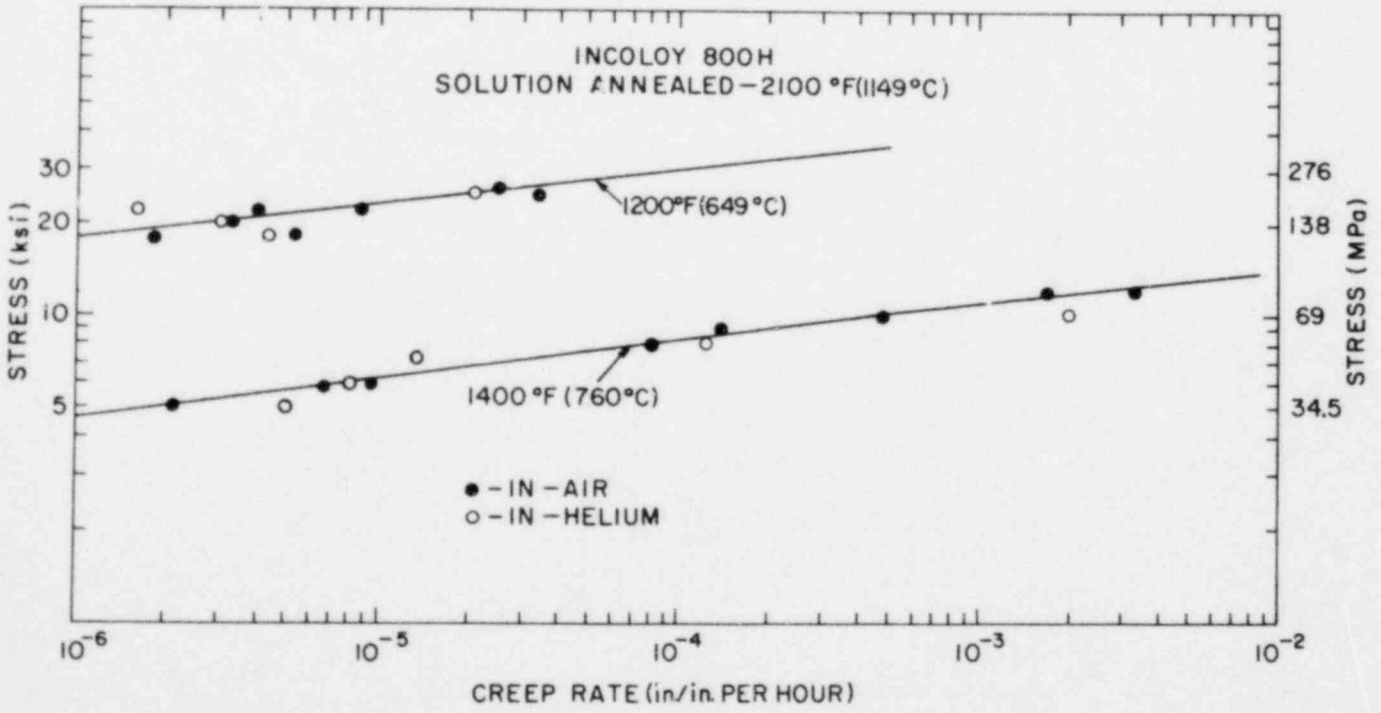

CREEP STRENGTHS OF INCOLOY 800H AT 1200 °F (649 °C) AND 1400 °F (760 °C) TESTED IN AIR AND IN HTGR HELIUM

Figure 2.18

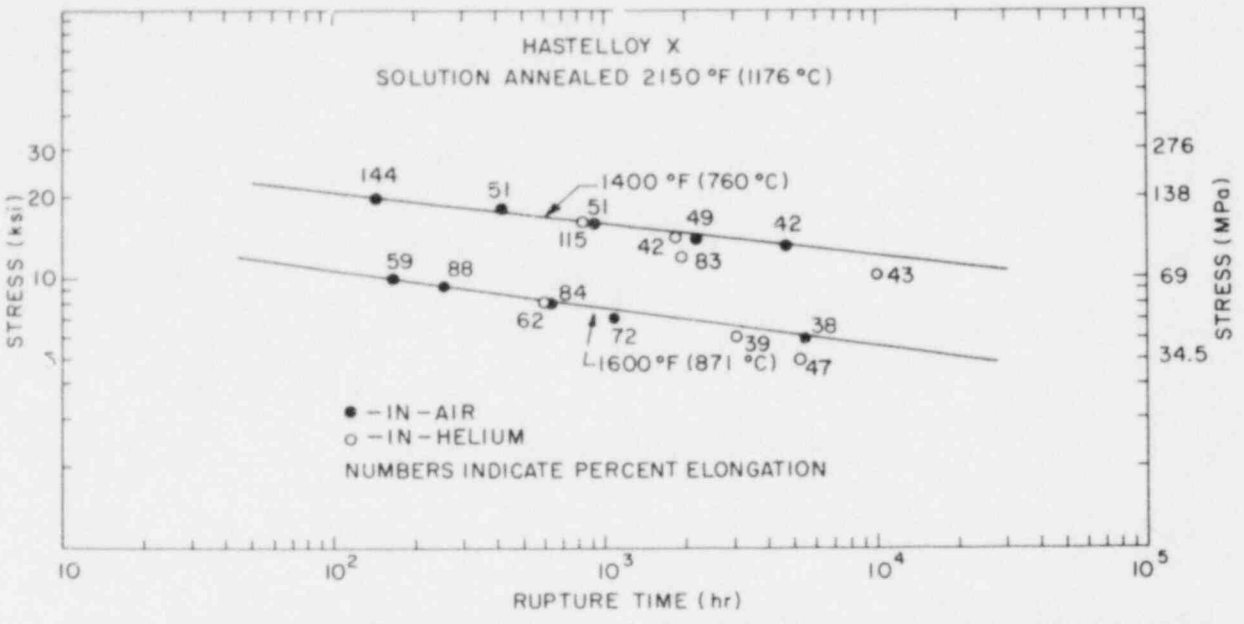

STRESS RUPTURE PROPERTIES OF HASTELLOY X AT 1400 °F (760 °C) AND 1600 °F (872 °C) TESTED IN AIR AND IN HTGR HELIUM

Figure 2.19

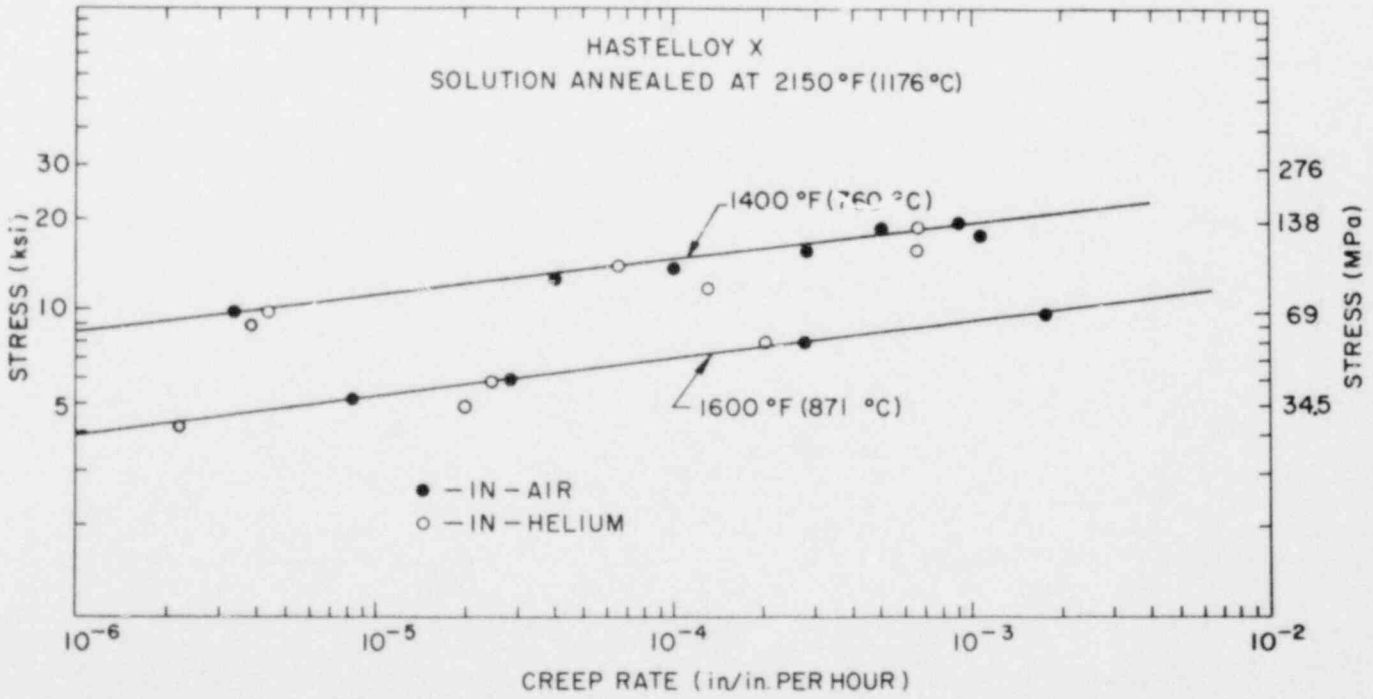

CREEP STRENGTHS OF HASTELLOY X AT 1400 °F (760 °C) AND 1600 °F (871 °C) IN AIR AND IN HTGR HELIUM

Figure 2.20

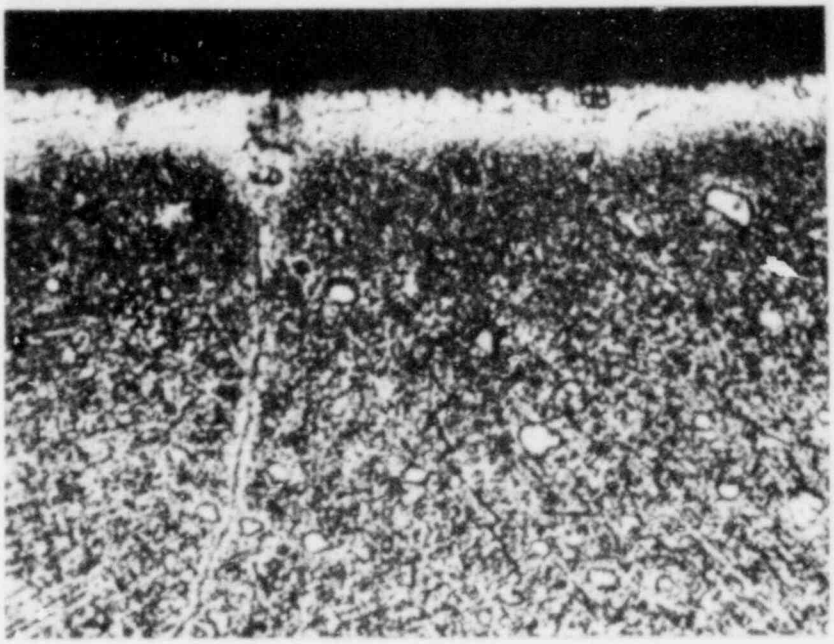

(a)

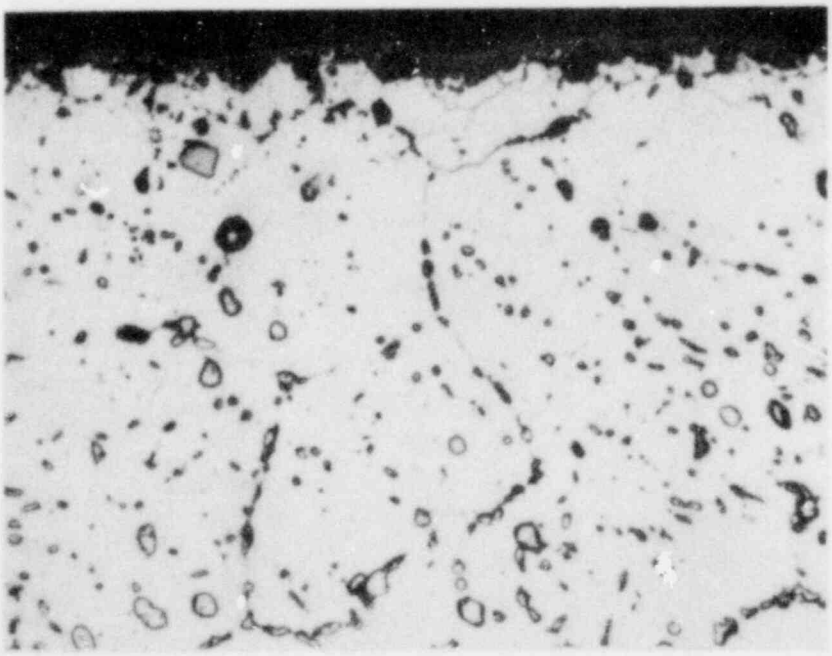

(b)

Figure 2.21. Microstructure of Hastelloy X creep rupture specimens tested in a helium environment at 760°C and at 871°C.
(a) Specimen MHT-12 tested at 760°C, 10,000 ksi, ruptured after 10,350 hours; (b) Specimen MHT-22 tested at 871°C, 5,000 ksi, failed after 5,109 hours. Both etched in oxalic acid. Magnifications 500X.

thin oxide scale, a light etching band underneath the scale, and a dark etching zone further into the specimen. Scanning electron microprobe studies show that the oxide layer is mostly chromium oxide with some manganese and the light etching band is an alloy depleted region. The dark etching zone is indicative of heavier precipitation and it could indicate a migration of carbon into this area. The specimen tested at 871°C (1600°F) (Figure 2.21b) shows a heavier oxide scale and also an alloy depleted zone underneath the scale layer. Further below the surface of the specimen, an area with intragranular precipitation is observed. These precipitates are believed to be carbides formed by migration of carbon into this area either from the environment or from the depleted alloy zone. Metallographic and scanning electron microprobe studies are continuing on fractured creep specimens.

2.3 Effect of Fission Product Interactions on the Mechanical Properties of HTGR Metals (P. Soo, J. G. Y. Chow, S. Aronson, R. Sabatini)

This program was initiated to determine the effect of long term (>1000 hours) exposure of HTGR alloys (Type 304 stainless steel, Hastelloy X, Incoloy 800, and 2 1/4Cr-1Mo steel) to fission product species such as iodine, tellurium, and cesium iodide, under conditions approaching as practically as possible those for normal HTGR operation. Exposures and analyses have been completed on five groups of samples as given in Table 2.1. Much of the data were reported in the previous quarterly report (Soo, 1979b).

Table 2.1

Exposure of HTGR Alloys to Simulated Fission Products

Test No.	Simulated Fission Product	Fission Product Vapor Pressure (atm)	Temperature of Metal Samples (°C)	Exposure Time (hours)
1	CsI	10^{-5}	790	1896
2	Te_2	10^{-5}	770	1992
3	CsI	10^{-5}	730	1825(1)
4	Te_2	10^{-5}	800	1850(1)
5	I_2	10^{-3}	800	1173

(1) This capsule contains a Ni-NiO mixture maintained at 800°C to give an oxygen partial pressure of 10^{-14} atm.

Previous studies reported in earlier quarterly reports show that Type 304 stainless steel is not embrittled in the three environments. Incoloy 800 showed moderate cracking in Te_2 and CsI during a post exposure bend test. However, Hastelloy X was extremely embrittled. In order to separate the contributions of the simulated fission product attack and thermal aging on the degree of embrittlement, two sets of thermal control specimens were aged for 2060 hours at 800°C in evacuated quartz capsules. One capsule contained a Ni/NiO buffer mixture, which at 800°C maintained an oxygen partial pressure of 10^{-14} atm. This, therefore, allows the effect of oxidation on embrittlement to be determined. Figures 2.22 through 2.25 show, in fact, that the presence of 10^{-1} atm. of oxygen does not

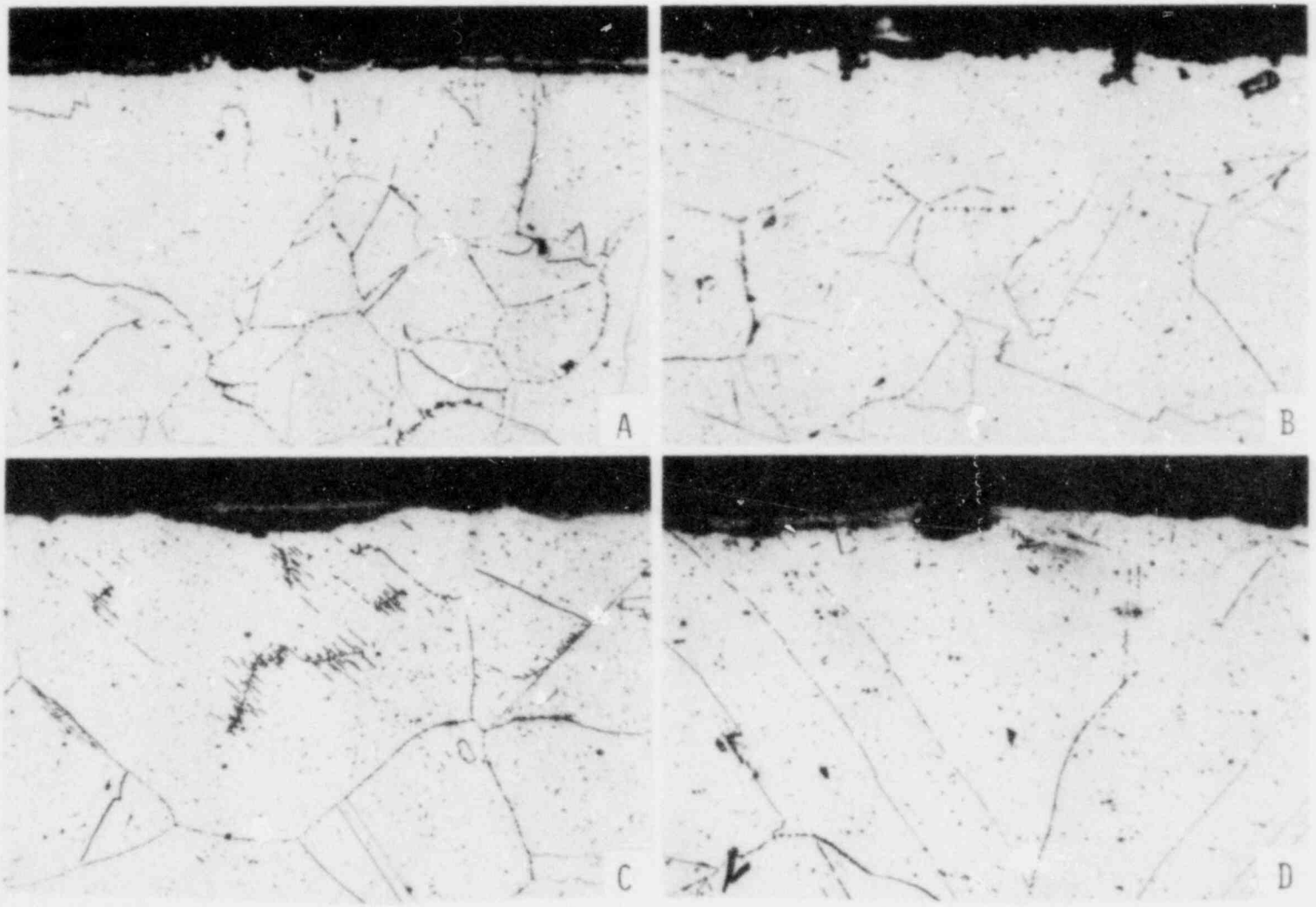

APPEARANCE OF TYPE 304 STAINLESS STEEL CONTROL SPECIMENS: (A) VACUUM ENCAPSULATED, 800°C/2060 H, UNSTRESSED. (B) VACUUM ENCAPSULATED, 800°C/2060 H, BEND SPECIMEN. (C) 10^{-14} ATM. O_2, 800°C/2060 H, UNSTRESSED. (D) 10^{-14} ATM. O_2, 800°C/2060 H, BEND SPECIMEN. ALL MAGNIFICATIONS 350X.

Figure 2.22

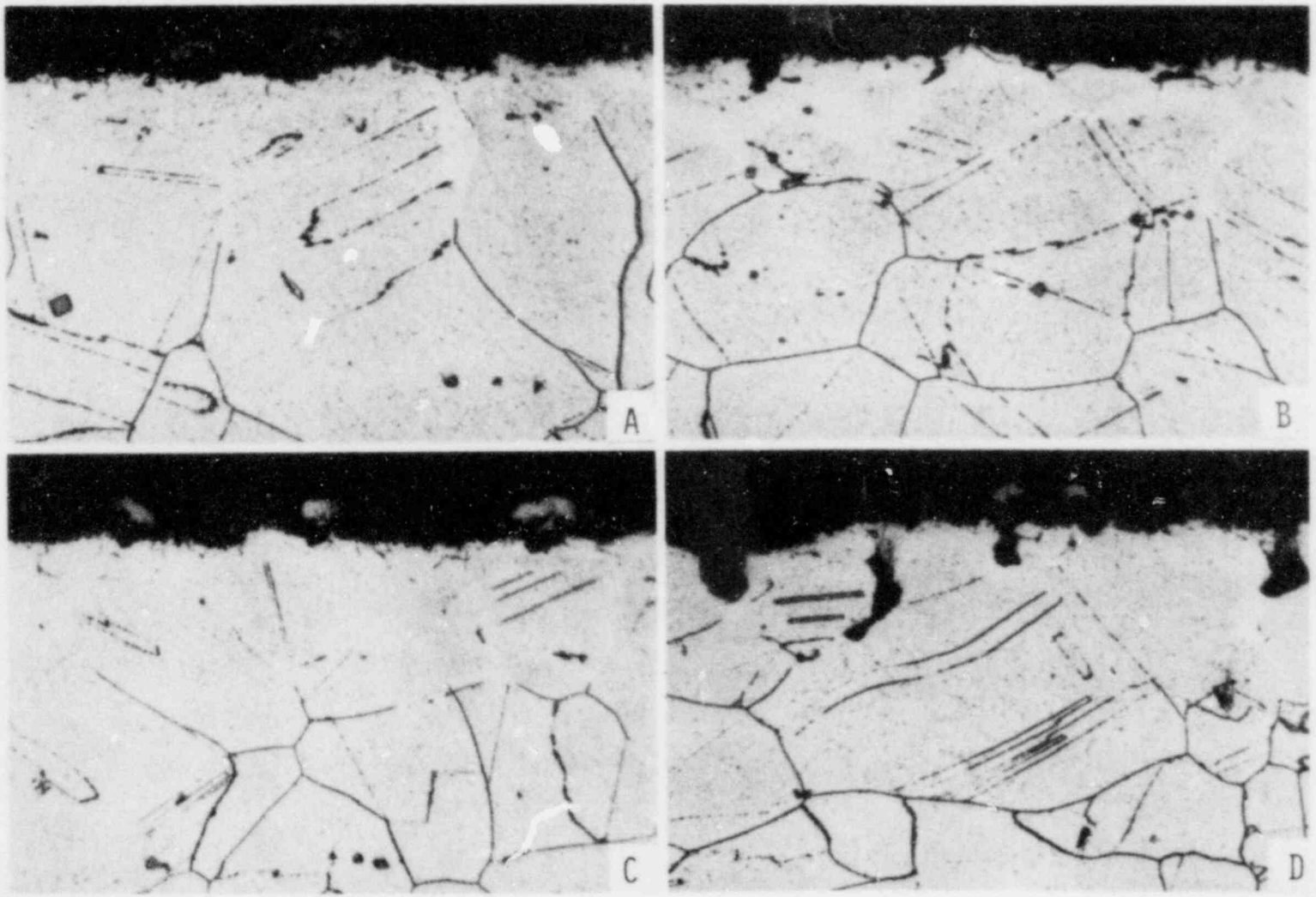

APPEARANCE OF INCOLOY 800 CONTROL SPECIMENS: (A) VACUUM ENCAPSULATED, 800°C/2060 H, UNSTRESSED. (B) VACUUM ENCAPSULATED, 800°C/2060 H, BEND SPECIMEN. (C) 10^{-14} ATM. O_2, 800°C/2060 H, UNSTRESSED. (D) 10^{-14} ATM. O_2, 800°C/2060 H, BEND SPECIMEN. ALL MAGNIFICATIONS 350X.

Figure 2.23

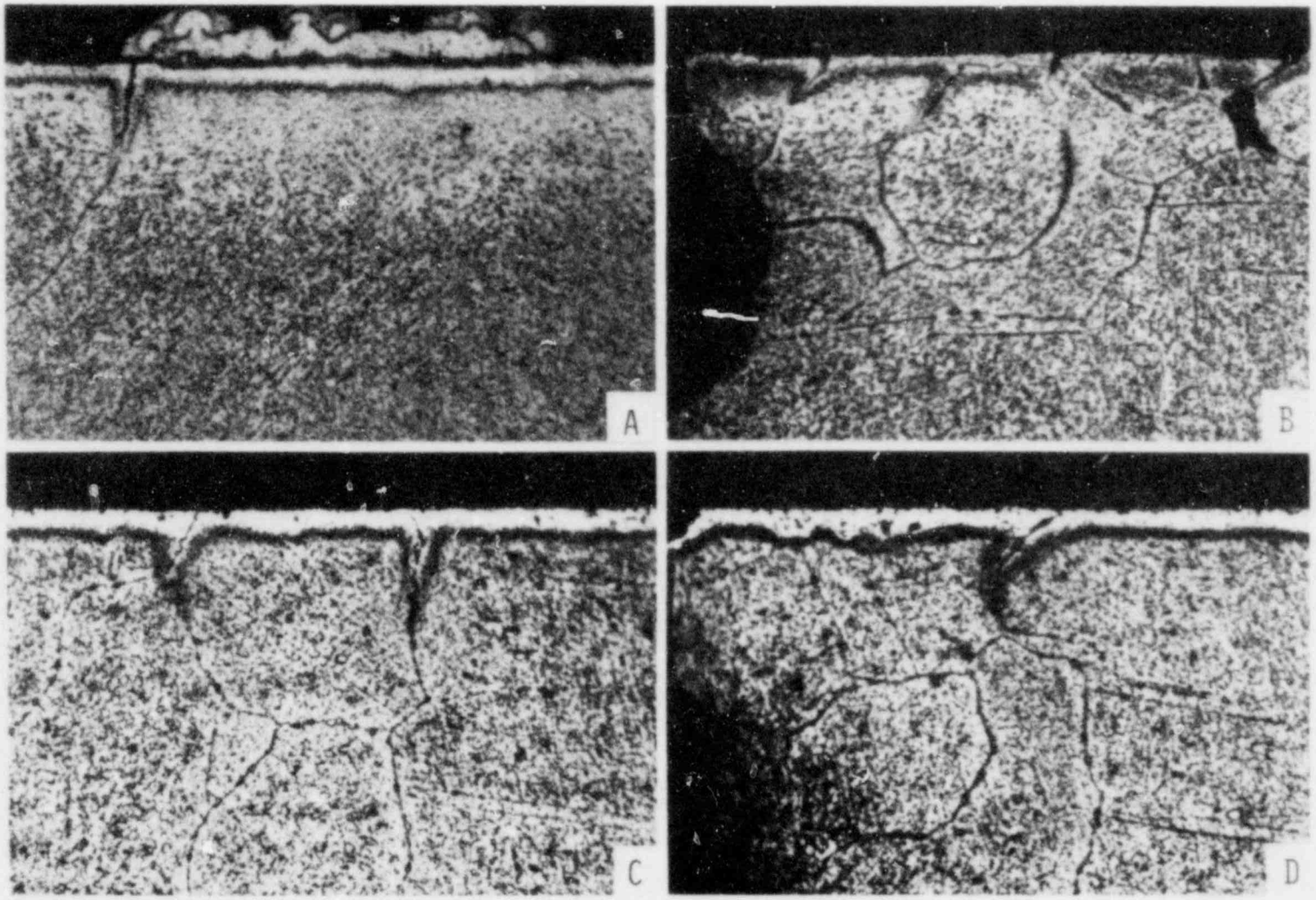

APPEARANCE OF HASTELLOY X CONTROL SPECIMENS: (A) VACUUM ENCAPSULATED, 800°C/2060 H, UNSTRESSED. (B) VACUUM ENCAPSULATED, 800°C/2060 H, BEND SPECIMEN. (C) 10^{-14} ATM. O_2, 800°C/2060 H, UNSTRESSED. (D) 10^{-14} ATM. O_2, 800°C/2060 H, BEND SPECIMEN. ALL MAGNIFICATIONS 350X.

Figure 2.24

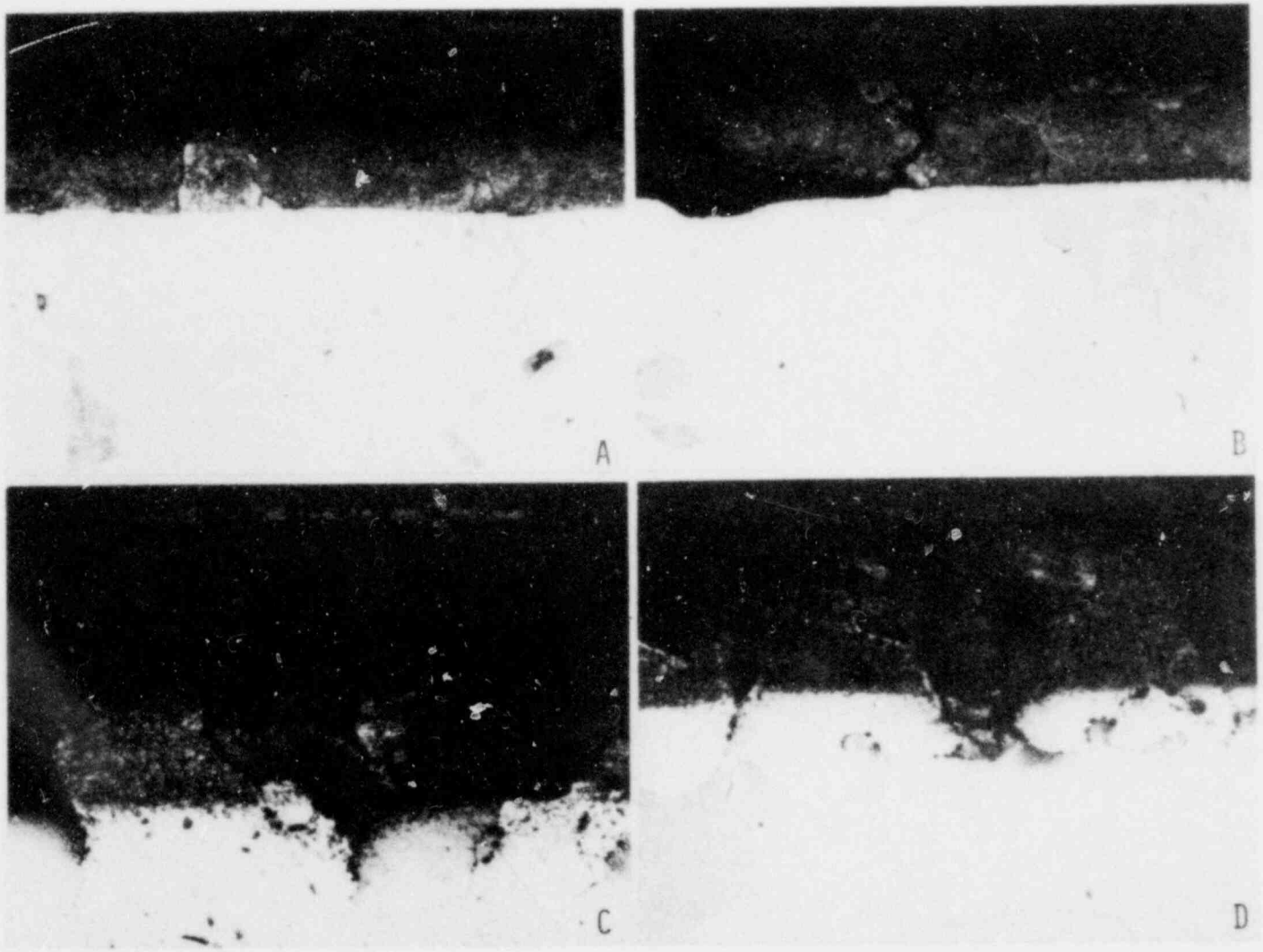

APPEARANCE OF 2 1/4CR-1MO CONTROL SPECIMENS: (A) VACUUM ENCAPSULATED, 800°C/2060 H, UNSTRESSED. (B) VACUUM ENCAPSULATED, 800°C/2060 H, BEND SPECIMEN. (C) 10^{-14} ATM. O_2, 800°C/2060 H, UNSTRESSED. (D) 10^{-14} ATM. O_2, 800°C/2060 H, BEND SPECIMEN. ALL MAGNIFICATIONS 350X.

Figure 2.25

generally increase the number of surface cracks in specimens which were bent in a special jig (at room temperature) through an angle of 80°.

In the Type 304 stainless steel and Incoloy 800 the grain boundaries close to the specimen surface were not etchable by oxalic acid. Most likely, chromium carbides do not form in these regions due to the loss of chromium during oxide scale formation. This would lead to the formation of "clean" grain boundaries which are difficult to etch.

Hastelloy X was greatly embrittled by the thermal aging and, upon bending, complete fracture occurred. In the case of quenched and tempered 2 1/4Cr-1Mo steel, which is austenitic at the aging temperature of 800°C, there is a wide oxidized layer shown as a dark region in Figure 2.25. This area is substantially embrittled and intergranular cracking is noticed in the bend specimens.

A comparison of the thermal control bend specimens (Figures 2.22 through 2.25) with those exposed to CsI and Te_2 (Figures 2.26 through 2.29) shows that the extent of cracking is comparable. This is a clear indication that for the conditions listed in Table 2.1 CsI and Te_2 do not significantly embrittle the alloys evaluated. Any intergranular cracks formed are a direct result of metallurgical changes in the materials, brought about by long term thermal exposure.

In order to more fully understand the nature of oxidation on the thermal control specimen surfaces, a series of scanning electron microscope/microprobe (SEMM) elemental scans was made using X-ray energy dispersive system (EDS) analyses. Figures 2.30 through 2.32 show data obtained. For the capsule containing 10^{-14} atm. of oxygen, a relatively uniform scale is formed on the surface. However, in the case of the capsule which did not contain this buffered oxygen concentration three distinct features were formed:

1. Small faceted crystallites.
2. Larger "rumpled" areas upon which the crystallites were formed.
3. Extensive uniform regions of scale which covered most of the specimen surfaces.

The SEMM data show that the surfaces of the austenitic materials exposed to the 10^{-14} atm. of oxygen are rich in Cr and Fe. At this oxygen partial pressure, for which Fe and Cr oxides are stable, it is very likely that the Fe and Cr detected are in the form of a mixture of Fe and Cr oxides. This has been confirmed previously in earlier work in this program (Soo, 1979b).

The formation of three distinct surface products in the capsule not containing the Ni/NiO buffer mixture is more complex. The SEMM data show that the crystallites predominently contain Fe; the small rumpled areas contain Fe with a smaller amount of Cr; and the very large surface scale areas contain Cr with smaller amounts of Fe. In interpreting these data, results obtained previously for Hastelloy X exposed to Te_2 provide a valuable insight (Figure 2.34). In this figure in which SEMM line scans were taken with an X-ray wavelength dispersive system (WDS) the location of oxygen can be found. It is seen that the uppermost light layer (corresponding to the rumpled regions in Figures 2.30 through 2.32) is composed of Fe with a small amount of oxygen. The underlying gray layer

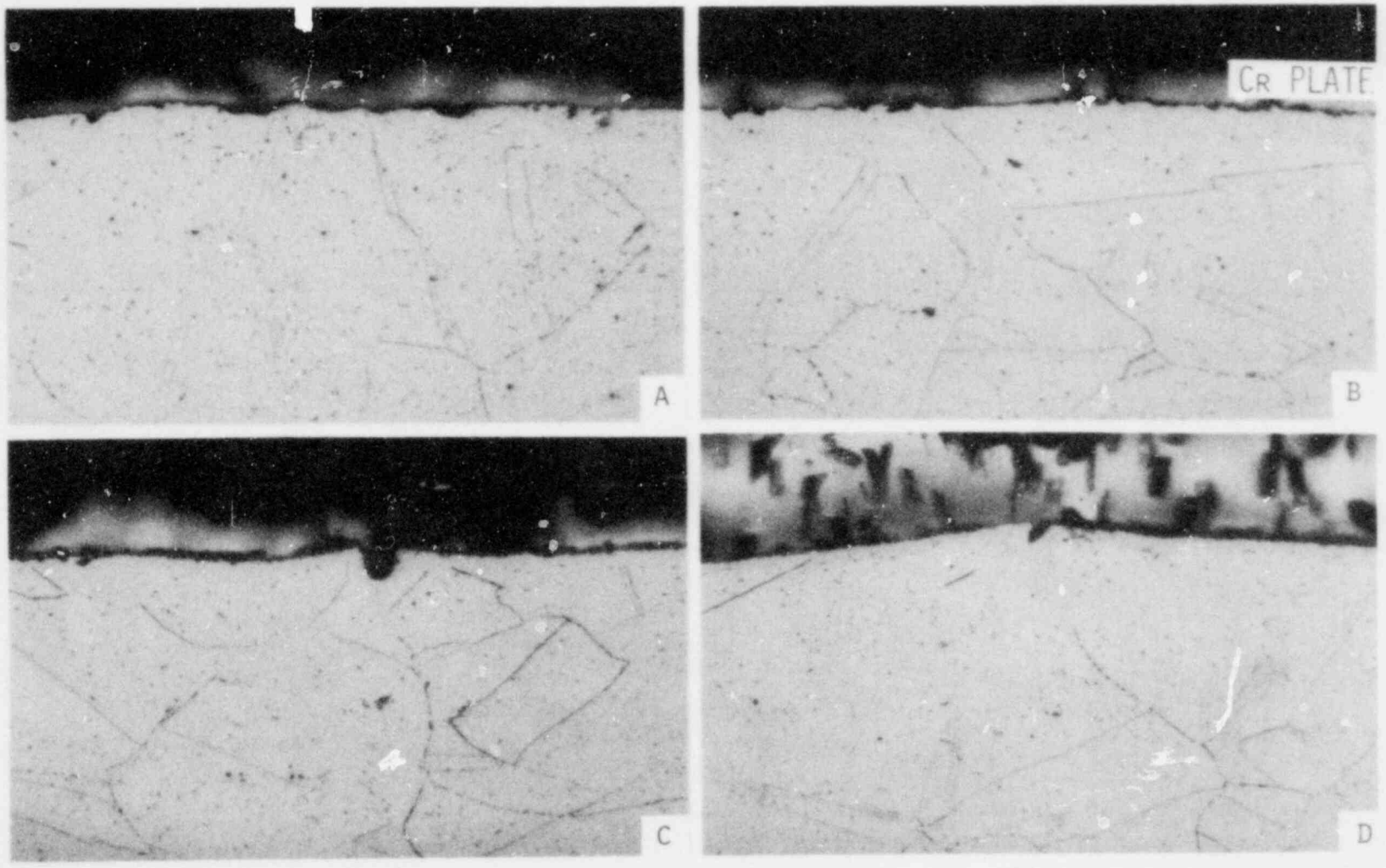

EFFECT OF BENDING ON TYPE 304 STAINLESS STEEL EXPOSED TO SIMULATED FISSION PRODUCT SPECIES:
(A) 770°C/1992 H, 10^{-5} ATM. TE_2, (B) 800°C/1850 H, 10^{-5} ATM. TE_2 + 10^{-14} ATM. O_2,
(C) 790°C/1896 H, 10^{-5} ATM. CsI, (D) 730°C/1825 H, 10^{-5} ATM. CsI + 10^{-14} ATM. O_2.
MAGNIFICATION 350X.

Figure 2.26

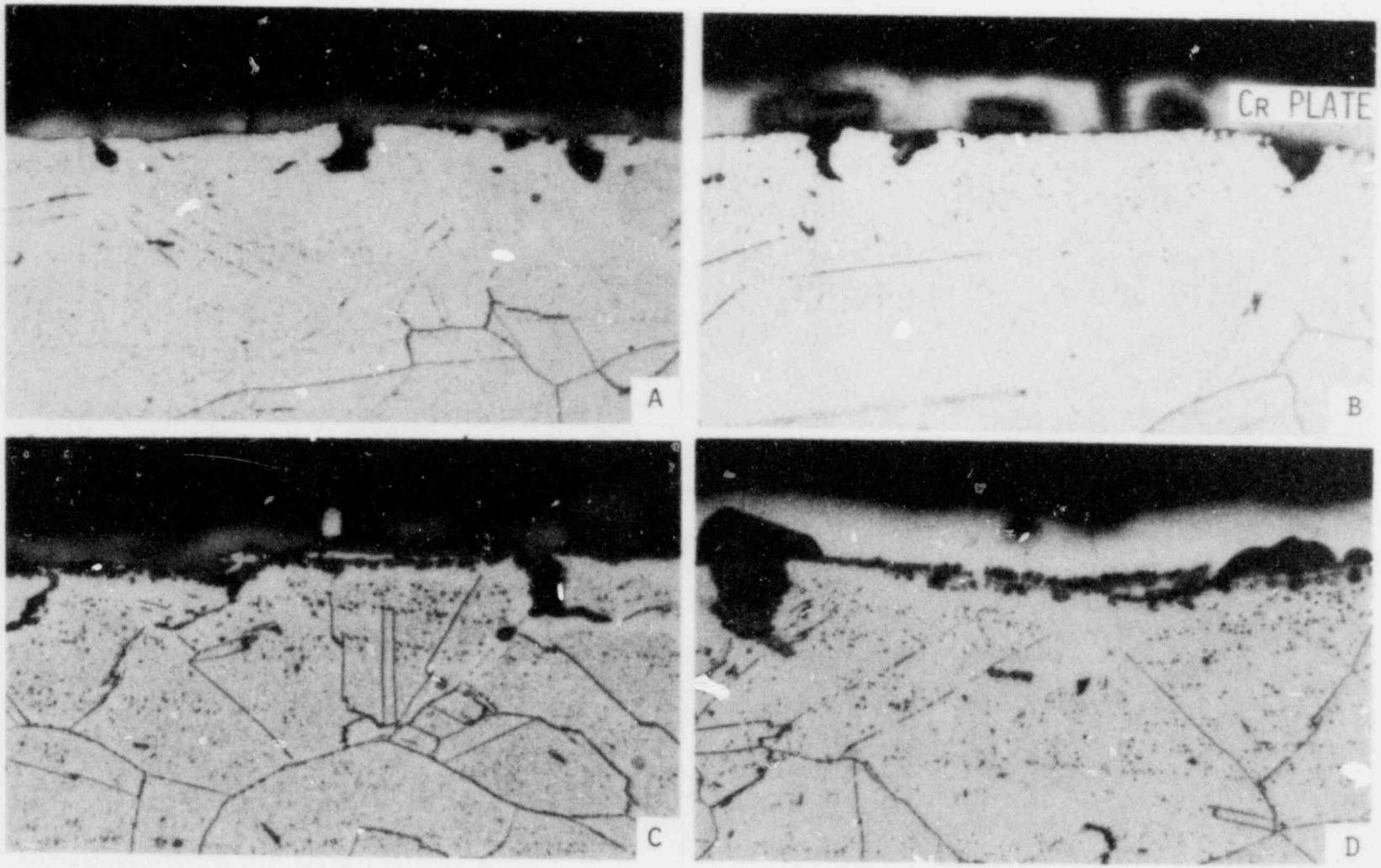

EFFECT OF BENDING ON INCOLOY 800 EXPOSED TO SIMULATED FISSION PRODUCT SPECIES: (A) 770°C/1992 H, 10^{-5} ATM. Te_2, (B) 800°C/1850 H, 10^{-5} ATM. Te_2 + 10^{-14} ATM. O_2, (C) 790°C/1896 H, 10^{-5} ATM. CsI, (D) 730°C/1825 H, 10^{-5} ATM. CsI + 10^{-14} ATM. O_2. MAGNIFICATION 350X.

Figure 2.27

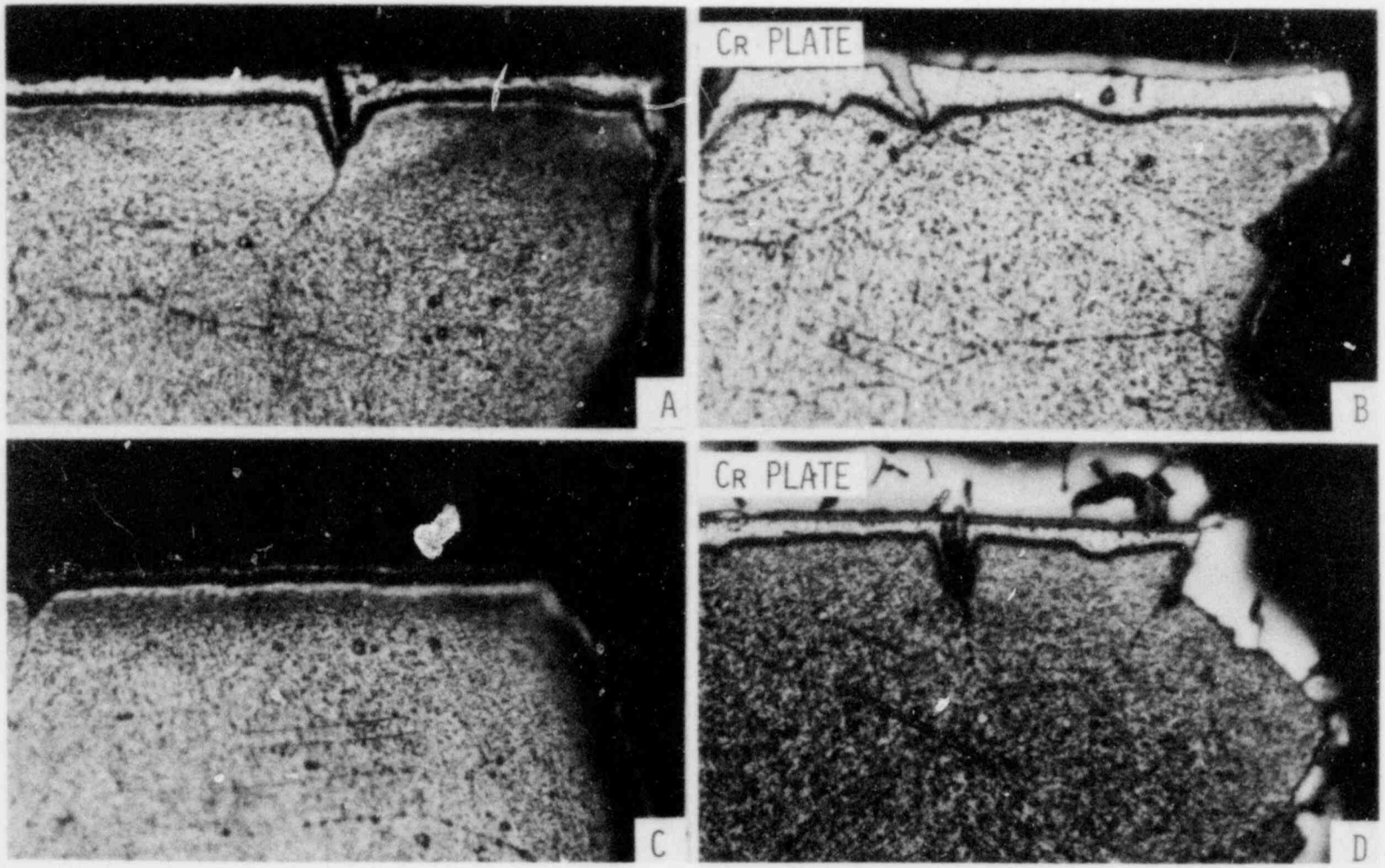

Effect of bending on Hastelloy X exposed to simulated fission product species: (A) 770°C/1992 h, 10^{-5} atm. Te_2, (B) 800°C/1850 h, 10^{-5} atm. Te_2 + 10^{-14} atm. O_2, (C) 790°C/1896 h, 10^{-5} atm. CsI, (D) 730°C/1825 h, 10^{-5} atm. CsI + 10^{-14} atm. O_2. Magnification 350X.

Figure 2.28

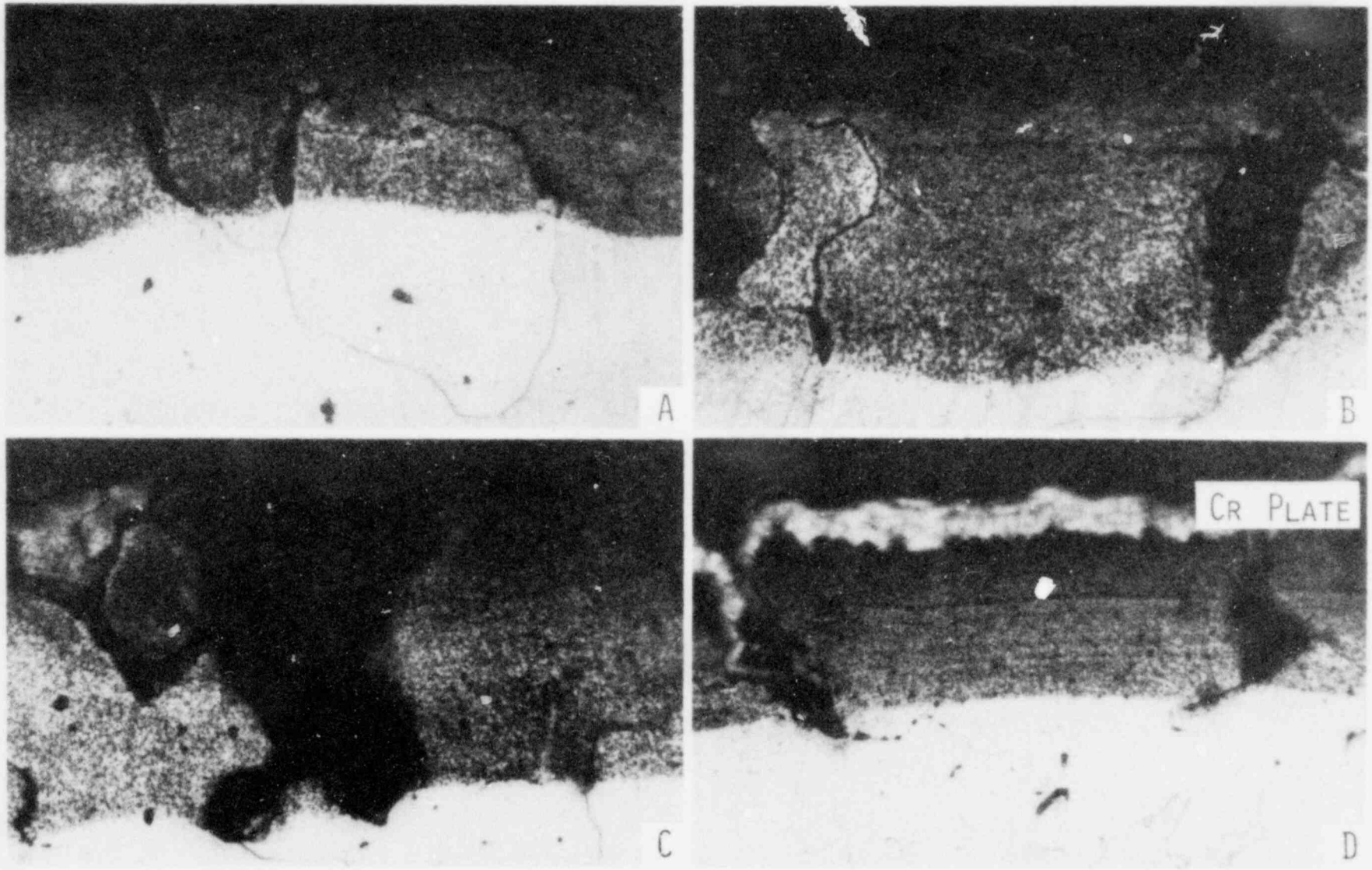

Effect of bending on Q&T 2 1/4Cr-1 Mo exposed to simulated fission product species: (A) 770°C/1992 h, 10^{-5} atm. Te_2, (B) 800°C/1850 h, 10^{-5} atm. Te_2 + 10^{-14} atm. O_2, (C) 790°C/1896 h, 10^{-5} atm. CsI, (D) 730°C/1825 h, 10^{-5} atm. CsI + 10^{-14} atm. O_2. Magnification 350X.

Figure 2.29

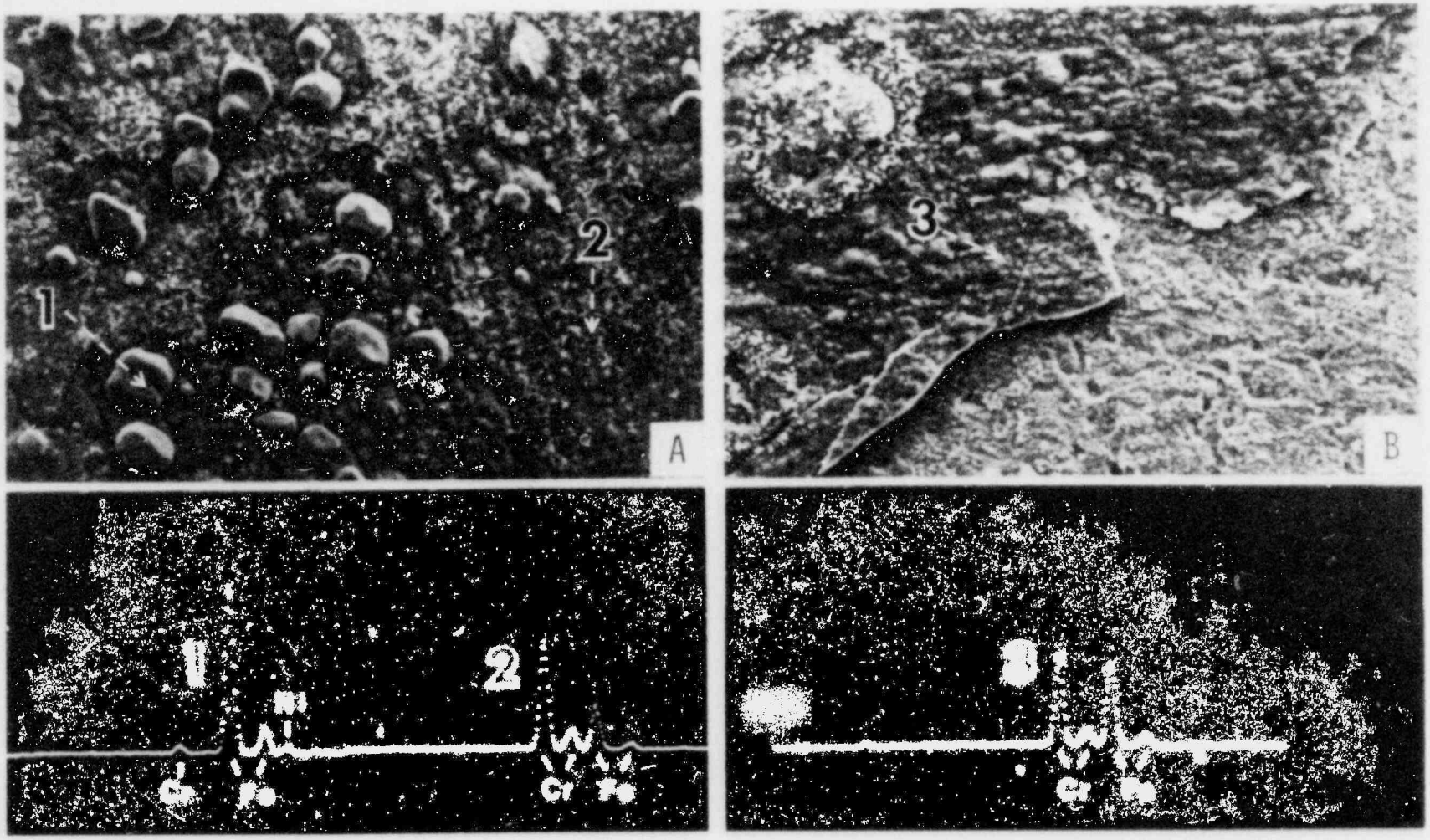

SEMM SCANS OF UNSTRESSED TYPE 304 STAINLESS STEEL CONTROL SPECIMENS: (A) VACUUM ENCAPSULATED, 800°C/2060 H. (B) 10^{-14} ATM. O_2, 800°C/2060 H. MAGNIFICATIONS 330X.

Figure 2.30

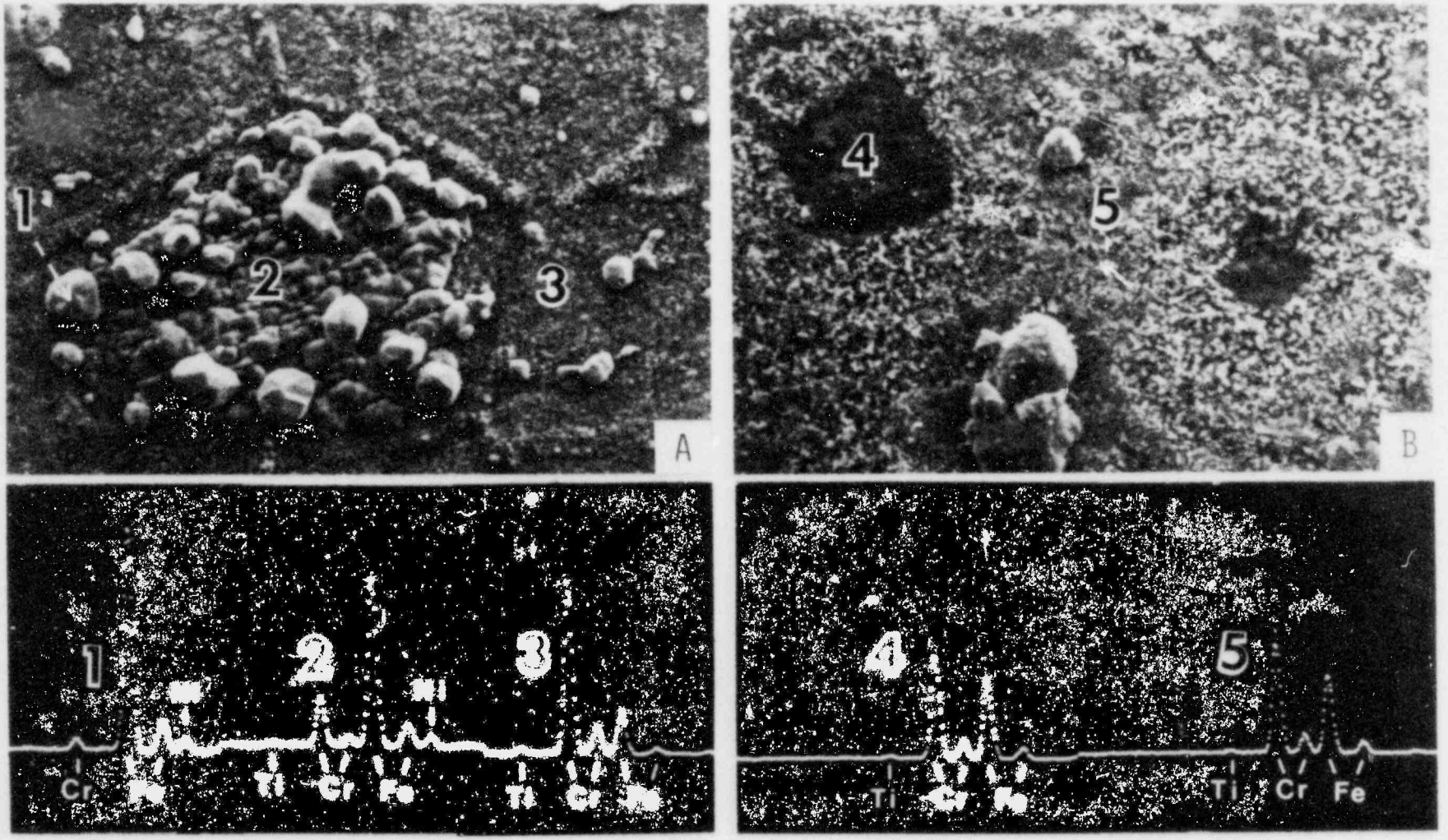

SEMM SCANS OF UNSTRESSED INCOLOY 800 CONTROL SPECIMENS: (A) VACUUM ENCAPSULATED, 800°C/2060 H. (B) 10^{-14} ATM. O_2, 800°C/2060 H. MAGNIFICATIONS 330X.

Figure 2.31

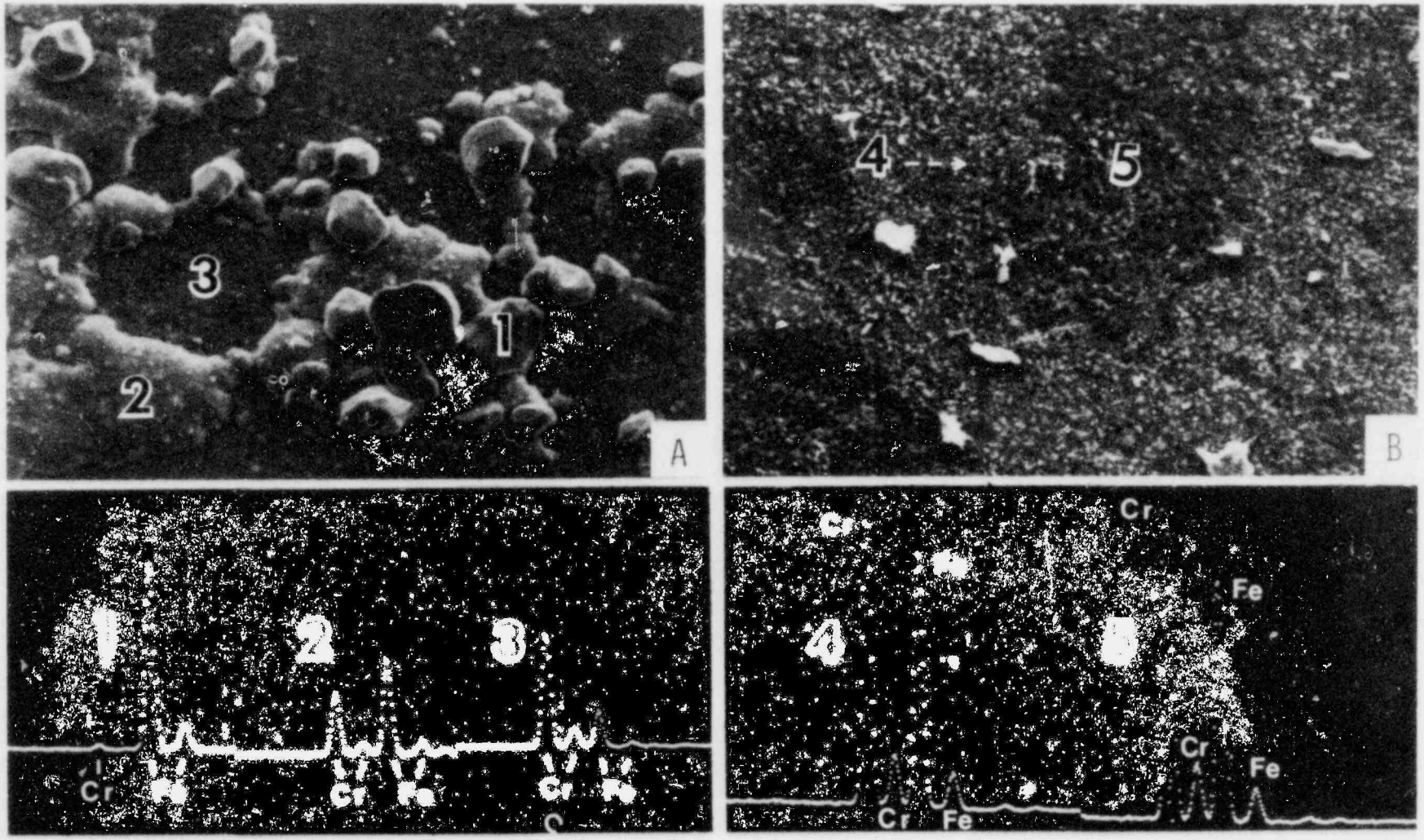

SEMM SCANS OF UNSTRESSED HASTELLOY X CONTROL SPECIMENS: (A) VACUUM ENCAPSULATED, 800°C/2060 H. (E) 10^{-14} ATM. O_2, 800°C/2060 H. MAGNIFICATIONS 330X.

Figure 2.32

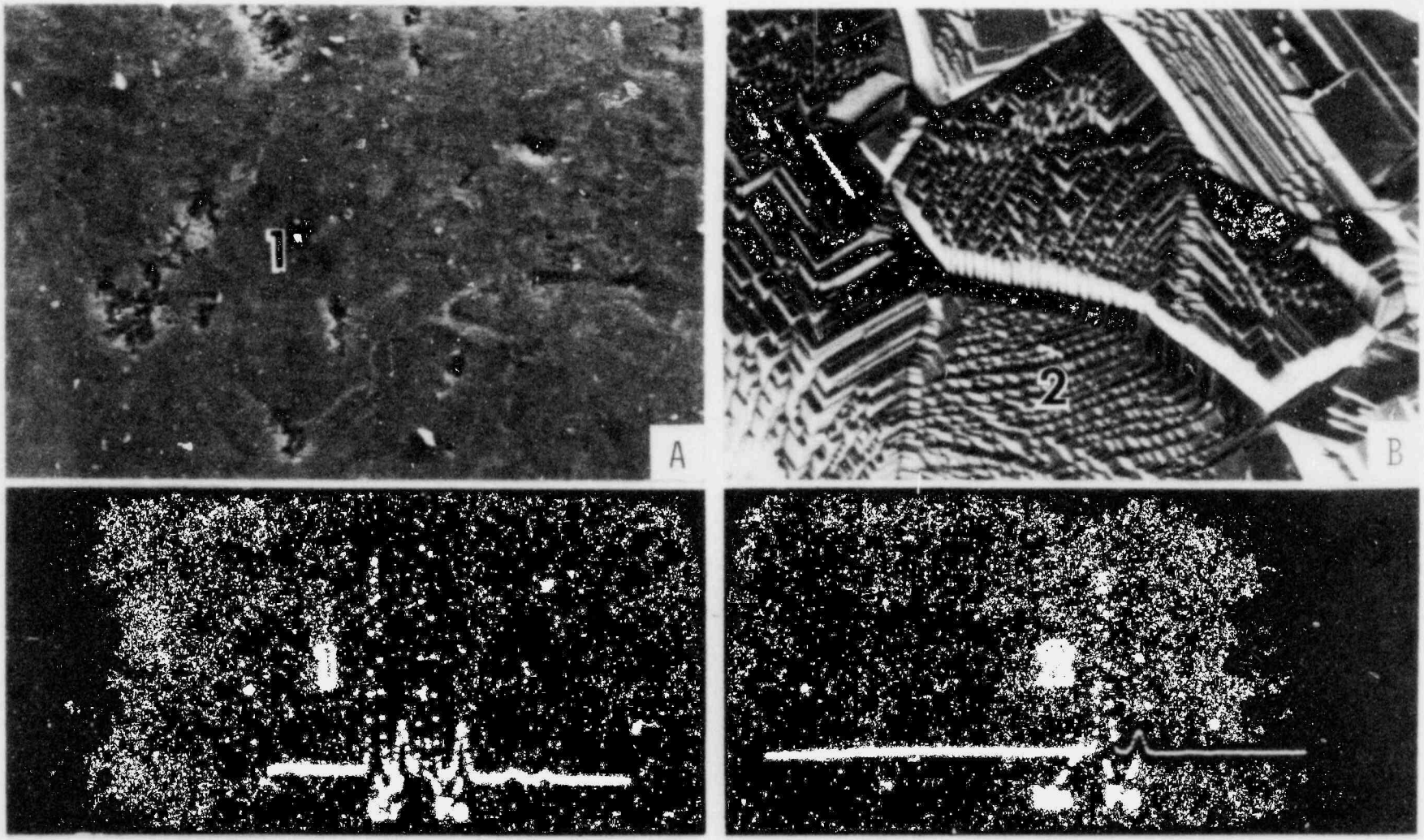

SEMM SCANS OF UNSTRESSED 2 1/4CR-1MO CONTROL SPECIMENS: (A) VACUUM ENCAPSULATED, 800°C/2060 H. (B) 10^{-14} ATM. O_2, 800°C/2060 H. MAGNIFICATIONS 330X.

Figure 2.33

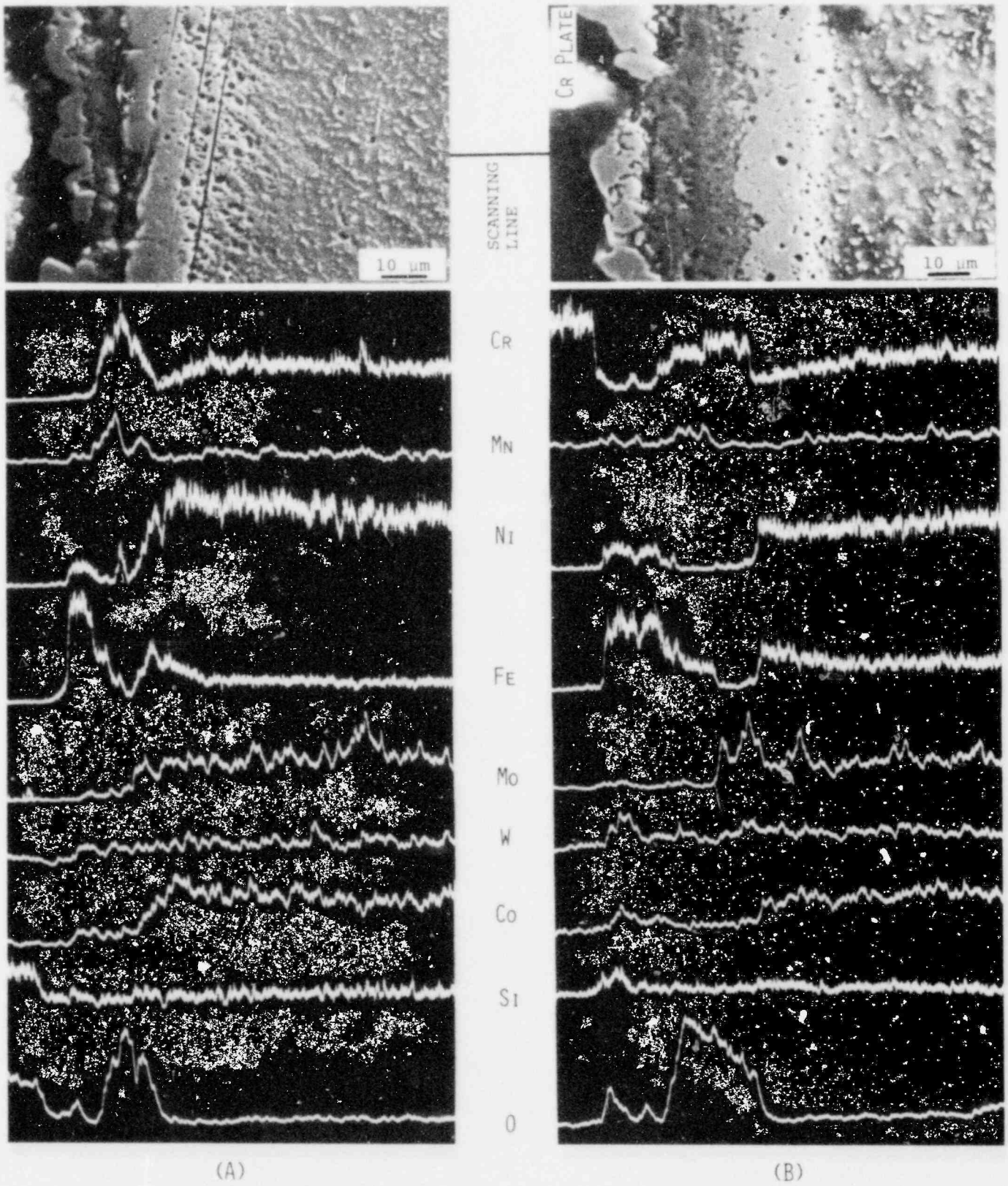

SCANNING ELECTRON MICROSCOPE/MICROPROBE LINE SCANS THROUGH THE SURFACE OF HASTELLOY X EXPOSED TO SIMULATED FISSION PRODUCT SPECIES: (A) 770°C/1992 H, 10^{-5} ATM. Te_2, (B) 800°C/1850 H, 10^{-5} ATM. Te_2 + 10^{-14} ATM. O_2.

Figure 2.34

is a Cr/Mn oxide. From this information, a tentative scenario for the formation of the three component surface layer on specimens heated in the evacuated quartz capsules can be made. Apparently, degassing of the quartz tube occurs when it is initially inserted into the furnace at 800°C. Oxides of Cr, Fe and possibly Ni are quickly formed. Degassing would soon be complete and the oxygen partial pressure would decrease to a very low value such that the Fe and Ni oxides would become unstable in the presence of excess Cr, and the Fe and Ni oxides would be reduced to metallic Fe and Ni. Oxygen released would form additional Cr_2O_3.

The rumpled areas probably represent a mixture of Fe, Fe_xO_y, and Cr_2O_3. The small crystallites are likely to be "pure" Fe formed by a more complete reduction of Fe_xO_y. Some type of nucleation and growth process appears to be occurring in this case based on the shape and distribution of the crystallites.

The results for the 2 1/4Cr-1Mo steel seem to be more straightforward (Figure 2.33). At an oxygen pressure of 10^{-14} atm., Fe_xO_y is stable and the Fe detected by the SEMM is likely to be in the form of this oxide. On the other hand, in the capsule without the Ni/NiO buffer mixture, the rate of oxidation is slower. Therefore, during the initial heating period, when degassing of the quartz capsule occurs, Fe_xO_y would be formed. The small amount of Cr in the steel is small (2 1/4%) and quite likely only small amounts of Cr_2O_3 are initially produced. However, as time progresses, Cr will be able to diffuse to the surface so that increasing amounts of Cr_2O_3 are formed and some of the Fe_xO_y is probably reduced to metallic Fe. The large Fe and Cr peaks in Figure 2.33 are likely to represent the presence of Cr_2O_3, Fe_xO_y and Fe.

2.4 Helium Impurities Loop (D. G. Schweitzer, G. Uneberg)

As noted previously, the problem of estimating possible property changes in HTGR materials that may occur over a 40-year lifetime includes determination of

a) the activities of C, Cr, Mn, FeO, etc. in as-received or preconditioned metals,
b) the direction of the change in steel composition required by equilibrium assumptions for expected gas compositions and temperatures,
c) the kinetics of time rate of change of activities for a range of operating conditions and
d) the property changes associated with the resulting activity changes.

During the past year we have been using data from the Helium Impurities Loop (HIL) to develop a model which can be used to achieve the above objectives. The data here are believed to represent surface reactions and therefore surface activities. In general the CO and CO_2 equilibrium concentrtions are approximated after 100-200 hours of reaction time. It is not expected that bulk chromium or bulk managnese can diffuse sufficiently rapidly in these times at this temperature to attain equilibrium within the steels. Until such information is obtained, the results obtained from the techniques described here are believed to represent rapid surface changes that may not be in equilibrium with the bulk steel.

2.4.1 Determination of Carbon Activity, Chromium Activity, Iron Oxide Activity and Oxygen Potential

At present, we have determined the carbon activity changes in the steels in the hot leg (730°C) of the HIL by two independent techniques. The first involves adding H_2 to the loop and determining the time stable value of the methane that builds up and levels off. From

$$C + 2H_2 \rightleftarrows CH_4 \tag{1}$$

the equilibrium constant for 1000°K is

$$K = \frac{P_{CH_4}}{(P_{H_2})^2 a_C} = .097 \tag{2}$$

Measurements of the equilibrium values of the methane and hydrogen pressures yield the carbon activity.

The second method used to obtain the carbon activity involves adding CO (or CO_2) to the loop. From the eventual time stable values of CO and CO_2 the carbon activity and oxygen activity are determined from

$$C + 1/2\ O_2 \rightleftarrows CO \tag{3}$$

$$K_{CO_{1000°K}} = \frac{(P_{CO})}{(P_{O_2})^{1/2}(a_C)} = 3.1 \times 10^{10} \tag{4}$$

and

$$C + O_2 \rightleftarrows CO_2 \tag{5}$$

$$K_{CO_{2_{1000°K}}} = \frac{[P_{CO_2}]}{[P_{O_2}](a_C)} = 5.7 \times 10^{20} \tag{6}$$

So that

$$a_{C_{1000°K}} = 0.59 \frac{[P_{CO}]^2}{[P_{CO_2}]}$$

and

$$a_{O_2\,1000°K} = 3 \times 10^{-21} \frac{[P_{CO_2}]^2}{[P_{CO}]^2}$$

Knowing the oxygen activity, the surface Cr activity and surface FeO activity are obtained from

$$2Cr + 1.5\ O_2 \rightleftarrows Cr_2O_3 \tag{7}$$

$$K_{1000°K} = \frac{Cr_2O_3}{(a_{Cr})^2 (a_{O_2})^{1.5}} = 9 \times 10^{44} \tag{8}$$

and

$$Fe + 1/2\ O_2 \rightleftarrows FeO \tag{9}$$

$$K_{1000°K} = \frac{a_{[FeO]}}{[Fe][a_{O_2}]^{1/2}} = 2 \times 10^{10} \tag{10}$$

(where $a_{Cr_2O_3} = a_{Fe} = 1$).

From these assumptions

$$a_{Cr\,1000°K} = 3 \times 10^{-23}\ [a_{O_2}]^{-3/4} \tag{11}$$

and

$$a_{FeO\,1000°K} = 2 \times 10^{10}\ [a_{O_2}]^{1/2} \tag{11a}$$

2.4.2 Theoretical Equilibrium Water Concentrations

The oxygen activity determined from equilibrium values of CO and CO_2 can be used to calculate the theoretical value of the equilibrium water concentration from

$$H_2 + 1/2\ O_2 \rightleftarrows H_2O \tag{12}$$

$$K_{1000°K} = \frac{H_2O}{H_2} \cdot \frac{1}{(a_{O_2})^{1/2}} = 1.1 \times 10^{10} \qquad (13)$$

$$H_2O = 1.1 \times 10^{10} [H_2] \cdot [a_{O_2}]^{1/2} \qquad (14a)$$

or

$$H_2O = 0.6 \frac{[H_2]\ [CO_2]}{[CO]} \qquad (14b)$$

2.4.3 Preliminary Results Related to Equilibria

As of experiments completed before April 1979, short term (40-100 hours) hydrogen treatment of the loop followed by reactions with CO and/or CO_2 appear to cause activity* changes of the following approximate magnitudes:

	H_2 Treatment	Many CO Reactions
a_C	0.2	0.004
a_{O_2}	7×10^{-26}	2×10^{22} atm.
a_{Cr}	4×10^{-5}	6×10^{-7}
a_{FeO}	0.016	0.28
Stable H_2O/H_2	10^{-2}	0.15
Stable H_2/H_2O	100	7
Stable CO	2000 ppm at 1 atm. = 40 ppm HTGR	5000 ppm or 100 ppm CO at HTGR
Stable CO_2	80 ppm at 1 atm. = 2 ppm HTGR	1100 ppm or 22 ppm at HTGR

Results from preliminary experiments indicate that the surface of the HIL reaches pseudo equilibrium at 1000°K with respect to

a) methane in approximately 10 hours
b) CO_2 in approximately 20 hours
c) H_2O in approximately 50 hours
d) CO in approximately 200 hours

*At present it appears that the activity of carbon may involve complex changes from both carbon in the steel and from surface deposits of carbon from reactions such as $CO + Fe \rightarrow FeO + C$.

2.4.4 Kinetics of CO Removal and CO_2 Production After Hydrogen Firing of HIL

It is well known that in systems with appreciable pressures of CO, the equilibrium between CO and CO_2 is often achieved by a kinetic path through the mechanism

$$2CO \rightleftarrows CO_2 + C \qquad (15)$$

In this case two molecules of CO are removed to form one of CO_2 and the mechanism is ascertained by kinetic measurements of changes in the gas composition.

In the HIL when only CO is added in the concentration range from several hundred to several thousand ppm, the evidence indicates that the CO-CO_2 equilibrium is achieved by rapid production of CO_2 by reaction (15) followed by removal of the excess CO by

$$CO + Fe \rightarrow FeO + C \qquad (16a)$$

or

$$3CO + 2Cr \rightarrow Cr_2O_3 + C \qquad (16b)$$

When equilibrium is achieved it is possible to calculate the oxygen potential from the CO + CO_2 values. Since we have run the above experiments with oxygen potentials from 10^{-22} atm. to 10^{-26} atm. it is likely that in some experiment reactions (16a) and (16b) both contribute to the removal of CO.

In these experiments the CO_2 reaches about 90% of its equilibrium value (at 1000°K) in a few hours, goes through a maximum and then appears to decrease slowly while the CO decreases. Typical results are shown in Figure 2.35 where 6500 ppm were added to the HIL after hydrogen firing of the loop with 100,000-200,000 ppm of H_2 for seven days.

The activities of carbon and oxygen calculated from the hundred hours values of CO ≈ 2,500 ppm and CO_2 ≈ 200 ppm are

$$a_C = 0.018$$
$$a_{O_2} = 1.9 \times 10^{-23} \text{ atm.}$$

It is perhaps worth noting that this oxygen activity implies an appreciable activity of FeO in a chrome steel. The results are also a qualitative indicator of the effectiveness or ineffectiveness of the hydrogen firing procedure.

2.4.5 Mass Spectrometer Analyses

Difficulties have been encountered with the mass spectrometer to be used in the HIL program with respect to measurements of H_2O concentrations (e.g. H_2O adsorbing on walls). For this reason the inlet system has been modified for continuous heating of the sample introduction line. Also, numerous faulty welds have been discovered on the inlet system. While the welds were not leaking to

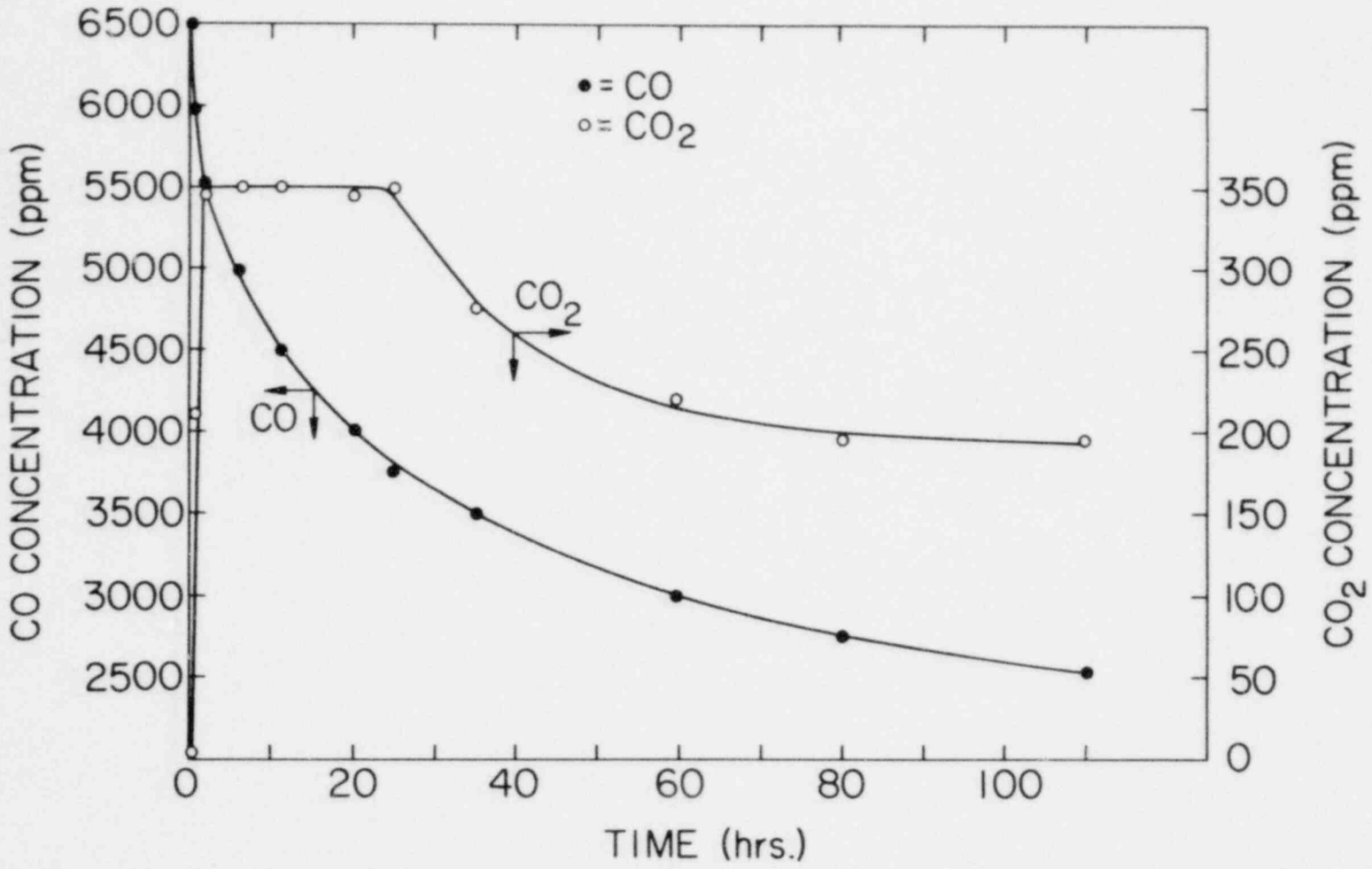

CHANGES IN CO AND CO_2 CONCENTRATION AFTER 7 DAYS OF H_2 TREATMENT (100,000-200,000 ppm) OF HIL AT 1000°K THE TEST ENVIRONMENT CONTAINS 2,000-3,000 ppm H_2 AT 1000°K

Figure 2.35

atmosphere, they did expose the samples to highly porous and carbonaceous surfaces. This, in turn, was responsible for "memory effects" and required excessive pump down times for the inlet system. These welds have been repaired, and all tube socket welds have been replaced with butt welds.

REFERENCES

ORR, J., "A Review of the Structural Characteristics of Alloy 800" in Alloy 800, W. Betteridge, Editor, North Holland Publishing Co., 1978, p. 25.

SOO, P., et al, "Fatigue of Structural Materials" in Reactor Safety Research Programs Quarterly Progress Report, July 1-September 30, 1978, Brookhaven National Laboratory, BNL-NUREG-50931, p. 29.

SOO, P., et al, "Fatigue of Structural Materials" in Reactor Safety Research Programs Quarterly Progress Report, April 1-June 30, 1979, Brookhaven National Laboratory, BNL-NUREG-51082.

SOO, P., et al., "Effect of Fission Product Interactions on the Mechanical Properties of HTGR Metals" in Reactor Safety Research Programs Quarterly Progress Report, January 1-March 31, Brookhaven National Laboratory, BNL-NUREG-51014, May 1979(b), p. 42.

3. Fuel and Fission Products

3.1 High Temperature Vaporization Studies of HTGR Fuel Components and Fission Products (S. Aronson and P. Epstein, Brooklyn College)

Mixtures of H451 graphite powder with ThO_2 and UO_2 powder were heated in the induction heating apparatus to temperatures of about 2000°C. In each run, the graphite crucible containing the mixture was surrounded by carbon felt insulation. Samples of the gas generated in these runs were analyzed by gas chromatography. As was expected, CO was the primary component.

Because the volume of the gas collection and induction heating system is large, about 3 liters, it is necessary to use large oxide-graphite samples to insure that the gas pressure is not limited by sample size. The graphite crucibles which were first fabricated were too small to contain sufficient sample. A number of exploratory runs were made with samples contained in these crucibles. An interesting phenomenon occurred in a run using a mixture of graphite, UO_2 and the simulated fission products, SrO and BaO. The reduction of the alkaline earth oxides by graphite apparently released metallic Ba and Sr which was absorbed into the carbon felt. This markedly changed the coupling characteristics between the high frequency coil and the system, reducing the temperature.

Several larger graphite crucibles were fabricated. In Figure 3.1, the gas pressure data obtained on a mixture of 3.6 grams of ThO_2 and 0.7 grams of graphite are shown. In Figure 3.2 are shown data obtained on a mixture of 2.5 grams of ThO_2, 0.5 grams of graphite and 0.3 grams each of La_2O_3, Nb_2O_5 and Y_2O_3 as simulated fission products. In each run, the sample was first heated to 1200°C and the system was evacuated. The samples were held at each temperature listed in parentheses for at least 20 minutes to bring the pressure to a constant value.

The data will be discussed in detail in the next quarterly report. One phenomenon that is immediately evident is that the pressure changes are not readily reversible. Lowering the temperature does not appreciably reduce the pressure attained at the higher temperature.

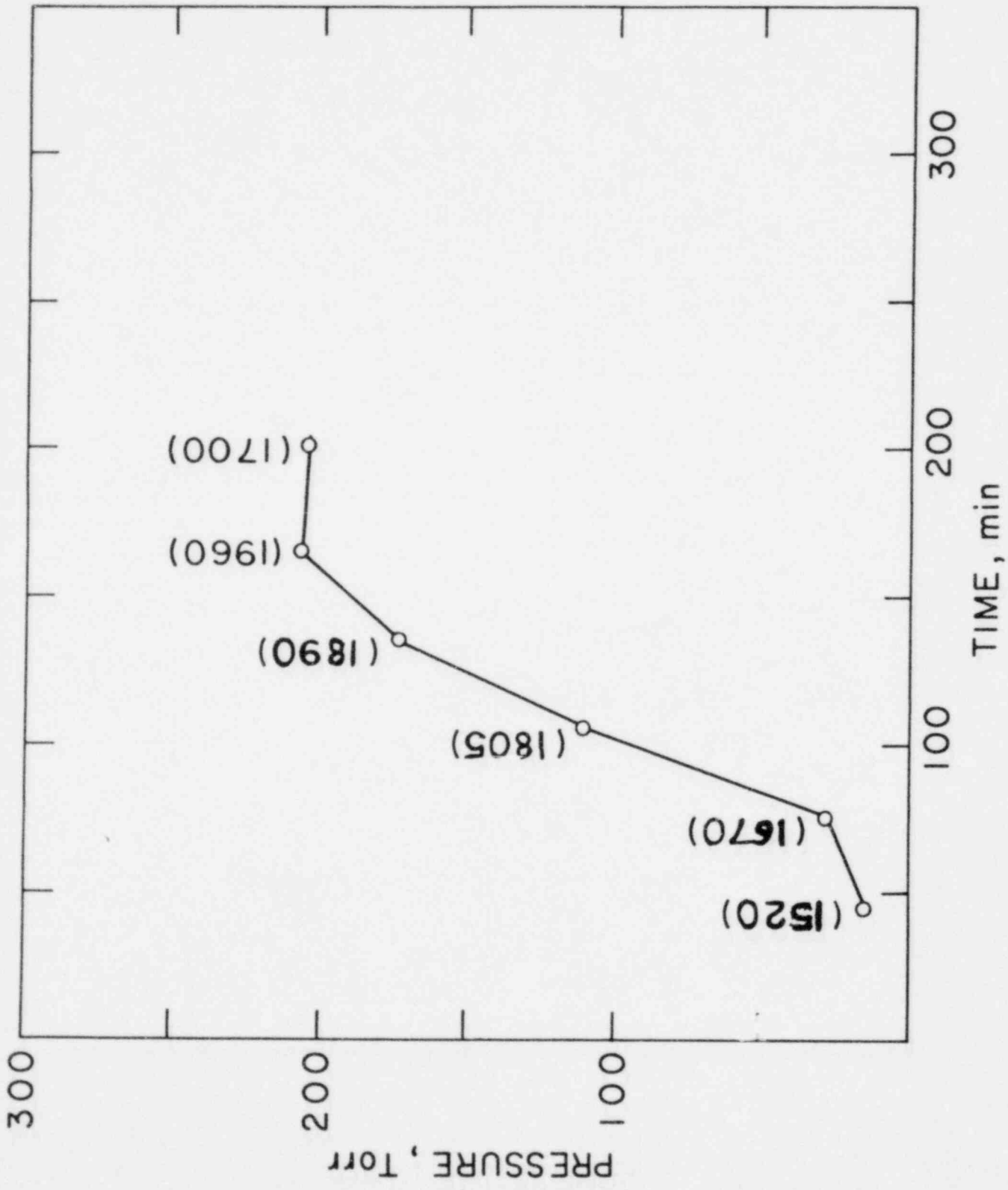

Figure 3.1. Gas pressures at a series of temperatures on a sample of 3.6 grams of ThO_2 and 0.7 grams graphite.

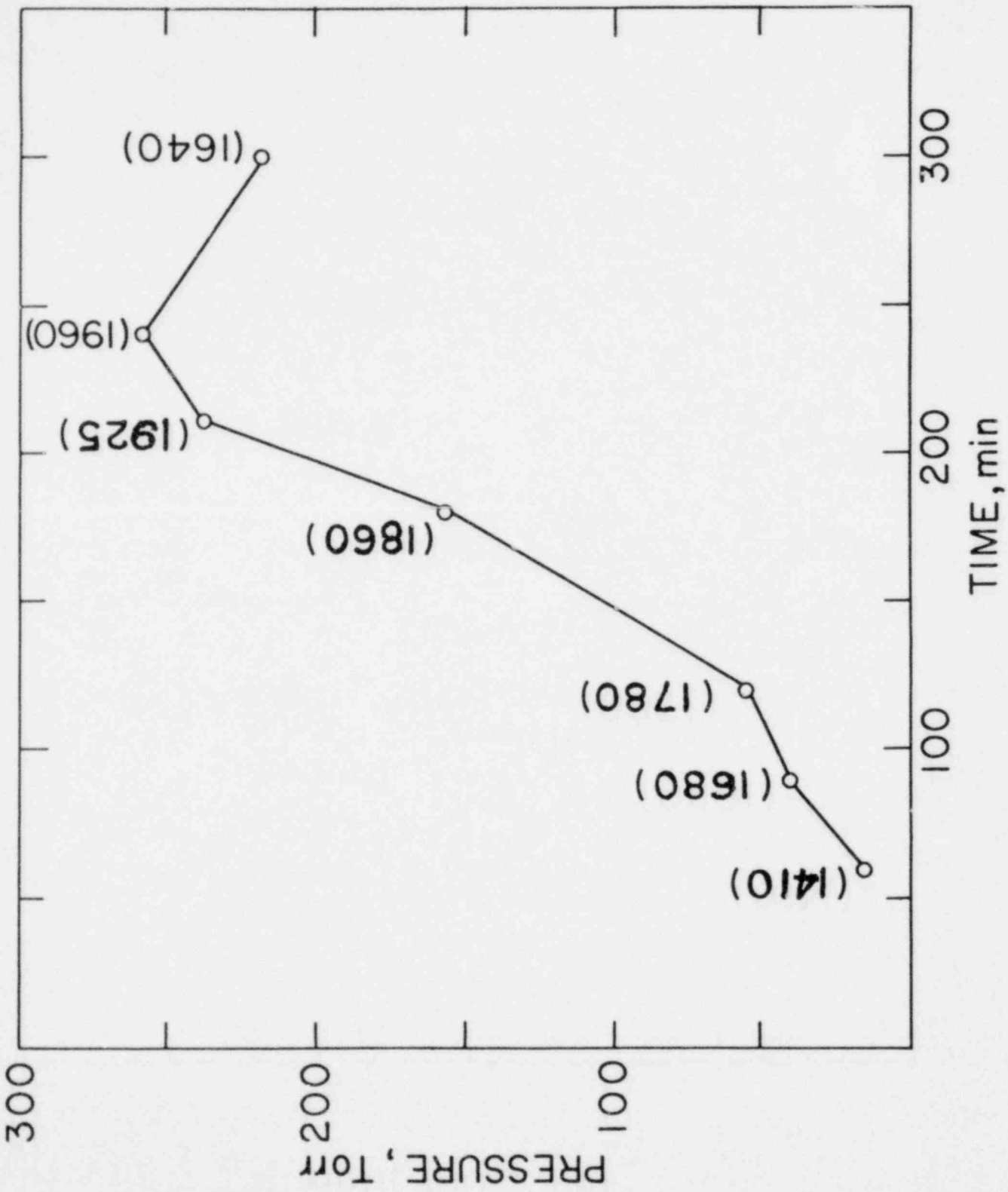

Figure 3.2. Gas pressures at a series of temperatures on a sample of 2.5 grams of ThO_2, 0.5 grams of graphite and 0.3 grams each of La_2O_3, Nb_2O_5 and Y_2O_3.

II. LMFBR SAFETY EVALUATION

SUMMARY

Analysis of the power density distributions in slabs exposed to microwave radiation was performed in order to evaluate the usefulness of microwave radiation for generation of equal volume heating in volumetric boiling pool experiments. The results indicate that standing waves may be generated in the slabs, with resulting large variations in power density. These waves occur due to interference of transmitted waves and also due to interference of the transmitted waves with waves reflected at slab interfaces. Methods for reducing the variations in power density are being explored.

The influence of a heavy entrained phase in an expanding post-disassembly bubble on the development of Rayleigh-Taylor instabilities was investigated. The results of a simplified mathematical analysis indicate that depending on droplet size, the heavy phase may act to decrease the rate of growth of the instability and, hence, to stabilize interfacial disturbance growth, or may have little effect. A mathematical model was derived for the rate of crust growth during molten fluid freezing in a tube. It was assumed that the molten fluid temperature is above its freezing point, and that the fluid is a two-phase gas-liquid mixture. A method of solution is proposed which couples the crust growth [illegible]ction to the fluid momentum equation.

Volume-boiling pool heat transfer data, and derived mechanistic correlations, are presented. Average and local heat transfer results are presented for conditions of bubbly flow and for inclined wall angles of 60°, 75°, and 90°.

The Super System Code (SSC) development program encompasses a series of four codes: SSC-L, SSC-P, SSC-W and SSC-S.

During this quarter the SSC-L code was used to illustrate and quantify the role of bouyancy in governing low-flow behavior of the LMFBR primary system. The results show the importance of accurately specifying the hydraulic profile throughout the loop, as is done in SSC-L.

SSC-L was applied to simulate several ATWS-type transients in an LMFBR design. The results showed the importance of including the plant controls in the system simulation and the need for a nonlinear simulation to adequately predict the response of a nonlinear system.

Further studies were done with SSC-L to analyze the effects of friction, check valve operation and part-load profiles.

Modifications to the SSC program library were instituted to: (1) correct recurrent oscillations in the vessel-to-pump flow rate calculations; (2) correct pump speed initialization at off nominal conditions; and (3) correct and improve in-core temperature response during flow reversal.

The latest cycle of SSC-L, denoted SSC-L export Version-002 was made available to the seven external users of the code.

A substantial effort was completed during this quarter to make the SSC-P code compatible with all the overlapping corrections/improvements which were incorporated into the SSC-L code. A steady-state (null) transient was accomplished with the SSC-P code (without tank energy balance equations).

Under the SSC-W code development effort, work accomplished this quarter included: (1) modification of the primary loop correlations and properties to water; (2) inverting of the steam generator to account for primary fluid being inside the tubes; and (3) achieving a steady-state with SSC-W for a B&W plant design (without aspirator).

During this quarter, the SSC code validation effort continued to focus on the prediction with SSC-L of the FFTF acceptance tests. A 19 channel input deck was prepared and preliminary runs accomplished to simulate four LOEP transients to be conducted at the FFTF.

1. Fast Reactor Assessment - Accident Sequence Studies (O. C. Jones, Jr. and N. Abuaf)

1.1 Liquid Dispersion in Internally Heated Boiling Pools (T. Ginsberg, H. Makowitz, Applied Math Dept. and J. C. Chen, Lehigh University)

The objectives of this task are to conduct experiments and perform analysis to study the dispersive characteristics of internally heated boiling pools. Experiments using internal heat generation are used to simulate nuclear heating, and the two-phase boiling characteristics are studied in open and closed boiling systems with boundary heat losses.

1.1.1 Power Density Distributions in Slabs Exposed to Microwave Radiation

Simulation of fission- or decay-heating with microwave power deposition in two-phase liquid dielectrics has been proposed. In order to effectively model the multiphase fluid dynamics of the system, the spatial distribution of power density must be quantified. Previous experimental and analytical investigations (Johnson, 1972) have shown that severe power density gradients may be generated within samples exposed to microwave radiation fields. On the other hand, it has been suggested that microwave energy deposition in a sample can be computed assuming simple exponential attenuation of the electric field strength through the material (Gabor, 1975). This latter approach ignores the possibility of standing wave development on the sample under irradiation.

Analytical modeling of microwave radiation interaction with dielectric materials is being pursued in order to develop a quantitative understanding of the power density distribution under microwave heating conditions. During this reporting period the problem of determining the power density distribution in homogeneous slabs resulting from single-sided and bilateral microwave irradiation was investigated. Two problems were studied: the first considers the general problem with boundary effects; the second is a simplified problem involving irradiation of an infinite slab in which boundary effects are not included.

A. General Problem With Boundary Effects

Consider the slab shown in Fig. (1.1). The electric field within the slab depends on the relative orientation of the electric and magnetic field vectors, $\bar{E}$ and $\bar{H}$, on the relative phases of the incident plane waves, on the dieletric constants of the slab material, on the wavelength of the incident radiation and on the slab width.

The electric field within the slab shown in Fig. (1.1), when irradiated from the left side only, is due to the interaction of two waves, one which is transmitted across the left surface of the slab, and the other one reflected from the right surface. The field is given by (Von Hippel, 1954).

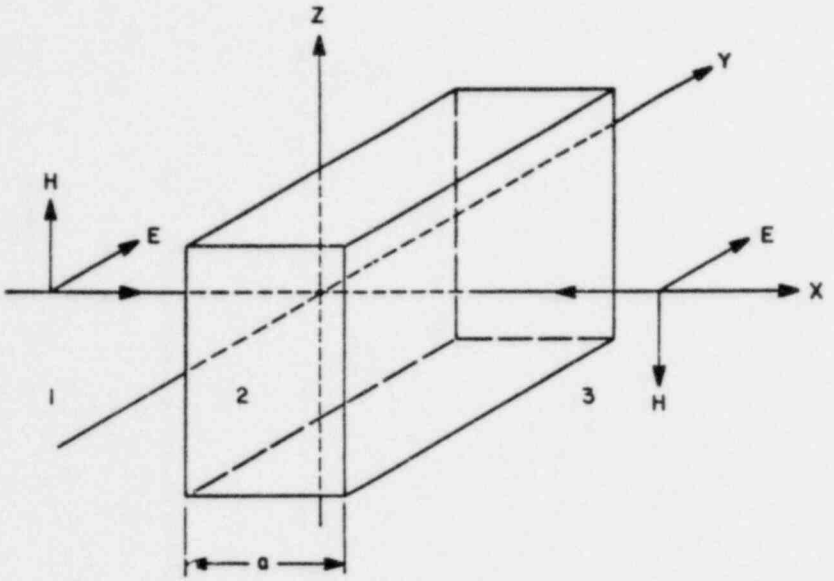

Figure (1.1) - Geometry of Slab With Incident Microwave Radiation. (BNL Neg. No. 11-578-79)

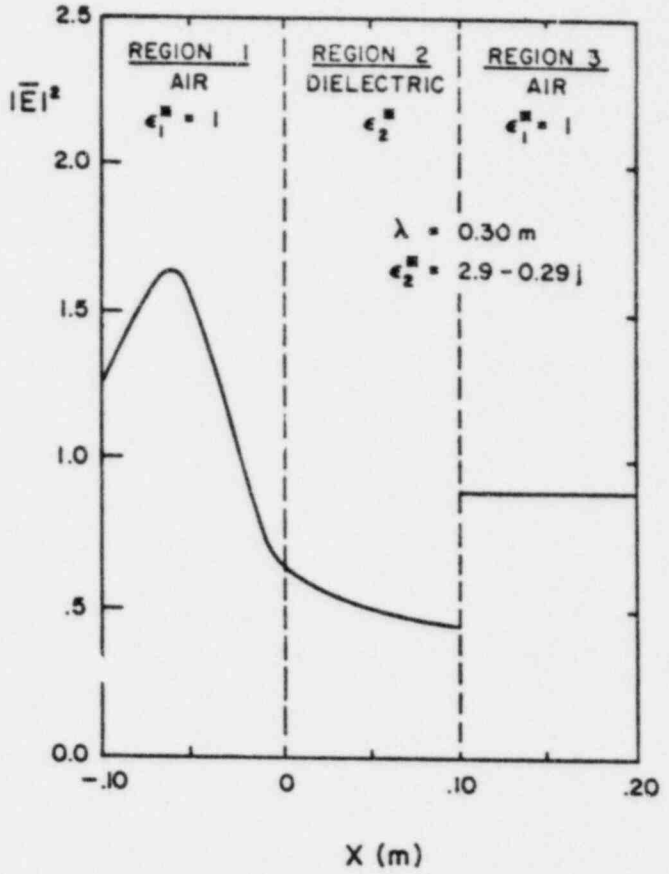

Figure (1.2) - Electric Field Intensity in a Dielectric Slab and Surrounding Air - Radiation Incident From Left Side. (BNL Neg. No. 11-578-79)

The electric field within the slab shown in Fig. (1.1), when irradiated from the left side only, is due to the interaction of two waves, one which is transmitted across the left surface of the slab, and the other one reflected from the right surface. The field is given by (Von Hippel, 1954).

$$E = E_o \tau_o e^{j\omega t} \left(e^{-\gamma_2^* x} + r_1 e^{\gamma_2^* x}\right) \tag{1.1}$$

where

$$r_1 = \frac{Z_1 - Z_2}{Z_1 + Z_2}, \quad \tau_o = \frac{2Z_2}{Z_1 + Z_2} \tag{1.2}$$

$$\gamma_i^* = j\omega\sqrt{\varepsilon_i^* \mu_i^*} \quad ; \; i = 1,2 \tag{1.3}$$

$$Z_i = \frac{\gamma_i^*}{j\omega\varepsilon_i^*} \quad ; \; i = 1,2 \tag{1.4}$$

The parameters appearing in Eqs. (1.1) - (1.4) are

E	electric field
E_o	incident electric field
j	imaginary number $\sqrt{-1}$
r_1	reflection coefficient
t	time
x	position
ε^*	complex permittivity
μ^*	complex permeability
τ_o	transmission coefficient
ϕ	phase angle
ω	frequency

The indices '1' and '2' represent the air and dielectric media, respectively.

If the slab is irradiated from both sides with sources of equal strength and frequency, then the field may be computed by superposition. The resulting field distribution is

$$E = E_o e^{j\omega t} \left\{ e^{-\gamma_2^* x} + e^{(j\omega\phi + \gamma_2^* x')} + r_1 \left[e^{\gamma_2^* x} + e^{-(j\omega\phi + \gamma_2^* x')} \right] \right\} \tag{1.5}$$

where $x - x' = a$. The remaining quantities are as defined in Eqs. (1.2) - (1.4).

The time-average power density (power dissipation per unit volume of dielectric) is given by (Elliot, 1966)

$$P = \frac{\omega}{2} \varepsilon'' \overline{E^2} \tag{1.6}$$

$$= \frac{\omega}{4} \varepsilon'' |E|^2 \tag{1.7}$$

where the over-bar represents a time-average operation, ε'' is the dielectric loss factor and $|E|$ is the absolute value of the electric field.

The quantity $\overline{E^2}$, proportional to the power density via Eq. (1.6), has been computed for the following cases:

(i) slab irradiated from one side only

(ii) slab irradiated bilaterally, with identical frequency sources

Dielectric property data for 0.3 meter wavelength radiation for cyclohexane-ethanol solutions have been used in the calculations.

Figure (1.2) presents the results for single-sided irradiation. The results indicate that standing waves are established in Region 1, due to the interference of the incident radiation and the radiation reflected back from the dielectric medium. Region 3 is characterized by a traveling wave, resulting from transmission through the slab. Interference effects within the dielectric, Region 2, are minimal, and the power density variation (proportional to $\overline{E^2}$) is consequently relatively small.

Figure (1.3) presents results for a slab irradiated from both sides with radiation of identical frequency. The results indicate that a standing wave pattern is generated within the dielectric slab. The interference pattern is due to two effects. First, the waves which are incident on the slab from both directions are transmitted across the medium boundaries. These waves interfere. Second, the waves which are generated within the slab as a result of relection from the interfaces interfere with the transmitted waves. The two peaks observed in Fig. (1.3) near the boundaries are due to the interference of the incident and reflected waves. The broad peak in the center of the dielectric is the result of interference of the transmitted waves. As a result of these effects, severe power density variations are computed across the slab.

The above results indicate that severe power density variations can occur when dielectric slabs are irradiated in single frequency microwave fields. These variations are caused by interference of the waves transmitted across the interface and by interference effects near the boundaries of the medium.

B. Simplified Model: Infinite Dielectric Slab, Bilaterally Irradiated - Different Frequencies

A model was developed to evaluate the effects of irradiating a slab from two sides, with sources of two different frequencies. In order to simplify calculations, the field within an infinite slab was assumed to result from superposition of two traveling waves of different frequency within the dielectric medium. As a result, the effects of dielectric property discontinuities at the boundaries were neglected. The central 0.10 m of the slab is equivalent to Region 2 of Figs. (1.2 - 1.3).

The two waves, traveling in opposite direction are,

$$E_1 = E_o e^{j\omega_1 t} e^{\gamma_1^* x} \tag{1.8}$$

$$E_2 = E_o e^{j\omega_2 t} e^{-\gamma_2^* x} \tag{1.9}$$

The field in the slab is

$$E = E_1 + E_2 \tag{1.10}$$

The time-average power density is given by Eq. (1.6). For the case of $\omega_1 \neq \omega_2$ (Lorrain, 1970)

$$\overline{E^2} = \lim_{T \to \infty} \frac{1}{T} \int_o^T \mathrm{Re}(E)\mathrm{Re}(E)\,dt \tag{1.11}$$

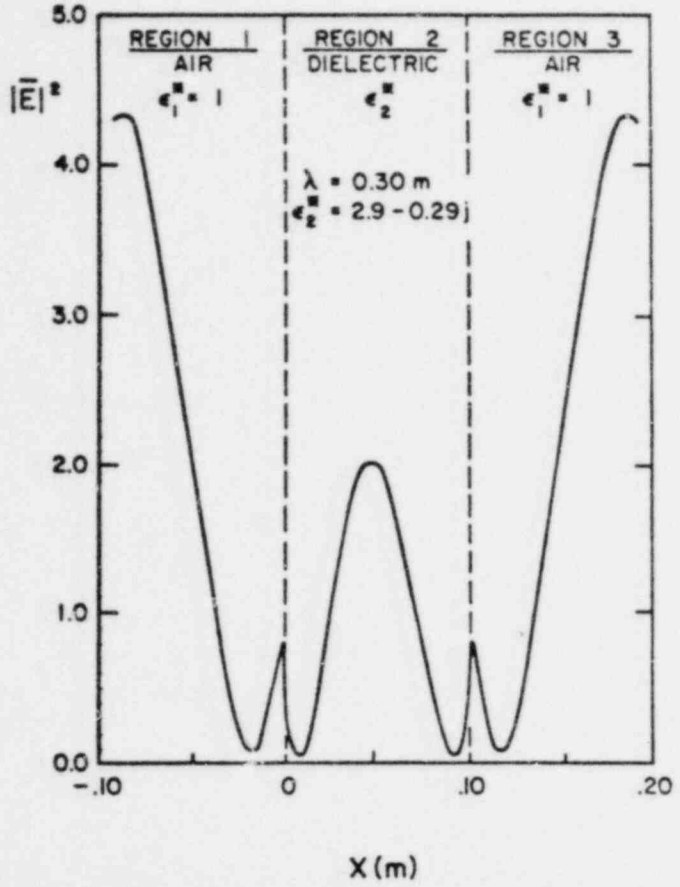

Figure (1.3) - Electric Field Intensity in Slab and Surrounding Air -Bilateral Irradiation. (BNL Neg. No. 11-577-79).

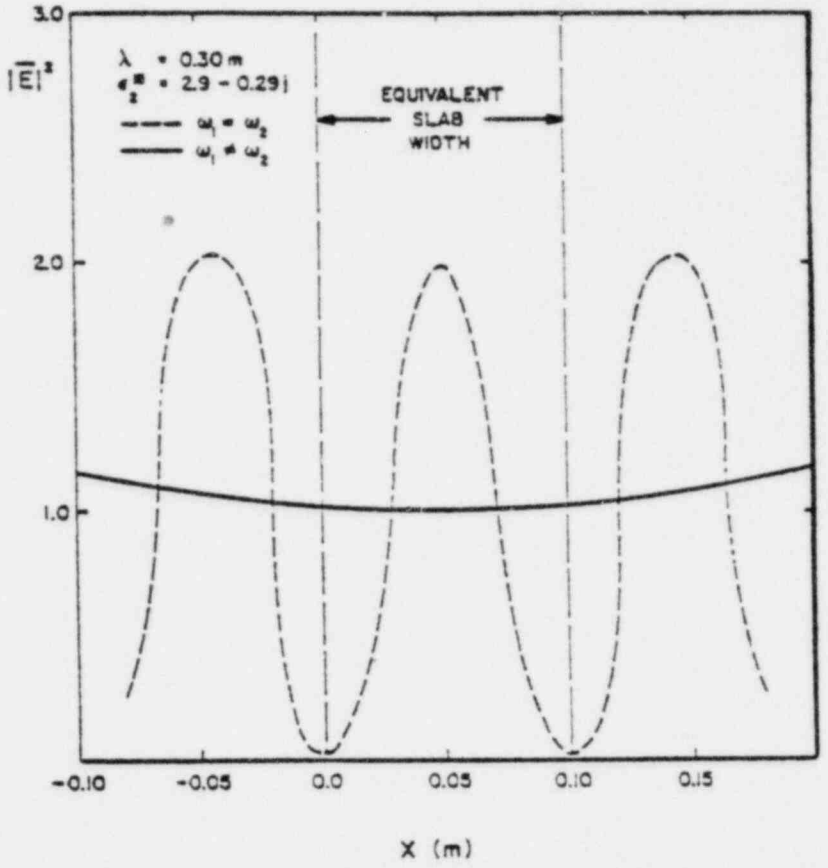

Figure (1.4) - Electric Field Intensity in a Dielectric Material Irradiated Bilaterally. (BNL Neg. No. 11-577-79).

$$= \frac{E_o^2}{2}\left[\cos^2(\xi_1 x)e^{2\delta_1 x} + \cos^2(\xi_2 x)e^{-2\delta_2 x}\right.$$

$$\left. + \sin^2(\xi_1 x)e^{2\delta_1 x} + \sin^2(\xi_2 x)e^{-2\delta_2 x}\right] \tag{1.12}$$

where

$$\delta_i = \frac{2\pi}{\lambda_i}\kappa_i' \tag{1.13}$$

$$\xi_i = \frac{2\pi}{\lambda_i}\kappa_i' \tag{1.14}$$

where λ is the wavelength, κ_i' and κ_i'' are the relative dielectric constant and loss factor, respectively, and where the index i denotes the property values at the two frequencies. For the case where the frequencies ω_1 and ω_2 are close but not identical, the result is

$$\overline{E^2} = E_o^2 \cos h\ (2\delta x) \tag{1.15}$$

For the case $\omega_1 = \omega_2$, Eq. (1.11) yields

$$\overline{E^2} = \frac{1}{2}|E|^2$$

$$= E_o^2\ [\cosh\ 2\delta x + 2\cos^2 \xi x - 1] \tag{1.16}$$

Figure (1.4) presents the results for $\overline{E^2}$ (again proportional to the power density) within the dielectric for the cases $\omega_1 = \omega_2$ and $\omega_1 \neq \omega_2$. The region labeled "EQUIVALENT SLAB WIDTH" is of interest in comparison with

Figs. (1.2) and (1.3). For the case $\omega_1 = \omega_2$, the two waves interfere to form a standing wave pattern within the dielectric, characterized by severe power density gradients. The behavior is similar to that observed in Fig. (1.3), except that the edge affects are not accounted for in Fig. (1.4). For $\omega_1 \neq \omega_2$, the superposition of two waves does not lead to development of a standing wave pattern in the medium. In this case, the observed variation in power density is quite small, and is due only to the exponential decay of the field strengths through the medium. With the dielectric properties of the cyclohexane-ethanol solution, the power density variation across a 10 cm slab would be less than 2 percent. For a 30 cm slab, the variation would be less than 15 percent.

C. Conclusion

The above analysis indicates that standing waves generated within a dielectric exposed bilaterally to microwave radiation leads to strong variation in power density across the material. The standing waves may develop as a result of interference of the transmitted waves within the medium, and also as a result of interference effects at the medium boundaries.

The results suggest that if a dielectric medium is exposed bilaterally to sources of radiation of two different frequencies, and if boundary interference effects can be minimized, then power density variations within the dielectric would be minimized. These ideas are being explored with microwave equipment vendors in our search for an optimum microwave heating apparatus for the volume-heated boiling experiments.

1.2 HCDA Bubble Energetics: Role of Taylor Instabilities (J. Moszynski and T. Ginsberg)

The objective of this task is to characterize the mechanisms of entrainment of liquid sodium into the post-disassembly multi-phase bubble during a hypothetical core disruptive accident in an LMFBR. The present effort is directed primarily toward analysis of the influence of the heavy liquid phase of the bubble on the growth rate of Taylor instabilities.

1.2.1 Effect of Dispersed Condensed Phase on the Rayleigh-Taylor Stability of a Gas-Liquid Interface

It has been suggested that sodium entrainment into an expanding HCDA bubble could occur as a result of the growth of Rayleigh-Taylor instabilities at the liquid-sodium/bubble interface. If it is assumed that the vapor within the bubble expands against, and accelerates, the overlying sodium, then the Taylor theory (Taylor, 1950) predicts that disturbances supplied to a planar interface would grow exponentially. The "fingers" that result from the instability growth mechanism may lead to entrainment of liquid into the expanding bubble.

The expanding bubble, however, is a multiphase mixture of vapor and liquid and/or solid UO_2 and steel. The presence of the heavy particles may affect the Rayleigh-Taylor stability of the interface. The effect of the particles can be estimated in a simplified calculation which considers the two-phase bubble as a homogeneous mixture with a mixture density equal to the volume-weighted sum of the component densities. Assume that the liquid or solid fuel or steel density to be about ten times that of the liquid sodium. It is found that when the bubble void volume fraction is 90 percent, then the mixture density equals that of the overlying liquid sodium pool. The Taylor theory predicts that when the fluid densities on either side of the interface are equal, then the instability vanishes. For void fractions less than 90 percent, then, this reasoning leads to the conclusion that no instability is possible. The implication, therefore, is that the entrainment by Taylor instability would not be possible in this range of bubble void fraction.

The above argument is highly simplified. The particles are very heavy, and probably do not follow the gas motion. The Taylor model probably is inadequate under these circumstances. A more rigorous investigation of the Taylor instability mechanism in systems involving multiphase fluids is required in order to evaluate the effect of the heavy component.

In order to estimate the effects of the particles, a model is considered in which the particles are assumed to have infinite inertia. A fixed particle system, with gas flow past them, is modeled by a porous matrix. Flow through the particle matrix is assumed to follow Darcy's law, where the matrix is characterized by a permeability, k. The analysis that follows is an adaptation of one proposed by Saffman (1958). In the first approximation, viscosity of the liquid and the surface tension are neglected. This allows the introduction of a disturbance velocity potential. In the upper fluid (liquid), denoted by the subscript 1,

$$\phi_1 = Ae^{-\kappa y + nt} \tag{1.17}$$

$$p_1 = p_o - a\rho_1 y + \rho_1 \frac{\partial \phi_1}{\partial t} \tag{1.18}$$

where

a	acceleration of the liquid interface
n	disturbance growth constant
p	pressure
p_o	constant
t	time
y	coordinate normal to and measured from interface
ρ	density
ϕ	velocity potential
κ	disturbance wave number

The lower fluid (gas-particle mixture denoted by the subscript 2), is assumed to obey Darcy's law

$$V_2 = -\frac{k}{\mu_2}\left(\frac{\partial p_2}{\partial y} + \rho_2 a\right) = -\frac{\partial \psi}{\partial y} \tag{1.19}$$

and

$$p_2 = p_o + \frac{\mu_2}{k}\psi_2 - a\rho_2 y \tag{1.20}$$

where μ_2 is the viscosity of the gas, k the permeability of the matrix, v_2 the velocity component in the y-direction, and ρ_2 is the gas density.

We put,

$$\psi_2 = -Ae^{\kappa y + nt}\cos \kappa x \tag{1.21}$$

where x is the coordinate parallel to the interface. Equation (1.21) satisfies the requirement that when $y = 0$, $v_1 = v_2$. Equating pressures at the interface we obtain the dispersion equation

$$n^2 + \frac{\mu_2}{\rho_1 k} n + \frac{\rho_2 - \rho_1}{\rho_1} a\kappa = 0$$

and (1.22)

$$n = -\frac{\mu_2}{2\rho_1 k} \pm \sqrt{\left(\frac{\mu_2}{2\rho_1 k}\right)^2 + \left(1 - \frac{\rho_2}{\rho_1}\right) a\kappa}$$

Equation (1.22) is the "dispersion relation" for the particle-vapor system modeled as a porous matrix medium. The magnitude of n determines the rate of growth of the instability, as shown by Eq. (1.17).

In the absence of viscosity and surface tension, the classical Taylor theory gives the dispersion relation

$$n_o = \sqrt{a\kappa \frac{\rho_1 - \rho_2}{\rho_1 + \rho_2}} \tag{1.23}$$

Examination of Eq. (1.22) indicates that as the permeability of the medium gets sufficiently large, the growth constant of the porous medium approaches the classical Taylor limit.

Numerical results are presented for two fluids systems: (i) a nitrogen bubble growing into water, and (ii) a gas-particle mixture growing into a water pool, where the gas-particle mixture density is equal to the water density.

Consider first the system often used to experimentally model the fuel vapor - liquid sodium system, namely nitrogen - water, where $\rho_2 << \rho_1$. The accelerations in these experiments fall in the range from 1 to 1000 g or approximately 10 - 10000 m/s^2. The wave numbers κ of interest range from 0 to a maximum cut-off value, determined by the surface tension κ and given by (Taylor, 1950)

$$\kappa_{MAX} = \sqrt{\frac{(\rho_1 - \rho_2)a}{\sigma}} \tag{1.24}$$

This represents the maximum wave number for which applied disturbance will grow. Surface tension prevents growth of the disturbance for larger κ. For water $\rho_1 = 1000\ kg/m^2$, $\sigma = 0.073$ n/m. Table (1.1) presents the cut-off wave numbers as a function of interfacial acceleration for this system. Table (1.2) shows the growth constants, n_o, obtained from Eq. (1.23). For each acceleration, values of n_o are presented for the range of wave numbers indicated in Table (1.1).

The growth constant n was computed via Eq. (1.22) using the Brinkman (Scheidegger, 1957) relationship for the permeability, i.e.,

$$k = \frac{r^2}{18}\left[3 + \frac{4}{1-\alpha} - 3\sqrt{\frac{8}{1-\alpha} - 3}\right] \tag{1.25}$$

For a given void fraction, the permeability is proportional to the square of the particle radius.

It is assumed that the void fraction of the particle matrix is 0.9. Considering particle radii of 10^{-6}m, 10^{-5}m and 10^{-4}m respectively,

TABLE (1.1)

CUT-OFF WAVE NUMBERS ACCORDING TO TAYLOR THEORY

$a\,(m/s^2)$	10	100	1000	10000
$\kappa_{max}\,(m^{-1})$	370	1170	3701	11703

TABLE (1.2)

GROWTH CONSTANT PREDICTED BY TAYLOR THEORY

$a = 10\ m/s^2$	$\kappa\,(m^{-1})$	10	50	100	200	400
	$n_o\,(s^{-1})$	10	22.4	31.6	44.8	63.2
$a = 100$	κ	10	100	1000	1200	
	n_o	31.6	100	316	346	
$a = 1000$	κ	10	100	1000	4000	
	n_o	100	316	1000	2000	
$a = 10000$	κ	10	100	1000	10000	12000
	n_o	316	1000	3160	10000	10950

(1, 10 and 100 μm) the permeabilities are $0.93 \times 10^{-12} m^2$, $0.93 \times 10^{-10} m^2$, and $0.93 \times 10^{-8} m^2$. Taking for air (or nitrogen) at room temperature $\mu_2 = 1.2 \times 10^{-5}$ kg/m s, one obtains $\mu_2/2\rho_1 k = 6450$, 64.5 and 0.645 respectively. Equation (1.22) was used to compute the growth constants, n.

Table (1.3) presents, for each acceleration and for a range of wave numbers, the magnitudes of the growth constants n_1, n_2, n_3 corresponding to the permeabilities described above. Note that n_1, n_2, and n_3 correspond to particle radii of 1 μm, 10 μm and 100 μm, respectively. Also presented for comparison are the Taylor theory predictions from Table (1.2).

The results presented in Table (1.3) display the stabilizing influence of flow past the stationary spheres. The smaller the particle radius and, hence, the smaller the permeability of the particle matrix, the smaller is the growth constant. For example, consider a liquid interface acceleration of $a = 100$ m/s^2. For a wave number $\kappa = 1000$, the growth constants for 1 μm, 10 μm, and 100 μm particles, respectively are, 7.75, 258, and 315. This result implies that for $\alpha = 0.90$, the disturbance growth rates are strong functions of the permeability, i.e., particle size. The existence of the heavy phase can play a stabilizing role on the growth of Taylor instabilities.

The above results suggest that even with a void fraction as high as 90 percent, the stabilizing effect of the discrete heavy phase in two-phase expanding bubbles may be very substantial, particularly for the 1-10 μm range of condensed particles. The effect becomes almost insignificant as the particle size increases to the 100 μm range. For a given particle size increasing the void fraction increases the permeability and reduces the stabilizing effect.

Under reactor conditions the liquid density (sodium) ρ, would be less than that of water used here, and the gas viscosity μ_2 would be much higher than the cold air viscosity. Both these effects would increase the parameter $\mu_2/2\rho_1 k$ and would increase the stabilizing effect for a given void fraction and particle size.

The porous matrix model of the two-phase flow within an expanding bubble, employed here in conjunction with the analysis of liquid interfacial stability, supports the hypothesis that the heavy entrained phase acts to stabilize the growth of Taylor interfacial disturbances. The major implication of this work is that the heavy entrained phase of HCDA bubbles must be accounted for in analyses of Taylor instability at the accelerating bubble interface. It is conceivable that the proposed Taylor instability entrainment may not be possible in the presence of a heavy entrained phase.

The extension of the porous matrix model to account for liquid viscosity and surface tension is in progress. A more general model, allowing for finite particle inertia is under consideration.

TABLE (1.3)

GROWTH CONSTANTS:
POROUS MATRIX THEORY (n_i) and TAYLOR THEORY (n_o)

$a = 10\ m/s^2$	κ	10	50	100	200	400
	n_0	10	22.4	31.6	44.8	63.2
($r = 1\ \mu m$)	n_1	0.008	0.04	0.08	0.16	0.31
($r = 10\ \mu m$)	n_2	0.8	3.8	7.3	14.0	25.8
($r = 100\ \mu m$)	n_3	9.4	21.6	31.0	44.2	62.6
$a = 100\ m/s^2$	κ	10	100	1000	1200	
	n_0	31.6	100	316	346	
	n_1	0.08	0.78	7.75	9.30	
	n_2	7.3	54.5	258	288	
	n_3	31.0	99.4	315	345	
$a = 1000\ m/s^2$	κ	10	100	1000	4000	
	n_0	100	316	1000	2000	
	n_1	0.78	7.75	77.1	303	
	n_2	54.5	258	938	1937	
	n_3	99.4	315	999	1999	
$a = 10000\ m/s^2$	κ	10	100	1000	10000	12000
	n_0	316	1000	3160	10000	10950
	n_1	7.75	77.1	733	5450	6260
	n_2	258	938	3098	9936	10890
	n_3	315	999	3159	9999	10949

The review of experiments and models concerning coolant entrainment by the expanding post-disassembly bubble has been completed and a report is in preparation.

1.3 Solidification Dynamics of Flowing Fluids (G. A. Greene)

The purpose of this task is to study and characterize the solidification dynamics of multiphase mixtures in channels by use of simulant materials in order to develop a basic phenomenological understanding. This effort highlights the extension of the two-phase conduction freezing model to include the general case that the fluid is initially at a temperature above its freezing temperature.

1.3.1 Mathematical Development - Freezing Rate

In the general case of solidification of a flowing fluid with sensible heat, i.e., $T_\ell > T_f$, the following equation represents the convection-conduction energy balance at the freezing interface

$$k_s \left.\frac{\partial T_s}{\partial r}\right|_i + h(T_\ell - T_f) = \rho h_{fs} \frac{\partial R}{\partial t} \tag{1.27}$$

where k is the thermal conductivity, h is the liquid heat transfer coefficient, h_{fs} is the heat of fusion, T_s, T_ℓ, and T_f are the solid, liquid, and fusion temperatures, respectively, ρ is the density, and r is the radial coordinate; the terms on the left are heat conducted away from the interface and heat convected to the interface, and the term on the right is the difference between the two, the rate of heat of fusion released due to solidification at the interface. The heat transfer coefficient, strictly speaking, is not a constant in these problems since the flow rate, and hence, the Reynolds number varies during the transient.

Following the mathematical procedure outlined previously (Greene, 1978), the interfacial energy balance may be combined with the solid region energy equation to arrive at the dimensionless crust growth relation indicated below,

$$\left(\frac{d\beta}{d\tau}\right)^2 - Bi\ \theta_\ell N_{pch} N_\rho \left(\frac{d\beta}{d\tau}\right) = \frac{\gamma^2}{(\beta \ell n \beta)^2} \tag{1.28}$$

subject to the following conditions:

$$\beta = 1 \quad @ \quad \tau = 0$$

$$\beta \to 0 \quad @ \quad \tau \to \tau_{plug}$$

1.3.2 Dimensionless Parameters

The dimensionless variables are defined as:

dimensionless centerline-to-crust coordinate $\beta = \frac{R}{R_o}$

dimensionless time $\tau = \frac{a_s t}{R_o^2(1 - \alpha)^{1/2}}$

where R_o is the unfrozen tube radius, a_s is the thermal diffusivity, and α is the gas void fraction.

The dimensionless scaling parameters are:

Biot number $\quad Bi = \frac{hR_o}{k_s}$

Density ratio $\quad N_\rho = \frac{\rho_s}{\rho_\ell}$

Phase change number $\quad N_{pch} = \frac{C_p(T_f - T_w)}{h_{fs}}$

Dimensionless Temperature Difference $\quad \theta_\ell = \frac{T_\ell - T_f}{T_f - T_w}$

Freezing Parameter $\quad \gamma = \sqrt{1 + 2N_\rho N_{pch}} - 1$

Note that modeling the effect of the gas void fraction enters through the dimensionless time as previously shown (Greene, 1978).

1.3.3 General Solution Behavior

For the case that $\theta_\ell = 0$ (i.e., $T_\ell = T_f$), Eq. (1.28) reduces to the form beldw

$$\left(\frac{d\beta}{d\tau}\right)^2 = \frac{\gamma^2}{(\beta \ell n \beta)^2} \tag{1.29}$$

subject to the same initial conditions. This form is identical to the original derivation for freezing of fluids at their fusion temperature, demonstrating that Eq. (1.28) is a more general form.

Noting that Eq. (1.28) is a quadratic equation in $d\beta/d\tau$, we can directly take the roots to find the rate of crust growth as follows:

$$\frac{d\beta}{d\tau} = \frac{Bi\ \theta_{\ell} N_{\rho} N_{pch}}{2} \pm \sqrt{\frac{(Bi\ \theta_{\ell} N_{\rho} N_{pch})^2}{4} + \left(\frac{\gamma}{\beta \ell n \beta}\right)^2} \tag{1.30}$$

Assuming $Bi\ \theta_{\ell}\ N_{\rho} N_{pch} \ll 2\gamma/\beta \ell n \beta$, the first term may be neglected under the root sign. Under these conditions, we find

$$\frac{d\beta}{d\tau} = \frac{Bi\ \theta_{\ell} N_{\rho} N_{pch}}{2} + \frac{\gamma}{\beta \ell n \beta} \tag{1.31}$$

since the positive root corresponds to the physically real case of freezing from the inside wall of a tube toward the centerline. Note, as $\theta_{\ell} = 0$, Eq. (1.31) reduces immediately to Eq. (1.29) as one should expect.

Note that the term $\gamma/\beta \ell n \beta$ is always negative indicating crust growth in the radial direction inward (negative direction). The term $Bi\ \theta_{\ell} N_{\rho} N_{pch}$ is always positive and has the effect of slowing down the crust growth. In addition, for the case that these two terms are equal in magnitude, $d\beta/d\tau \equiv 0$, and the steady centerline-to-crust distance is given simply by

$$(\beta \ell n \beta)_{ss} = -\frac{2\gamma}{\beta i \theta_{\ell} N_{\rho} N_{pch}} \tag{1.32}$$

Rigorous solution to the transient and steady state cases requires knowledge of the transient evolution of the Biot number, Bi(t), which contains two time-varying terms, the heat transfer coefficient, h, and the hydraulic diameter for flow, d_h, both of which decrease during transient solidification. Choosing Bi and θ_{ℓ} based upon initial inlet values will insure the slowest crust growth since these will be the maximum values for Bi and θ_{ℓ}.

The mass flow rate per unit area, G_o is defined as

$$G_o = \left[\frac{2\rho_{\ell} D_o^{1.25}\ \Delta P_f}{.316\ \mu_{\ell}^{.25} L\ \phi_{LO}^2}\right]^{0.57} \tag{1.33}$$

where ρ_ℓ is the liquid density, μ_ℓ is the liquid viscosity, L is the channel length, ΔP_f is the frictional pressure drop, D_o is the initial channel hydraulic diameter and the two-phase frictional multiplier is $\phi^2_{LO} \sim 1/(1 - \alpha)$ (Greene, 1978). It may be readily shown that the mass flow rate varies with the unobstructed flow diameter as follows:

$$\frac{\dot{m}(t)}{\dot{m}_o} \sim \beta^{2.71} \tag{1.34}$$

Equation (1.34) requires the frictional pressure drop of the total pressure drop. This may be determined by iterative solution to Eq. (1.33) and the appropriate form of Bernoulli's equation. An initial flow velocity, $V_o(\tau = 0)$, is guessed and used in Bernoulli's equation to solve ΔP_f. This in turn is substituted into Eq. (1.33) to solve for $V_o'(= G_o/\rho A_o)$. This procedure is repeated until $V_o' = V_o$. From this, the Reynolds number and hence, the initial Nusselt and Biot numbers can be computed, and the crust growth and flow rate may be computed. It will be necessary to recalculate the Biot number and flow rate, G(t), at each time step.

This set of equations will be solved numerically and results will be compared to the experimental data previously reported.

1.4 Boiling Pools With Internal Heat Generation (G. A. Greene and C. E. Schwarz)

The purpose of this task is to study and characterize local boundary heat transfer and void distributions in volume-heated boiling pools in flow regimes applicable to LMFBR accident conditions. Experiments have been performed at wall angles 90° (vertical), 75°, and 60°. Models have been developed for local and average heat transfer correlations and void fraction distributions.

1.4.1 Average Boiling Heat Transfer Correlations in Bubbly Flow

The development of the modeling assumptions of modified natural convection (two-phase) and void distribution have been presented in (Greene, 1977; 1979a). Experimental data has indicated that the average void fraction exists in two dominant flow regimes, bubbly and churn-turbulent, and that each regime influences the behavior of the boundary heat transfer.

For the bubbly flow regime, it was found that heat transfer was controlled by the formation of a natural convection boundary layer and the modeling parameters were developed as

$$Nu = f(Gr^* \cdot Pr) \tag{1.35}$$

where Nu = hx/k, $Gr^* = g\bar{\alpha}x^3\cos\theta/\nu^2$, and Pr = μc/k. For the bubbly flow regime, it was found that, for the range of the experiments performed, the average boundary heat transfer correlations derived were

$$\overline{Nu} = 1.54\ Ra^{*0.25} \qquad Ra^* < 1.86 \times 10^{11} \tag{1.36}$$

and

$$\overline{Nu} = 0.0314\ Ra^{*0.40} \qquad Ra^* > 1.86 \times 10^{11} \tag{1.37}$$

where $Ra^* = Gr^* \cdot Pr$. In the bubbly flow regime and for these experiments, it was found that the average void fraction, $\bar{\alpha}$, could be approximately represented as a function of the dimensionless superficial vapor velocity, $j_{g\infty}/U_\infty$, as

$$\bar{\alpha} \sim 0.75\left(\frac{j_{g\infty}}{U_\infty}\right) - 0.15 \tag{1.38}$$

for $j_{g\infty}/U_\infty$ in the range (0.2, 1.0).

1.4.2 Local Boiling Heat Transfer Correlations in Bubbly Flow

The local heat transfer coefficient is necessary for calculating local melt rates or heat loads from a volume-boiling pool to boundaries of the pool. It has been found that local heat transfer from a boiling pool may vary by as much as a factor of 5 or more spatially (see Greene, 1979b).

The local heat transfer coefficients have been measured for boiling pools in the bubbly and churn-turbulent flow regimes. The detailed experimental data may be found in (Greene, 1979a). The correlation procedure was the same as indicated in Eq. (1.35) and (Greene, 1977, 1979a).

The bubbly flow regime data were correlated at three wall angles, 90° (vertical), 75°, and 60°. These data are presented in Figs. (1.5a - 1.5c) for $Ra^* < 2 \times 10^{11}$. The data for $Ra^* > 2 \times 10^{11}$ appeared to behave differently and were correlated separately [see Fig. (1.6)]. The variations in the correlations at 90°, 75°, and 60° were deemed to be due only to experimental uncertainty and not due to a real systematic effect. As a result, the following local heat transfer correlations were developed for the bubbly flow regime:

$$Nu(x) = (1.41 \pm 0.24)\ Ra^{*0.25} \qquad Ra^* < 7.36 \times 10^{11} \tag{1.39}$$

and

$$Nu(x) = (0.0234 \pm 0.0020)\ Ra^{*0.40} \qquad Ra^* > 7.36 \times 10^{11} \tag{1.40}$$

Note that the numbers specified for transition in equations 1.36, 1.37, 1.39, and 1.40 represent the numerical crossover points only. While these are expected to reflect the physical transition from laminar to turbulent bubbly flows, the variation is probably representative of both the variation in this transition and the scatter in the data. In fact, if the lower 1σ value for the coefficient in equation 1.39 is taken, (i.e., 1.17 rather than 1.41), then the intersection is calculated to be 2×10^{11} exactly.

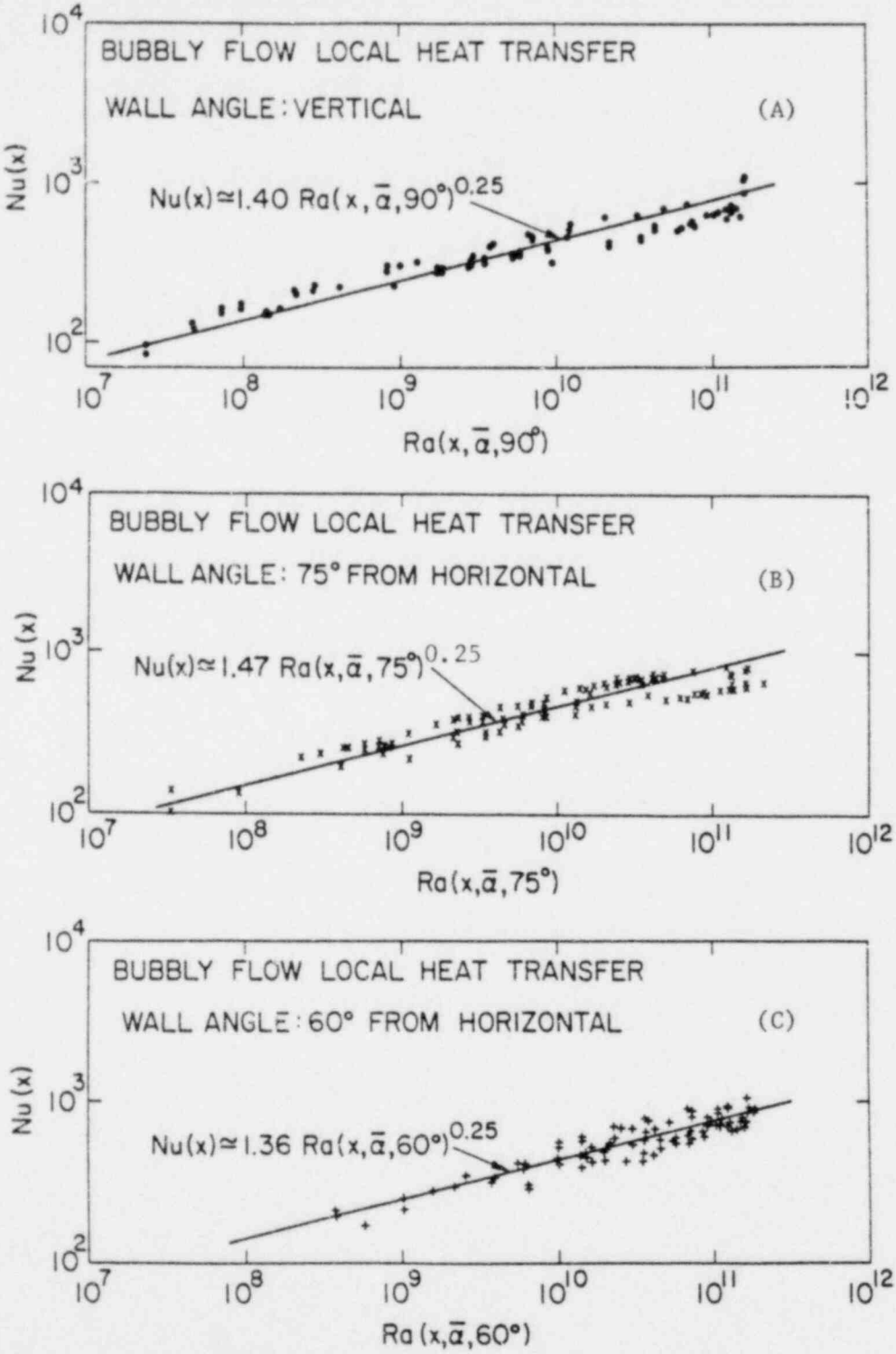

Figure (1.5) - Correlation of Local Heat Transfer Data from Volume-Boiling Pools in Bubbly Flow, $Ra^* \leq 2 \times 10^{11}$ (BNL Neg. Nos. 10-1060-79, 10-1061-79, 10-1062-79).

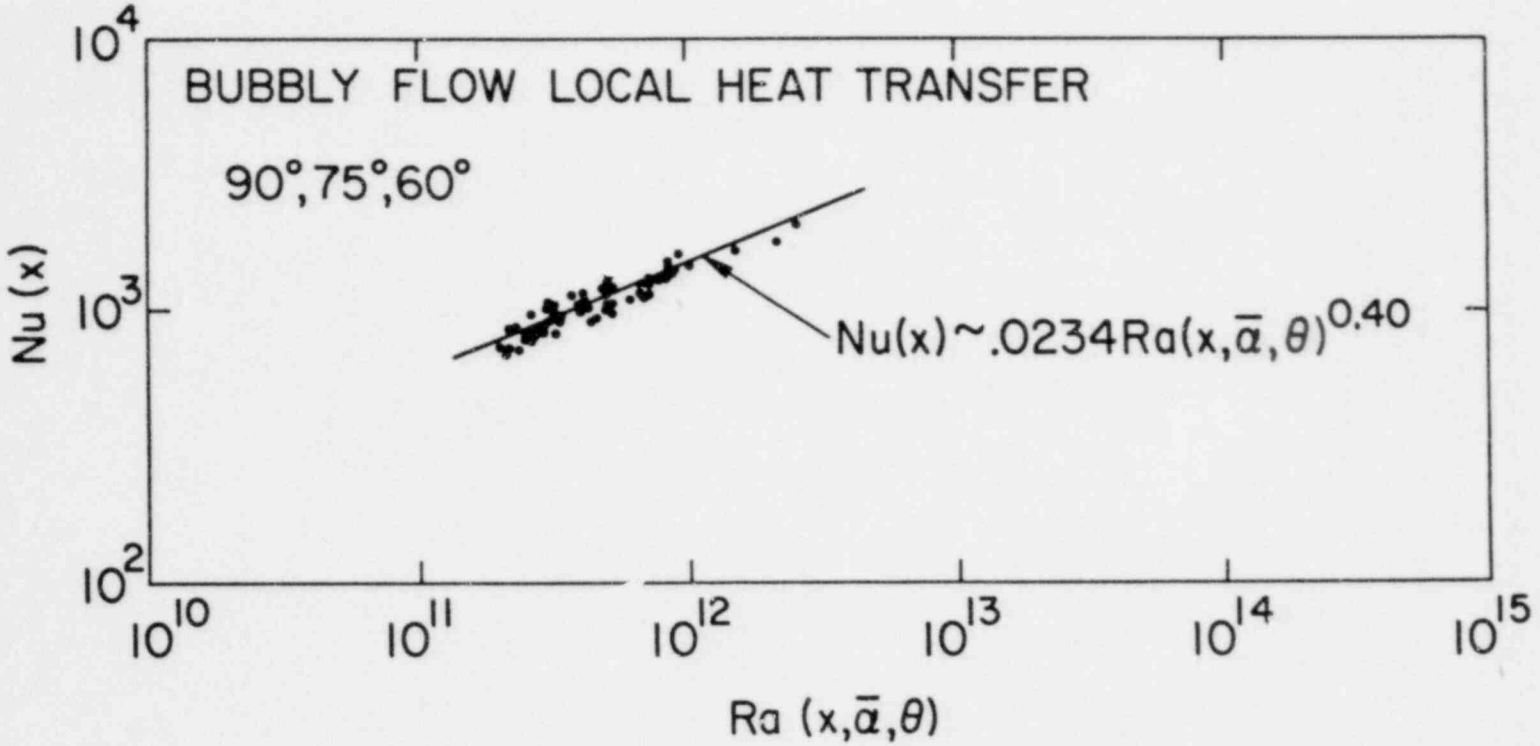

Figure (1.6) - Correlation of Local Heat Transfer Data From Volume-Boiling Pool: $Ra^{*} > 2 \times 10^{11}$. (BNL Neg. No. 10-1063-79).

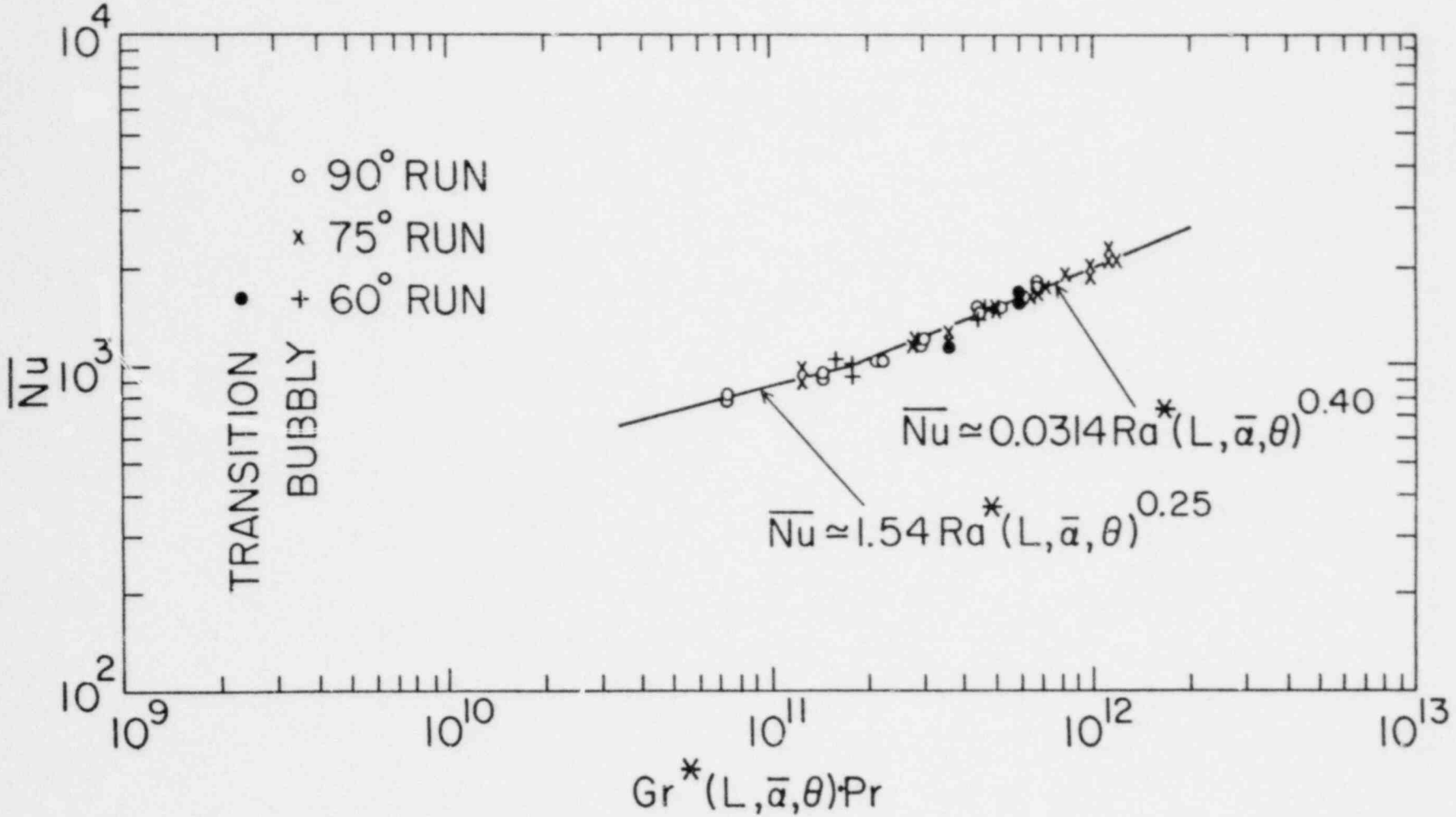

Figure (1.7) - Correlation of Average Heat Transfer Da From Volume-Boiling Pool in Bubbly Flow. (BNL Neg. No. 4-1305 -79).

REFERENCES

ELLIOT, R. S., Electromagnetics, McGraw-Hill Book Company, New York (1969).

GABOR, J. D., et al., "Feasibility Study on the Simulation of Large Meltdown Processes," ANL/RAS 75-40 (October 1975).

GREENE, G. A., JONES, O. C., JR, AND SCHWARZ, C. E., "Thermo-Fluid Mechanics of Volume-Heated Boiling Pools," Proceedings of the Third Post-Accident Heat Removal Information Exchange, ANL 78-10, BNL-NUREG-50759 (November 1977).

GREENE, G. A., JONES, O. C., JR., KAZIMI, M. S., BARRY, J. J., AND ZIMMER, G. A., "Two-Phase Transient Solidification Dynamics of Flowing Fluids With Non-Condensable Vapors," BNL-NUREG-24486R (April 1978).

GREENE, G. A., ABUAF, N., JONES, O. C., JR., AND SCHWARZ, C. E., "Heat Removal Characteristics of Volume-Heated Boiling Pools With Inclined Boundaries," BNL-NUREG-26325 (May 1979a).

GREENE, G. A., ABUAF, N., JONES, O. C., JR., AND SCHWARZ, C. E., "Heat Removal Characteristics of Volume-Heated Boiling Pools With Inclined Boundaries in Bubbly Flow Regime," ASME Paper No. 79-HT-99, 18th National Heat Transfer Conference, San Diego, CA (August 1979b).

JOHNSON, C. C. and GUY, A. W., "Nonionizing Electromagnetic Wave Effects in Biological Materials and Systems," Proc. IEEE, Vol. 60, No. 6 (June 1972).

LORRAIN, P. and CORSON, D., Electromagnetic fields and Waves, 2nd Ed., W. H. Freemen and Company (1970).

SAFFMAN, P. G. and SIR G. I. TAYLOR, "The Penetration of a Fluid Into a Porous Medium or Hele-Shaw Cell Containing a More Viscous Liquid," Proc. Roy. Soc. (London) 245A, p. 312 (1958).

SCHEIDEGGER, A. E., The Physics of Flow Through porous Media, The Machmillan Company, New York (1957).

TAYLOR, SIR G. I., "The Instability of Liquid Surfaces When Accelerated in a Direction Perpendicular to Their Planes-I," Proc. Roy. Soc. (London) A, 201, p. 192 (1950).

VON HIPPEL, A. R., Dielectric and Waves, John Wiley and Sons, Inc., London (1954).

2. SSC Code Development (J. G. Guppy)

The Super System Code (SSC) Development program deals with the development of an advanced thermohydraulic code to simulate transients in LMFBRs and LWRs. During this reporting period, work on four codes in the SSC series was performed. These codes are: (1) SSC-L for simulating short-term transients in loop-type LMFBRs, (2) SSC-P which is analogous to SSC-L except that it is applicable to pool-type designs, (3) SSC-W for simulating short-term transients in LWRs, and (4) SSC-S for long-term (shutdown) transients occuring in either loop- or pool- type LMFBRs. Reference is made to the previous quarterly progress report (Agrawal, 1979) for a summary of accomplishments prior to the start of the current period.

2.1 SSC-L Code (J. G. Guppy)

2.1.1 Role of Buoyancy (I. K. Madni, E. G. Cazzoli)

In order to illustrate and quantify the role of buoyancy in governing the low-flow behavior of the primary system, the SSC-L code was applied to simulate flow coastdown to natural circulation in a loop-type design, using CRBRP thermohydraulic design data. Figure 2.1 shows the computed time history of core flow, pressure head and component pressure losses in the system, (Madni 1979a). At full power, full flow conditions, the net buoyancy head in the primary system is computed to be 2.06 kPa (≈0.3 psi). Compared to the pump driving head of 1136 kPa (≈165 psi), required to overcome the pressure losses in the system, this is indeed negligible. Thereafter, while buoyancy remains nearly constant, pump head and system losses decay rapidly. At 56.4 seconds, with core flow at slightly less than 5%, the pump head becomes negative and the pump begins to contribute to losses. Buoyancy is now the only driving force to maintain circulation. However, with losses in the circuit continuing to decay with flow, buoyance is able to overcome more and more of the impedances and flow decay becomes considerably damped. At 72 seconds, as core flow reaches its minimum value of 2.7%, the entire pressure losses in the circuit, including reactor vessel, have dwindled to a mere 2.15 kPa (≈0.31 psi). The buoyancy head is more than adequate to sustain these losses; consequently, there is a slight increase in flow as natural circulation is established.

These results point to the need to accurately specify the hydraulic profile so that, at any location, there is no mismatch in elevations when going completely around the circuit. A 10 cm mismatch for example, will create an artificial buoyancy head, either for or against the normal flow direction, of about 0.8 kPa, which will remain essentially unchanged during flow decay. Under natural circulation, this can equal about 37% of the total pressure losses in the system, and will drastically alter the core flow and temperature predictions. Likewise, the elevations of active core and IHX have to be properly specified to achieve the correct relative elevations of their respective thermal centers.

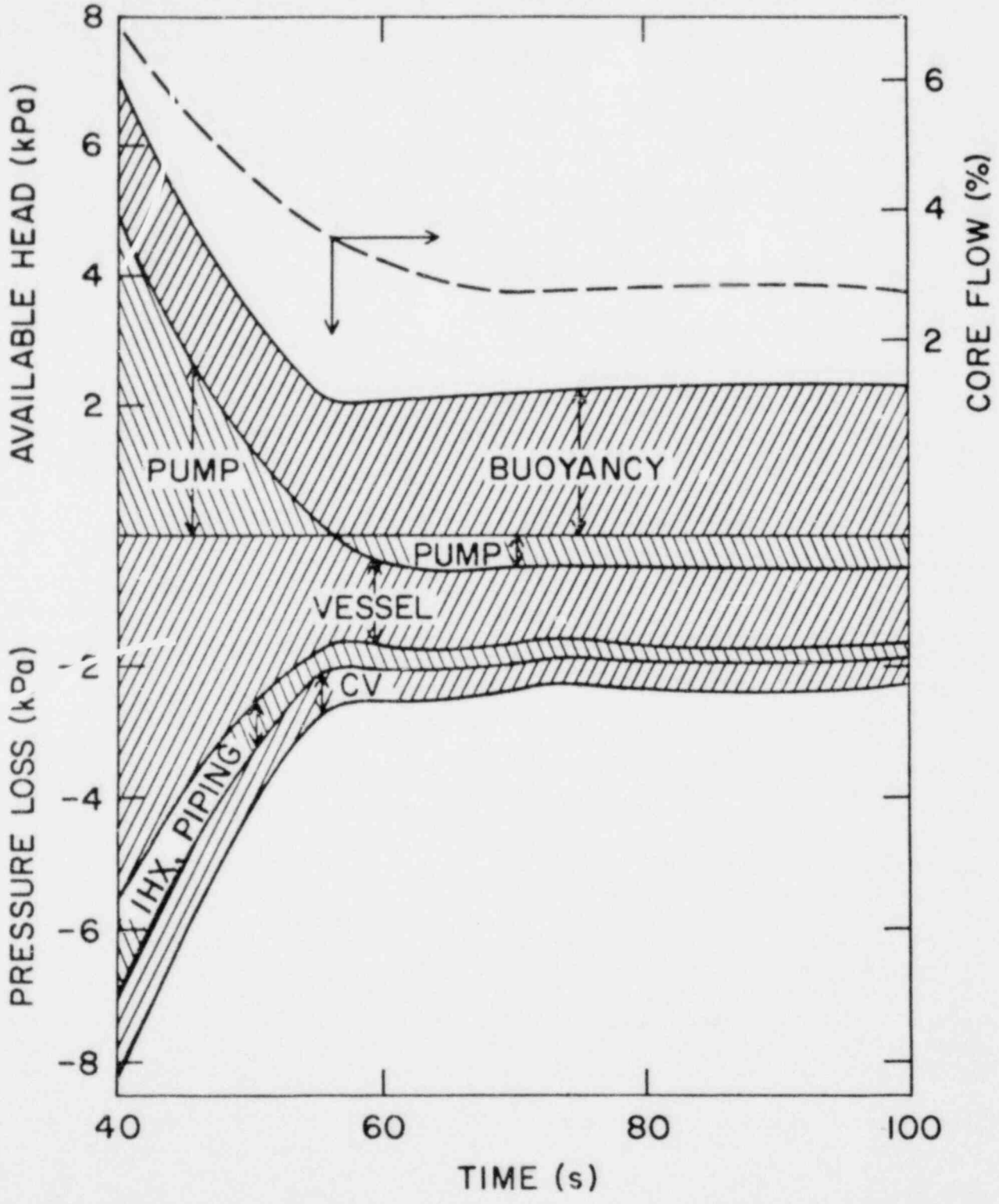

FIGURE 2.1

Core flow, pressure heads and component pressure losses in CRBR primary system during coastdown to natural circulation.

2.1.2 Effects of Modeling Friction (I. K. Madni, E. G. Cazzoli)

The SSC-L code was used to simulate flow coastdown to natural circulation in CRBRP. The detailed model in SSC-L was replaced by an approximate model to represent frictional losses in the pipings and IHX. Gravity heads and other details were kept the same in both models. In the approximate model, all frictional and form losses (excluding those in reactor vessel) were treated as $\Delta P = CW|W|$, where C is independent of the flow rate W. In the detailed model, the frictional resistances are explicitly included in the form

$$\Delta P_f = 0.5 \frac{W|W|}{D_e A^2} \int_o^L \frac{f}{\rho} dx, \qquad (2.1)$$

where f is the flow-dependent friction factor and form losses are treated as $KW|W|/\rho A^2$ where K is a constant. Comparisons between the predicted transient core flow using these models are shown in (Madni, 1979a). The effect was seen to be small, the results agreeing to within 2%. Note, however, that if friction in the reactor vessel was also included in $CW|W|$, the difference would indeed be very significant, since most of the frictional resistance of the circuit is in the core.

2.1.3 Effect of Check Valve Operation (I. K. Madni, E. G. Cazzoli)

A double-ended pipe rupture with break area equal to twice the cross-sectional area was postulated to occur just upstream of the cold leg check valve in CRBRP. Examination of predicted results for the first 18 seconds, (Madni, 1979a) showed that an operational check valve in the affected loop is very effective in reducing the initial transient severity. Compared to the results from a stuck open valve in the affected loop, the vessel inlet pressure is higher, core flow is higher, and the maximum sodium hot channel temperature is lower by about 100K. The margin to boiling is increased by more than 100K due to the higher saturation temperature with an operational valve.

2.1.4 Code Refinements (I. K. Madni, E. G. Cazzoli)

Oscillations in predicted vessel-to-pump flow coastdown had been a continuing problem with LOEP calculations using SSC-L. The problem was traced to the orifice tank pressure loss coefficient (K) being too small. Appropriately converting the value in DEMO to MKS units yielded a much higher K. Subsequent calculations with the new value for K in SSC-L showed the pump-to-vessel flow coastdown to be oscillation-free. Also, two problems in the steady state pump formulation that caused the predicted steady state transient results to drift from the initialized state were uncovered and subsequently corrected. First, since the impeller could be in either of two curves (HAN, HVN) during steady state operation, the code occasionally selected the wrong curve to calculate pump speed; this problem

has been resolved. Second, the polynomial representation for each curve has multiple roots. When steady-state operation was significantly different from 100%, the polynomial was found to converge to the root closest to the initial guess. This problem was eliminated by taking advantage of additional information about the curves to impose limits to the root appropriate to each curve, thus forcing the polynomial to converge only to the right root.

Corresponding refinements, wherever appropriate, have also been made to the SSC-P code.

2.1.5 Numerical Simulation of ATWS Events in LMFBRs (M. Khatib-Rahbar)

The SSC-L code was used to study a number of anticipated transients without scram (ATWS) events, (Khatib-Rahbar, 1979) using the Clinch River Breeder Reactor Plant (CRBRP) reference design (CRBRP, 1975) data where available.

Table 2.1 summarizes various feedback elements and their associated control settings for reactor power, primary and intermediate flow-speed control systems. Table 2.2 sets forth the primary control rod banking data.

Three representative anticipated transients without scram were simulated, namely: (1) a 10 cent step reactivity insertion, (2) a 25 cent step reactivity insertion and (3) a 10% ramp change in load demand in 40 seconds.

Figure 2.2 shows the reactor system response to a 10 cent and a 25 cent step reactivity insertion at time zero of the transient. The total reactivity is seen to jump from 0 to 0.10 and 0.25 dollar at time zero, causing a sharp rise in the neutron flux (power level) and, hence, an increase in reactor temperatures. The controller tries to correct for the disturbance by driving the regulatory bank into the core, until finally the neutron flux and the core mixed mean sodium temperature reach their respective setpoints as calculated by the plant supervisory controllers.

It is important to note that all of the automatic shutdown functions of the Plant Protection System (PPS), which would normally override the controllers in an event that the PPS settings are exceeded (e.g., 115% overpower signal) were not activated.

Figure 2.3 illustrates the plant response to a typical plant unloading of 10% in 40 seconds. It is seen that as the load demand is reduced, the plant control system responds by driving the regulating rod into the reactor as well as reducing the drive motor torque on both primary and intermediate pumps causing the desired reduction in the feedback variables to within the accuracies of their deadband settings.

From the results presented, the following conclusions emerge: (1) the representation of plant control systems in a large system simulation code is an essential tool for the study of ATWS event in LMFBR systems, and (2) the nonlinearity of the plant over a wide range of operating conditions necessitates a nonlinear simulation of the overall system.

For future work, the influence of unit controller settings and feedback cascading on the predicted response of the plant system requires further investigation. The interaction of the plant protection and control systems needs to be studied to determine the possibility of PCS adversely affecting or preventing the PPS actions.

TABLE 2.1
Plant Control System Data

Unit Controller		τ_m(s)	K	R(s^{-1})	τ_D(s)	ε_o	Actuator Constants
Reactor Power Controller	Steam Temperature	0.20	2.0	0	0	0	$V_{up} = 3.81 \times 10^{-3}$ m/s
	Core Mixed Mean Temp.	0.20	2.0	0	0	0	$V_{down} = -3.81 \times 10^{-3}$ m/s
	Neutron Flux	0.05	1.0	0	0	0.005	
Flow Controller — Primary	Reactor Inlet Temp.	0.20	1.0	0	0	0	$a_1 = 0.577$; $b_1 = 0.065$; $\zeta = 1.0$ (critically damped); $\omega_n = 0.375$ (s^{-1}); $\Omega_D = 1116$ rpm
	Sodium Flow	0.50	1.0	0	0	0	
	Pump Speed	0.02	1.0	0.10	0	0.005	
Flow Controller — Intermediate	Steam Pressure	0.15	1.0	0.02	0	0	$a_1 = 0.577$; $b_1 = 0.065$; $\zeta = 1.0$; $\omega_n = 0.375$; $\Omega_D = 1116$ rpm
	Sodium Flow	0.50	1.0	0.20	0	0	
	Pump Speed	0.02	1.0	0.10	0	0.005	

TABLE 2.2
Primary Control Rod Banking Data

Location	$\rho_{max,1}$(\$)	$Z_{max,1}$(m)	ρ_1(\$)	Z_1(m)
6-R7?	12.17	0.940	3.49	0.300
6-R7C	11.00	0.940	6.72	0.584
2-T1-	2.95	0.940	2.95	0.940

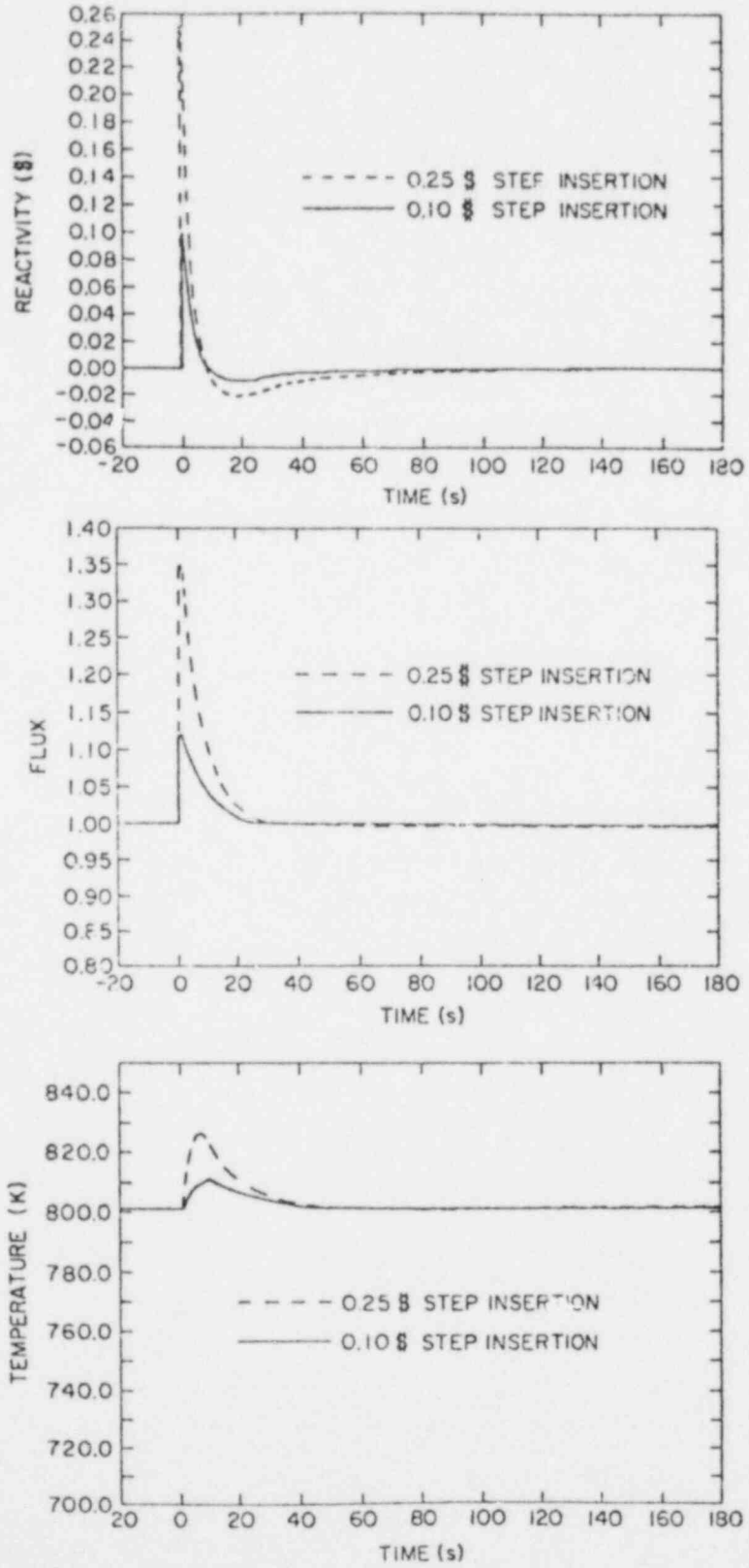

Figure 2.2 System Response to 10 cent and 25 cent Step Insertion of Reactivity Transient.

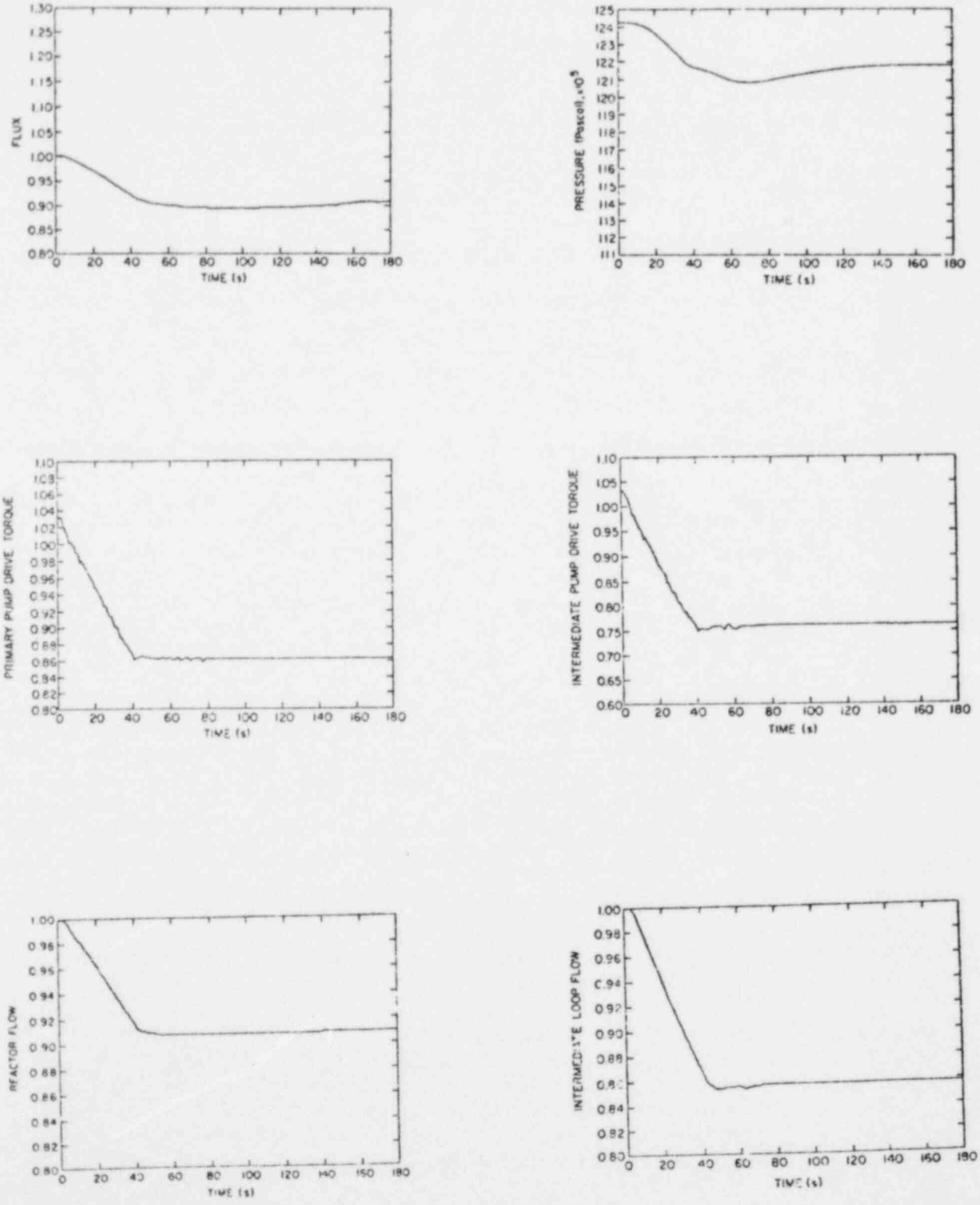

Figure 2.3 System Response to a Transient Resulting from a 10% Ramp Change in Power Demand in 40 Seconds.

2.1.6 Part Load Profiles (J. G. Guppy, E. S. Srinivasan)

A part load profile with SSC-L was successfully run using CRBRP prototype data from 100% load down to 40% load in decrements of 5% in power. The part load profile selected assumed a constant reactor power to primary flow rate ratio and constant steam generator outlet enthalpy conditions. The profile was accomplished by successive steady-state restarts using the latest cycle of SSC-L. In the course of accomplishing this part load profile several bugs were uncovered and subsequently corrected.

2.1.7 Core Flow Reversal (R. Pyare, J. G. Guppy, T. C. Nepsee and D. Thayer)

During the course of simulating pipe break transients with the latest cycle (CY-31) of SSC-L, a coding error was uncovered in the channel flow reversal calculations. An index counter for one of the recently modified structural temperature arrays was not properly set under reverse flow conditions. This problem was resolved.

In addition, an improved method for determining the boundary temperature in any given channel whenever a flow reversal occurs was accomplished. The axial temperature calculations are advanced by a marching technique which proceeds up or down the channel(s) in the direction of flow in that channel. Temporary axial temperature oscillations, observed immediately after flow reversal, have been substantially reduced by using channel dependent mixing lengths at the inlet module and outlet zone in calculating the boundary temperature.

2.1.8 Sodium Boiling (R. Pyare, T. C. Nepsee)

The boiling modules were made current with the latest cycle of SSC-L. The coding modifications to include effects of wire-wrap and hexcan structure were partially debugged.

2.1.9 Steam Generator Modeling (W. L. Weaver III, G. J. Van Tuyle, R. J. Kennett S. F. Carter)

Changes were made to the input processor for the steam generator module to give the user more flexibility in describing the steam generating system geometry. These changes have been made in anticipation of adding pressure relief and turbine bypass systems models to the code.

A steam turbine model consisting of a turbine control valve and turbine blade cascade has been developed and coded. This model will be used in conjunction with the turbine valve controller to determine the turbine inlet pressure boundary condition. Models of the turbine bypass system, pressure relief system and feedwater systems, with their individual controller, have been developed and are currently being coded and tested.

2.1.10 User Support (R. J. Kennett, J. G. Guppy)

The latest cycle of SSC-L, denoted SSC-L Export Version-002, was made available to all current users. These users include:

(1) BNL
(2) NRC/ARSR
(3) Gesellschaft fur Reaktorsicherheir (GRS), Cologne, West Germany
(4) Babcock & Wilcox
(5) Combustion Engineering
(6) General Electric
(7) University of Arizona
(8) Argonne National Laboratory

A staff member from GRS completed his stay at BNL. An input deck to SSC-L representing the entire SNR-300 reactor system was successfully produced and two test cases (LOEP and pipe break) were run successfully.

2.1.11 Accident Progression Analysis of Protected Transients in LMFBRs (M. Khatib-Rahbar, K. M. Jamali)

Accident progression analysis of protected transients in LMFBRs was started by reviewing the CRBRP Risk Assessment Report (CRBRP, 1977) and Sandia Laboratories Accident Delineation Study, (Sandia, 1978).

It is evident that the treatment of protected accident transients for LMFBRs is rather limited and incomplete. An attempt is being made to use SSC-L's unique capabilities to study accident sequences, characteristic of various protected transient events.

The present study uses fault tree analysis for the identification of dependent and common cause failures primarily in a qualitative manner. The COMCAN II computer code, (Rasmuson, 1978) will be used for common cause failure analysis of the fault tree. The minimal cut set and their associated rankings will be derived through the WAM-CUT computer code, (Erdman, 1978). Some dependent failure and event tree sequence probabilities will be determined using the WAM-BAM Code, (Leverenz, 1976). Phenomenological uncertainties will be clarified using various deterministic codes such as SSC-L.

2.2 SSC-P Code

2.2.1 Code Development (E. G. Cazzoli, I. K. Madni)

Following the code development approach adopted for SSC-P (Madni, 1979b) the current state of SSC-P is described by two program libraries. They are the current 'official' cycle of SSC-L and the most current cycle of SSC-P. The "pool" library contains subroutines which are totally new and unaffected by changes to SSC-L, as well as modified subroutines from the 'loop' library. The latter are definitely affected by any changes made to the corresponding routine in SSC-L. However, since these subroutines are part of the 'pool' library, they are not automatically updated. Keeping SSC-P current, there-

fore requires careful examination of all changes to SSC-L which are correspondingly updated in the pool routines. By using this process and updating the input data file, the SSC-P code was brought up-to-date with the current version of SSC-L, cycle 31 after considerable debugging. SSC-P now includes those refinements incorporated in SSC-L that were deemed necessary for SSC-P.

2.2.2 Tank Energy Balance (I. K. Madni, E. G. Cazzoli)

Barrier heat transfer coefficients (U1HM2, U1CM2) are calculated during steady-state by combining the composite barrier resistance with convective heat transfer coefficients between the metal and pool sodium. An option has been introduced to allow the user to input the values of U1HM2, U1CM2. A study was carried out which showed that these coefficients are not very sensitive to changes in temperature conditions. Hence an option has also been added to specify those coefficients which remain constant during the transient computations. For calculations done thus far, the code has been computing U1HM2, U1CM2 during initialization and using these same values during the transient.

2.2.3 Steady-state Transient (E. G. Cazzoli, I. K. Madni)

A steady-state transient from full power conditions in PHENIX was run using SSC-P, cycle 4 (consistent with SSC-L, cycle 31). The vessel inlet pressure was observed to decrease, causing the solution to drift towards a new steady-state. All calls to tank energy balance routines were then removed, and the problem was isolated and found to be caused by advancing the code to the new cycle.

The procedure described under 'Code Development' was followed and eventually, all cycle-related inconsistencies were isolated and removed. Following that, a steady-state transient was successfully executed, the solution remaining essentially drift-free.

The calls to tank energy balance modules were turned on again, and the code has been debugged up to the first integration step. Note that in SSC-P, tank energy balance equations are integrated together with pool hydraulics.

2.3 SSC-W Code (J. G. Guppy)

2.3.1 Steam Generator Modeling (G. J. Van Tuyle, W. L. Weaver, R. J. Kennett, S. F. Carter)

Work continued on modeling of the B&W once-through steam generator. Modifications included changing the primary side heat transfer correlation from the Graber-Reiger correlation (valid for sodium) to the Dittus-Boetler correlation (valid for water). The DNB correlation and the algorithm for the determination of the location of DNB were also modified. The DNB algorithm was modified so that a critical quality-boiling length correlation could be used, and the Biasi critical heat flux correlation was converted to this form and programmed into the code. A preliminary data deck for the steam generating system was prepared and a steady state in the steam generating system was successfully achieved. This preliminary data deck does not

model the internal downcomer and direct contract feedwater heating/aspirator system so that the steam generator behaves more like the newer B&W once-through steam generators which have integral economizers, rather than the once-through steam generators at TMI-2. Changes to the code which are required to model the direct contact feedwater heating/aspirator system and the internal downcomer are being coded.

2.3.2 Pressurizer Modeling (G. J. Van Tuyle, T. C. Nepsee)

The stand-alone pressurizer model (Agrawal, 1979) was verified against test data from the Shippingport plant, as reported by Redfield (1968). Discrepancies between present calculations and the reported results appear to be largely due to uncertainties in the spray and surge line temperatures. The pressurizer pressure was found to be quite sensitive to the spray temperature, in particular. The pressurizer model is now being incorporated into the SSC-W code.

2.3.3 Plant Data (R. Pyare, E. S. Srinivasan)

Based on the FSAR for the TMI-2 plant, a preliminary data deck was prepared. To collect certain data specific to the secondary loops, a meeting was arranged with GPU personnel at BNL. EPRI and B&W are also being consulted in this matter. The input deck for the GPU simulation of the TMI-2 plant using the RETRAN code is being reviewed.

2.3.4 Steady State Calculations (R. Pyare, T. C. Nepsee)

Using the preliminary data deck for TMI-2, a successful steady state run was accomplished using the SSC-W code. During this process, various coding problems were uncovered and resolved.

2.3.5 Transient Calculations (T. C. Nepsee)

Testing of the transient initialization segment of SSC-W is completed. The changes to modify the transient loop hydraulics calculations and to include the pressurizer have been interfaced.

2.4 SSC-S Code (J. G. Guppy)

2.4.1 Inter- and Intra- Assembly Temperature Flattening Effects (G. J. Van Tuyle)

A report was received from Prof. John E. Meyer (MIT), prescribing an algorithm to solve coupled equations representing intra-assembly heat transfer and buoyancy induced flow redistribution. Efforts were undertaken to fill in gaps in the algorithm and to implement this algorithm in computer code form. As of the end of this reporting period, neither the algorithm nor the brief code have been verified.

In another relevant area, the algorithm developed to speed up the matrix inversion in our Steady-state Porous-body Assembly Code (SPAC), derived from the ENERGY series of codes, was made available to Dr. Ehsan Khan of PNL. A factor of 40 in speed (2.5% of original computational cost) in our steady-state code (SPAC) had been gained over the ENERGY counter-part.

PUBLICATIONS:

The following is a list of publications during the current reporting period from this activity:

Gregory J. Van Tuyle (BNL) and John C. Lee (Univ. of Mich.), "Linearized Transient Analysis of Nuclear Steam Generators," ANS Transactions, 32, June, 1979.

M. Khatib-Rahbar, I. K. Madni, A. K. Agrawal and E. G. Cazzoli, "Transition to Natural Convection from Low-Temperature, Low-Flow Conditions in Loop-Type LMFBRs", Trans, Am. Nucl. Soc. 32, 503 (1979).

I. K. Madni, M. Khatib-Rahbar and A. K. Agrawal, "Effect of Pump-Stored Kinetic Energy on Natural-Circulation Decay-Heat Removal in Loop-Type LMFBRs", Trans. Am. Nucl. Soc. 32. 502 (1979).

M. Khatib-Rahbar, A. K. Agrawal and E. S. Srinivasan, "Feedback Control Systems for Non-Linear Simulation of Operational Transients in LMFBRs", Proc. of ANS/ENS International Meeting on Fast Reactor Safety Technology, Seattle, Washington (August 19-23, 1979).

A. K. Agrawal and M. Khatib-Rahbar, "Dynamic Simulation of LMFBR Systems", Journal of Atomic Energy Review, Vienna, Austria (Invited, In Press).

M. Khatib-Rahbar, I. K. Madni and A. K. Agrawal, "Impact of Multi-Dimensional Effects in LMFBR Piping Systems", Accepted for Presentation at Specialists' Meeting on Decay Heat Removal and Natural Convection In FBRs, Brookhaven National Laboratory, Upton, N.Y., (February 28-29, 1980).

M. Khatib-Rahbar, J. G. Guppy and A. K. Agrawal, "Natural Convection Transients in Homogeneous and Heterogeneous LMFBR Core Designs", Accepted for Presentation at Specialists' Meeting on Decay Heat Removal and Natural Convection In FBRs., Brookhaven National Laboratory, (February 28-29, 1980).

I. K. Madni, E. G. Cazzoli and A. K. Agrawal, "A Single-Phase Sodium Pump Model for LMFBR Thermal-Hydraulic Analysis", Proceedings of the 1979 International Meeting on Fast Reactor Safety Technology, Aug. 19-23, 1979, Seattle, Washington.

I. K. Madni and A. K. Agrawal, "LMFBR System Analysis: Impact of Heat Transport System on Core Thermal-Hydraulics", Specialists Issue of Nuclear Engineering & Design, Summer 1979 (Invited In Press).

I. K. Madni, "Transient Analysis of Coolant Flow & Heat Transfer in LMFBR Piping System", Brookhaven National Laboratory Topical Report (In Print).

A. K. Agrawal, J. G. Guppy, I. K. Madni and W. L. Weaver, "Dynamic Simulation of LMFBR Plant Under Natural Circulation", ASME Paper No. 79-HT-6, Presented at the 18th ASME National Heat Transfer Conference, Aug. 5-8, 1979, San Diego, California.

J. G. Guppy, "Application of Multiple Timestep Integration Method in SSC", Paper to be Presented at Winter Meeting (1979) of ANS in San Francisco.

REFERENCES

Clinch River Breeder Reactor Plant Preliminary Safety Analysis Report, Project Management Corporation (1975).

CRBRP Risk Assessment Report, (Draft) (1977).

ERDMAN, R. C. et al., (1978) "WAM-CUT, A Computer Code for Fault Tree Evaluation", EPRI-NP-803 (June 1978).

KHATIB-RAHBAR, M. et al., (1979), "Feedback Control Systems for Non-Linear Simulation of Operational Transients in LMFBRs," Proc. of International Meeting on Fast Reactor Safety Technology, Seattle, Washington (August 19-23, 1979).

LEVERENZ, [illegible] and KIRCH, H., (1976), "User's Guide for the WAM-BAM Computer Code", EPRI, 217-2-5 (Jan. 1976).

LMFBR Accident Delineation Study, (Draft), Sandia Laboratories (Oct. 1978).

MADNI, I. K. and AGRAWAL, A. K., (1979), "LMFBR Thermal-Hydraulic Analysis: Impact of Heat Transport System", Special Summer Issue of Nuclear Engineering & Design, 1979 (invited).

MADNI, I. K., CARTER, S. F. and CAZZOLI, E. G., (1979) "SSC-P Management and Interactions with SSC-L", Internal Memorandum to A. K. Agrawal, January 16, 1979.

KASMUSON, P. M. et al., (1978) "COMCAN II - A Computer Program for Common Cause Failure Analysis, EG & G Idaho, Inc. TREE-1289 (Sept. 1978).

REDFIELD, J. A. et al., (1968), "Pressurizer Performance During Loss-of-Load Tests at Shippingport: Analysis and Test", Nuclear Application, 4, pp 173-181, March, 1968.

3. SSC Validation (J. G. Guppy)

3.1 Simulation of FFTF Acceptance Tests (L. G. Epel, R. Pyare, W. L. Weaver)

During the past quarter the code validation effort continued to focus on the FFTF version of SSC-L. The new input deck, that represents the FFTF case with 19 channels and which incorporated data consistent with the requirements of "cycle 31", was used to simulate four of the FFTF acceptance tests (series 5A008). The initial conditions of these tests are summarized in Table 4.1. Following achievement of steady state at the conditions below, a loss of electric power (LOEP) incident is simulated by tripping all of the primary and secondary loop pumps, all of the fans in the Dump Heat Exchanger (DHX), and scramming the reactor.

Table 4.1
Summary of Acceptance Test Series 5A008 Initial Conditions

	Test D	Test C	Test B	Test A
Power, MWt (%)	400 (100)	300 (75)	140 (35)	20 (5)
Primary Loop Flow, GPM (%)	13373 (100)	10030 (75)	10030 (75)	10030 (75)
Secondary Loop Flow, GPM (%)	13113 (100)	9835 (75)	9835 (75)	9835 (7[illegible]
Primary Cold Leg Temp, F	680	659	625	590
Primary Hot Leg Temp, F	938	917	745	607
Secondary Cold Leg Temp, F	595	595	595	585

The 19 channels were chosen so that the hot channel, the average channel, the 2 fueled open test assemblies (FOTA), and many other groups of assemblies could be studied in detail and individually. The 19 channels were grouped according to flow-to-power ratio in each of the three orifice zones as shown in Table 4.2. Note that channel 19 represents 92 non-fueled assemblies made up of control, shim, reflectors, and shield assemblies. In Table 4.2 the row 2 FOTA is represented by channel 3; the row 6 FOTA by channel 18.

The input decks that are being used to describe the four LOEP transients summarized in Table 4.1 have been "fine-tuned" during the quarter to be as consistent with design information as possible. In connection with this goal, a meeting was held with HEDL personnel to exchange information and to compare preliminary results of several SSC runs with IANUS predictions.

Table 4.2
Power and Flow Fractions of 19 Channels

Channel Number	Number of Assemblies	Power Fraction	Flow Fraction	Power/Flow
1	1	.01772	.01219	1.453
2	4	.06772	.04878	1.388
3	1	.01723	.01219	1.413
4	9	.14230	.10975	1.297
5	9	.12196	.10975	1.111
6	3	.03513	.03658	.960
7	1	.01629	.01161	1.404
8	3	.04577	.03482	1.314
9	6	.08698	.06964	1.249
10	5	.06849	.05804	1.180
11	3	.03226	.03482	.927
12	1	.01340	.00989	1.355
13	6	.07046	.05933	1.188
14	9	.09773	.08900	1.098
15	4	.04070	.03955	1.029
16	5	.04692	.04944	.949
17	2	.01687	.01978	.853
18	1	.01367	.00989	1.383
19	92	.04838	.10049	.481
	165	1.00000	.91555	

The test runs performed to date have uncovered some "bugs" in the coding, which have subsequently been corrected and have suggested some improvements/ extensions which have subsequently been implemented.

In order to accommodate the size of the 19 channel problem a new allocation of computer memory was instituted. The program was updated as discussed previously in Sections 2.1.2 and 2.1.4.

Finally, some inconsistencies in the operating characteristics of the fans in the DHX have been resolved and appropriate programming changes were made to correct the discrepancies.

PUBLICATIONS:

The following is a list of publications during the current reporting period from this activity:

W. L. Weaver III, L. G. Epel, A. K. Agrawal, "Pre-Test Simulation of FFTF Natural Circulation Acceptance Tests", BNL-NUREG-26327, Paper to be presented at Winter Meeting (1979) of ANS in San Francisco.

☆ U.S. GOVERNMENT PRINTING OFFICE 1980—37